Développement d'un nouveau spectromètre RPE à haute fréquence

Utsab Banerjee

P[[[[[[[[[[[[[

Sorbonne Université

École doctorale388 Chimie Physique et Chimie Analytique de Paris

CentreLaboratoiredes Biomolécules / Équipe 3 : Structure et

Dynamique des Biomolécules

Development of Novel High-Frequency EPR Spectrometer and In-house fabrication of NMR MAS drive caps and ultra-centrifuge kit packing tools

Par Utsab Banerjee

Thèse de doctorat de Sciences de la Sorbonne Université

Dirigée par Daniel Abergel et Kong Ooi Tan

Présentée et soutenue publiquement le 07 décembre 2023

Composition du jury :

1. Rachel Martin, Rapporteur, Membre of the jury, University of California, Irvine, USA.
2. Sun Un, Rapporteur, Membre of the jury, CEA Saclay, France.
3. Thomas Prisner, President of the jury, J.W. Goethe-Universität Frankfurt, Germany.
4. Daniel ABERGEL, Directeur de thèse, Membre of the jury, LBM, École Normale Supérieure Paris, France.
5. Kong Ooi Tan, Co-supervisor, Member of the jury, LBM, École Normale SupérieureParis, France.

.

Contents

Abstract

Nuclear magnetic resonance (NMR) spectroscopy is a powerful method that can give insights into chemical processes and has the capability to characterize a wide variety of molecules. The simplicity of the preparation, the absence of damage to the analyte, and the moderate sample volumes needed are among the important reasons that make NMR a widely used spectroscopy method.

Nuclear magnetic resonance (NMR) is a powerful analytical technique that can provide structural information on analytes. However, it also has some drawbacks, such as low sensitivity. There are several methods to improve the sensitivity of NMR. One of the most powerful ways to improve NMR sensitivity is through dynamic nuclear polarization (DNP). However, due to the lack of knowledge of the electron and nuclear spin systems, DNP has not yet reached its full potential, which is further aggravated by the decreasing efficiency of DNP in high fields over 14 Tesla. To assess the spectral and spin dynamics of both nuclei and electrons in a sample system under DNP conditions, this type of study may be significantly enhanced using diagnostic tools. For this reason, we need to be able to use both NMR and EPR to accurately measure the DNP parameters and describe the spin-dynamic properties of samples that have the same concentration and solvent and are exposed to the same microwave power, cryogenic temperature, and magnetic field.

In order to easily and cost-effectively build an EPR/NMR probe, the longitudinal detected EPR technique is used here. Longitudinal detection (LOD) of EPR is based on a pickup coil aligned parallel to the static magnetic field to measure a changing longitudinal magnetization. The detection coil is placed orthogonally to the transmit coil and tuned to a different frequency range, which reduces the transmit crosstalk and noise. Amplitude modulation of the microwave can periodically saturate the electron magnetization by modulating the longitudinal magnetization. The resulting longitudinal magnetization changes over time, which causes an alternating voltage in the EPR coil with an axis that is parallel to static magnetic field. In this thesis, we have also shown that an LOD EPR optical chopper can be used to modulate the microwave for high-frequency, high-power devices. This is important because it will enable us to use the optical chopper with high-power microwave sources like the gyrotron, where microwave amplitude modulation is not possible. We have also shown that an optical chopper can be used with a gyrotron to perform DNP without causing any damage to the microwave source.

The other topic mentioned here is 3D-printed caps for solid-state NMR and ultracentrifuge kits to pack samples in solid-state NMR rotors. 3D-printing technology has emerged as a well-developed method to produce parts with considerably low cost and yet high precision (<100 µm). Recent literature has shown that 3D-printing technology can be exploited to fabricate a magic-angle

spinning (MAS) system in solid-state nuclear magnetic resonance (NMR) spectroscopy. It was demonstrated that advanced industry-grade 3D printers could fabricate 3.2 mm MAS drive caps with intricate features, and the caps were shown to spin > 20 kHz. Here, we show that not only lab-affordable benchtop 3D printers can produce 3.2 mm drive caps with a similar quality as the commercialized version, but also smaller 2.5 mm and 1.3 mm MAS drive caps—despite a slight compromise in performance. All in-house fabricated drive caps (1.3 to 7 mm) can be consistently reproduced (>90%) and achieve excellent spinning performances. In summary, the > 3.2 mm systems have similar performances as the commercial systems, while the 2.5- and 1.3-mm caps can spin up to 26 kHz ± 2 Hz and 46 kHz ± 1 Hz, respectively. The low-cost and fast in-house fabrication of MAS drive caps allows easy prototyping of new MAS drive cap models and, possibly, new NMR applications. For instance, we have fabricated a 4 mm drive cap with a center hole that could allow better light penetration or sample insertion during MAS. Besides, an added groove design on the drive cap allows an airtight seal suitable for probing air- or moisture-sensitive materials. Moreover, the 3D-printed cap was shown to be robust for low-temperature MAS experiments at 100 K, making it suitable for DNP experiments.

The development of magic angle spinning (MAS) rates higher than 100 kHz has made it easier to get high-resolution 1H-NMR spectra of biomolecules. However, challenges can arise when preparing rotors for these experiments due to the physical properties of biomolecular solid samples and the small dimensions of the rotors. In this study, we have designed 3D-printable centrifugal devices that facilitate efficient and consistent packing of crystalline protein slurries or viscous phospholipids into 1.3 mm and 0.7 mm rotors. We demonstrate the efficacy of these packing devices using ^{1}H-detected solid-state NMR at 105 kHz. In addition to devices for 1.3 mm and 0.7 mm rotors, we have also developed devices for other frequently employed rotor sizes and styles. We have made all our designs openly accessible, and we encourage their usage and ongoing development as a shared effort within the solid-state NMR community.

1. Résumé en français:

The entire summary is first written in English, and then DeepL software is used to translate the entire summary to French. To check the grammar, QuillBot software is used.

Part A: Développement d'un spectromètre RPE à haute fréquence

La spectroscopie par résonance magnétique nucléaire (RMN) est une méthode puissante qui permet de comprendre les processus chimiques et de caractériser une grande variété de molécules. La simplicité de la préparation, l'absence de dommages à l'analyte et les volumes d'échantillons modérés sont autant de raisons qui font de la RMN une méthode de spectroscopie largement utilisée.

La résonance magnétique nucléaire (RMN) est une technique analytique puissante qui peut fournir des informations structurelles sur les substances à analyser. Il existe plusieurs méthodes pour améliorer la sensibilité de la RMN. Cependant, en raison du manque de connaissances sur les systèmes de spin électronique et nucléaire, la DNP n'a pas encore atteint son plein potentiel, ce qui est encore aggravé par la diminution de l'efficacité de la DNP dans les champs élevés de plus de 14 Tesla. Pour évaluer la dynamique spectrale et de spin des noyaux et des électrons dans un système d'échantillons dans des conditions de DNP, ce type d'étude peut être considérablement amélioré à l'aide d'outils de diagnostic. Par conséquent, pour évaluer avec précision les paramètres de la DNP et caractériser les propriétés dynamiques du spin d'échantillons contenant la même concentration et le même solvant et soumis à la même puissance d'irradiation par micro-ondes, à la même température cryogénique et au même champ magnétique, une double capacité de détection de la RMN et de la RPE est nécessaire.

Afin de construire facilement et à moindre coût une sonde RPE/RMN, la technique de détection longitudinale de la RPE est utilisée ici. La détection longitudinale (LOD) de la RPE est basée sur une bobine de captation alignée parallèlement au champ magnétique statique, afin de mesurer une magnétisation longitudinale changeante. La bobine de détection est placée orthogonalement à la bobine d'émission et accordée sur une gamme de fréquences différente, ce qui réduit la diaphonie et le bruit de l'émission. L'aimantation longitudinale peut être modulée par une modulation d'amplitude des micro-ondes afin de saturer périodiquement l'aimantation électronique. L'aimantation longitudinale dépendante du temps qui en résulte induit alors une tension alternative dans la bobine EPR dont l'axe est parallèle à l'axe de la bobine. Dans cette thèse, nous avons également montré que l'EPR LOD peut être utilisé comme hacheur optique. Ceci est important car cela nous permettra d'utiliser le hacheur optique avec des sources de micro-ondes de haute puissance comme le gyrotron où la modulation d'amplitude des micro-ondes n'est pas possible. Nous avons également montré que le hacheur

optique peut être utilisé avec le gyrotron pour effectuer la DNP sans endommager la source de micro-ondes (gyrotron).

Dans la configuration LOD-EPR, les circuits d'excitation et de détection sont indépendants et bien isolés l'un de l'autre. Les fréquences d'excitation et de détection sont généralement éloignées de quelques ordres de grandeur l'une de l'autre. Cela permet de détecter des signaux à basse fréquence, tandis que des micro-ondes de forte puissance peuvent être utilisées pour l'irradiation de l'échantillon [9]. Cette robustesse permet une optimisation appropriée des différents éléments, comme le canal micro-ondes, qui peut être modifié pour une puissance élevée, tandis que le circuit de détection peut être modifié pour une large bande passante, une sensibilité élevée et les fluctuations de l'échantillon [11].

Dans le passé, il a été démontré que la LOD fonctionnait pour une large gamme de fréquences d'excitation. L'excitation a été réalisée sur une large gamme de fréquences, de l'échelle du MHz [12] à l'échelle du GHz. Alors que l'excitation se fait à haute fréquence, la détection se fait de HZ à des dizaines de kHz. Dans nos expériences, la plupart du temps, les expériences sont réalisées à une fréquence de détection inférieure à 10 Hz. Comme le circuit de détection fonctionne à une fréquence audio ou radio, il est plus facile à installer que les détecteurs RPE hétérodynes courants qui fonctionnent à la même fréquence micro-ondes que celle utilisée pour l'excitation.

Le circuit RPE LOD se compose de plusieurs sous-ensembles. Ces sous-unités sont les suivantes : (a) le circuit de détection [13] se compose d'un capillaire extérieur CFP (B) et d'un scellement dynamique (C), de sorte qu'il est possible de suivre une procédure de chargement de l'échantillon à l'intérieur du polariseur similaire à celle du bâtonnet d'échantillon dans une installation DNP à dissolution normale. La bobine de détection est un solénoïde divisé en fil de cuivre de 600 tours, composé d'un fil de cuivre émaillé de 0,1 mm enroulé autour d'un support de bobine en PEEK (E). Un petit espace permet aux micro-ondes d'atteindre l'échantillon. La partie inférieure de la forme de bobine a un diamètre extérieur de 7,5 mm, ce qui est suffisamment petit pour entrer dans la bobine RMN de l'insert DNP. Jusqu'à 120 µL d'échantillon peuvent être chargés dans la coupelle d'échantillon (F). Cette dernière glisse et se verrouille à l'intérieur de l'embase de la bobine. Le support de bobine est vissé en permanence à la partie supérieure de la fiole (D).

Les deux extrémités de la bobine de détection sont acheminées à l'intérieur du support de bobine et soudées à une paire torsadée de fils de cuivre argentés qui remonte à travers le capillaire noir pour transporter le signal hors du polariseur. Des connexions électriques sont prévues à l'extrémité extérieure de la sonde (A). La bobine (600 tours avec un fil de cuivre de 0,1 mm de diamètre) est alignée parallèlement au champ magnétique statique. La bobine est non résonnante et bien isolée de la terre pour réduire la diaphonie avec le signal de modulation de puissance.

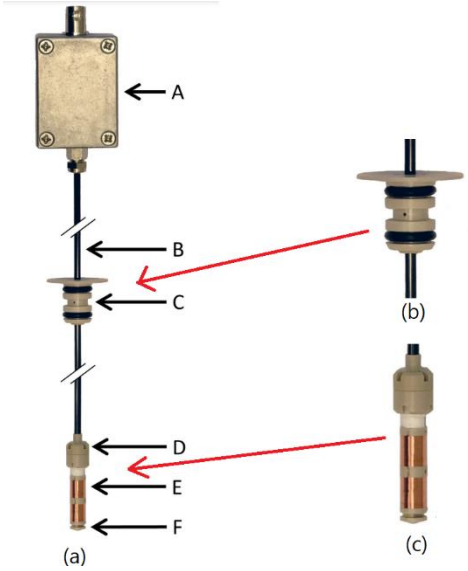

Fig. 1: (a) La sonde est composée des éléments suivants : une boîte de connexion étanche qui transforme la paire torsadée transportant le signal en connecteur BNC Twinax (A) ; un capillaire extérieur CFP 1/800 (B) avec son joint dynamique (C) et la partie supérieure de la fiole soudée au laser (D) ; un formeur de bobine supportant un solénoïde à broche de 600 tours (E) ; une coupelle d'échantillonnage (F). Les figures (b) et (c) illustrent la forme agrandie de l'étanchéité dynamique et de la bobine de captation. Sur la figure (b), l'espace pour les micro-ondes est clairement visible.

Deux types de configurations matérielles pour la mesure des signaux sont présentés ici. (1) Dans le premier cas, la bobine est connectée directement à un amplificateur différentiel audio, suivi d'un filtre passe-bas de 10 Hz. Le signal est mesuré à l'aide d'un dispositif d'acquisition de données NI (DAQ). La modulation d'amplitude (AM) est produite par le NI DAQ 6001 avant d'être envoyée à la source de micro-ondes. Pour saturer périodiquement les électrons, une onde carrée est générée par le DAQ pour la modulation d'amplitude et envoyée à la source de micro-ondes. Son amplitude contrôle le degré d'ouverture de l'atténuateur à la sortie du MW. À un maximum de 5 V, la puissance totale disponible est délivrée. La puissance totale des micro-ondes que le synthétiseur AnaPico peut produire est de 100 mW

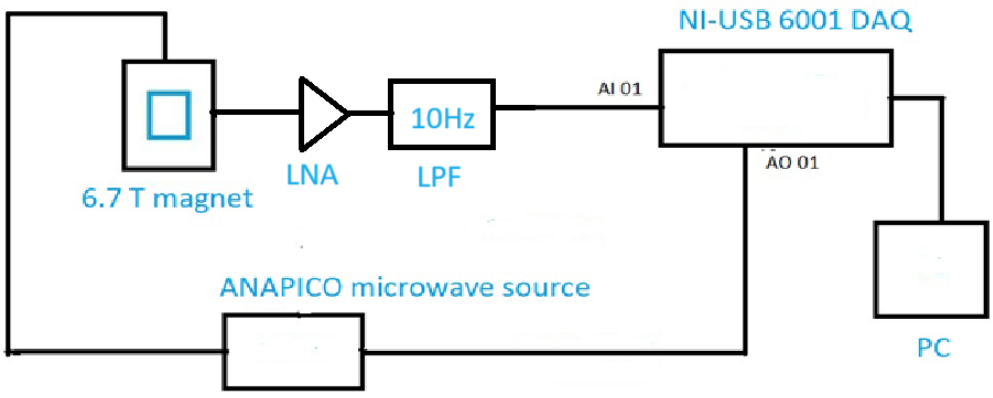

.

Fig. 2: La configuration de l'EPR LOD utilise un amplificateur audio à faible bruit avec un filtre passe-bas de 10 Hz, et l'acquisition est réalisée à l'aide d'un dispositif d'acquisition de données (DAQ) de National Instruments (NI).

Dans cette configuration, nous discuterons de la configuration double DNP/EPR. La bobine EPR LOD de la figure 3 (a) est insérée dans la sonde DNP de dissolution préexistante, comme le montrent les figures 3 (b) et (c). La sonde DNP de dissolution est équipée du guide d'ondes nécessaire pour se connecter à la source de micro-ondes. La sonde DNP de dissolution est équipée du guide d'ondes nécessaire pour se connecter à la source de micro-ondes et près de l'échantillon, il y a un réflecteur de micro-ondes pour irradier l'échantillon. La bobine RPE se trouve à l'intérieur de l'insert à radiofréquences et la bobine du renifleur fait face à la bobine correspondante de l'insert à radiofréquences. L'orientation correcte de l'insert RF est extrêmement importante pour les expériences de RMN. La boîte d'accord et d'adaptation est utilisée pour accorder et adapter le plus possible les fréquences nucléaires souhaitées, mais de petites variations se produisent en

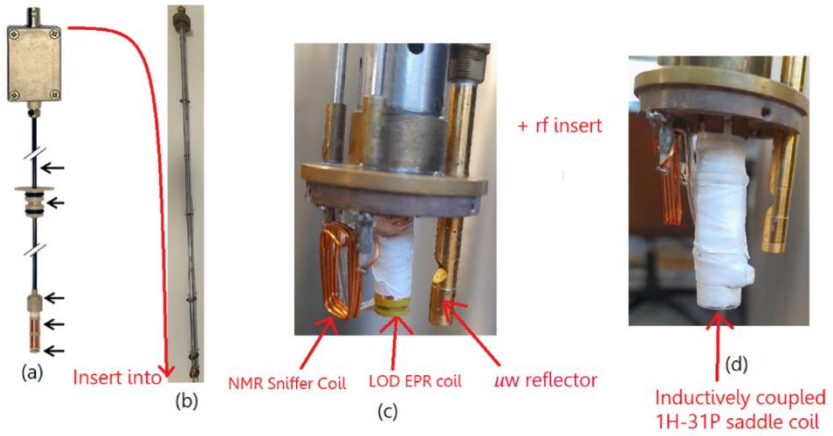

Fig. 3: The Probe is composed by the following components: (a) The LOD EPR detection coil, (b) The Dissolution DNP probe, (c) The enlarged picture of the bottom of the probe depicting the microwave reflector, NMR sniffer coil and the LOD coil and (d) the ^{1}H -^{31}P rf insert.

raison des changements de température.

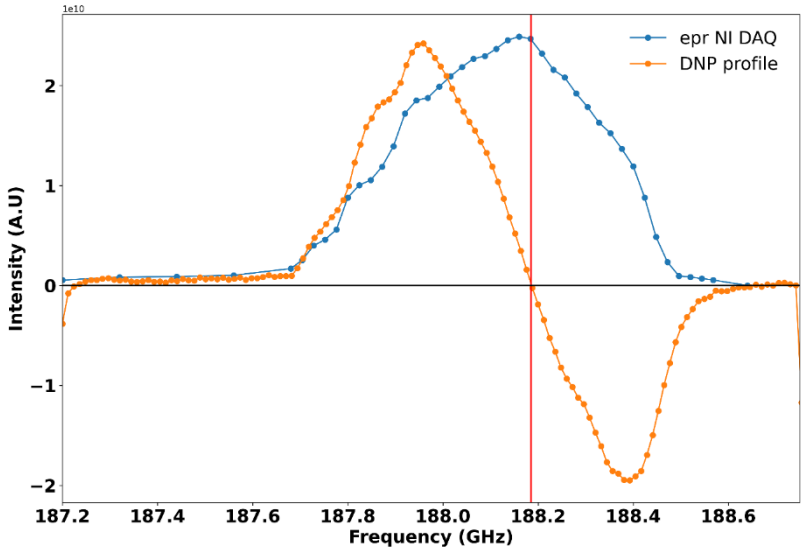

Fig. 4: Il montre le profil DNP (orange) et le profil EPR LOD (bleu) en utilisant NI DAQ.

Les expériences préliminaires ont été menées en utilisant le radical TEMPOL dans un jus DNP. La figure 4 montre le profil DNP et EPR de l'échantillon à 4,2K. AnaPico est utilisé comme source de micro-ondes avec une puissance maximale de 28mW dans la gamme des 188GHz. Pour l'expérience LOD EPR, la micro-onde est modulée par une onde carrée générée par la carte NI DAQ. L'acquisition est également réalisée à l'aide de NI DAQ où une technique de détection par verrouillage est effectuée. L'intensité de la RPE se situe à la position de passage à zéro du profil DNP. La fréquence de modulation d'amplitude des micro-ondes est de 5 Hz.

Jusqu'à présent, toutes les expériences RPE LOD ont été réalisées à l'aide de dispositifs à l'état solide. Pour réaliser la DNP à des champs plus élevés, il faut utiliser un gyrotron. Le gyrotron ne peut pas être déclenché à l'aide d'un signal de déclenchement. Et pour réaliser la RPE à un champ plus élevé, comme 18,8 T, il est très difficile de développer les composants micro-ondes nécessaires à ce champ. Pour mettre au point un système rentable permettant d'effectuer des mesures DNP et RPE à des champs plus élevés et des techniques RPE LOD plus puissantes, des modifications appropriées sont nécessaires. Dans la technique EPR LOD normale, les micro-ondes sont modulées à l'aide d'un signal de déclenchement provenant d'un générateur de fonctions ou d'une carte DAQ. Mais cela n'est pas possible avec le gyrotron. La solution que nous avons trouvée pour résoudre ce problème consiste à

utiliser un hacheur optique pour moduler les micro-ondes. Un schéma de

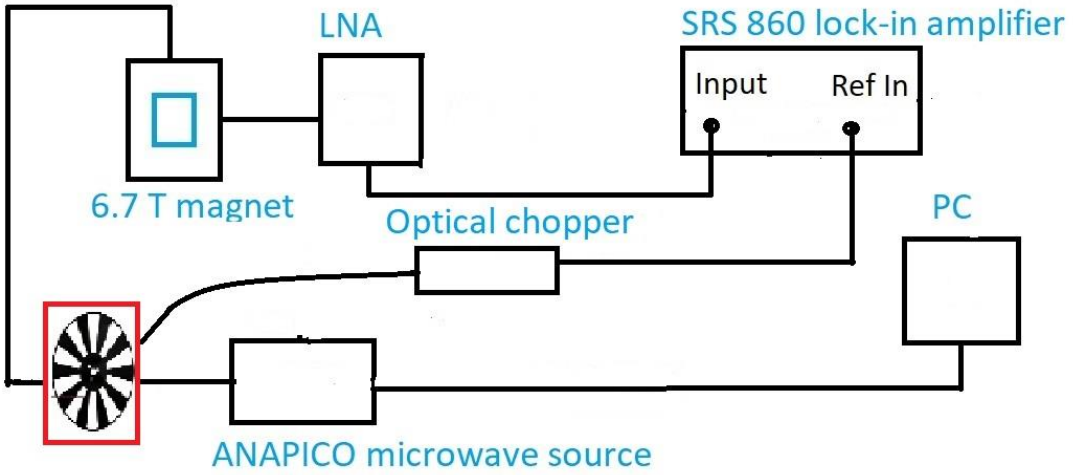

Fig. 5: Schéma de l'installation RPE à hachage optique pour le système 6,7 T/188 GHz.

l'installation est présenté à la Fig. 5.

Le diagramme de la figure 5 illustre l'installation du système à 188 GHz. Ce système a été développé en tant qu'expérience de démonstration de principe. La source de micro-ondes utilisée est la même que la source à semi-conducteurs AnaPico utilisée pour l'expérience RPE LOD normale.

Les expériences préliminaires ont été menées en utilisant le radical TEMPOL dans du jus de DNP. La figure 6 montre les profils DNP et RPE de l'échantillon à 4,2 k. AnaPico est utilisé comme source de micro-ondes, avec une puissance maximale de 28 mW dans la gamme des 188 GHz. Pour l'expérience EPR LOD, la micro-onde est modulée par un hacheur optique placé à 45° pour atténuer la réflexion de la micro-onde. L'intensité de la RPE est à la position de passage à zéro du profil DNP. La fréquence de modulation d'amplitude des micro-ondes est de 5 Hz.

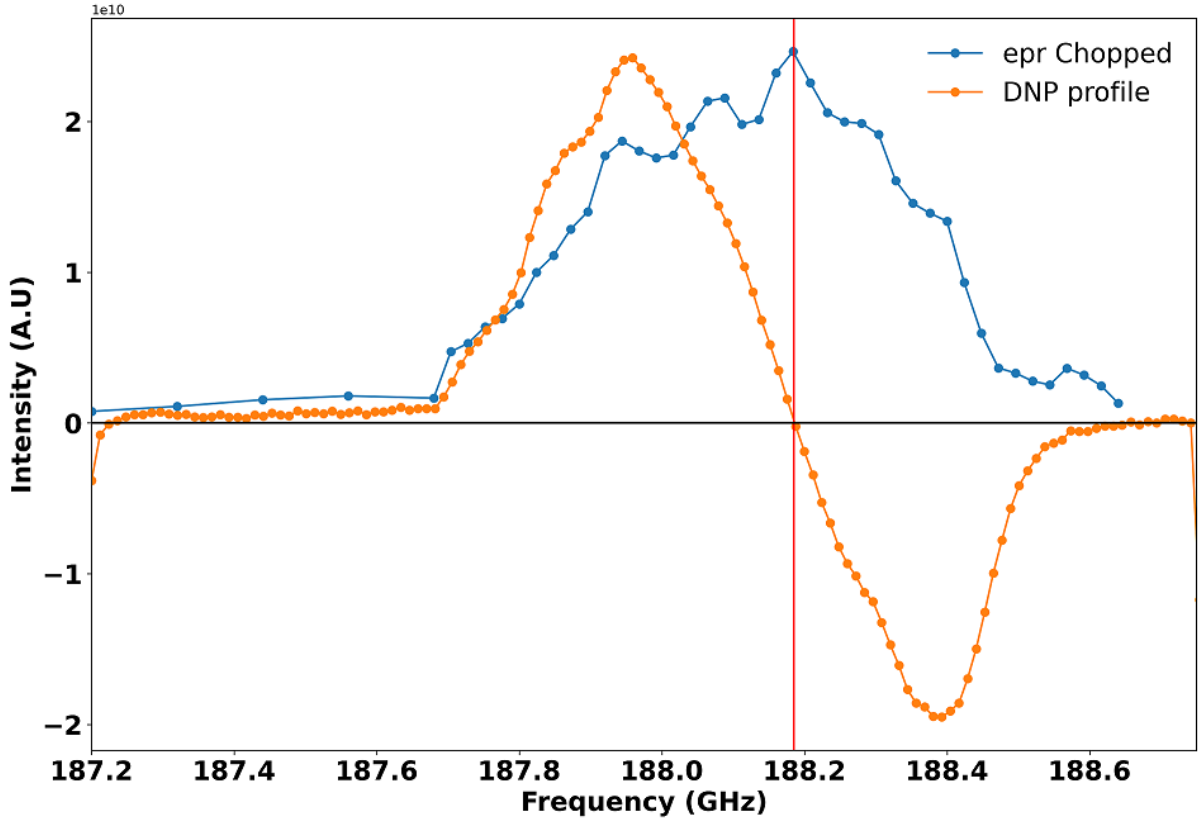

Fig. 6: Il montre le profil DNP (orange) et le profil RPE LOD (bleu) en utilisant un hacheur optique.

Part B: Fabrication en interne de capuchons de rotor RMN à l'état solide

La RMN du solide est une technique de caractérisation puissante qui a été largement appliquée à l'étude d'échantillons solides allant des petites molécules aux macromolécules biologiques, en passant par les matériaux inorganiques [1]. Bien que les échantillons à l'état solide présentent généralement des pics larges dus à des interactions anisotropes telles que les couplages dipolaires et l'anisotropie du déplacement chimique, il est possible de les atténuer en réalisant des expériences de rotation à l'angle magique (MAS) [2,3], où l'échantillon est tourné à un angle de 54,74 par rapport au champ magnétique statique. Il est essentiel que la fréquence MAS () soit suffisamment supérieure à la taille des interactions anisotropes pour obtenir un effet efficace de rétrécissement des raies, c'est-à-dire que les rotors peuvent tourner jusqu'à = 160 kHz en fonction de leur taille [4,5].

Il existe deux grandes catégories de technologies d'impression 3D : la modélisation par dépôt en fusion (FDM) et la stéréolithographie (SLA). Bien que la méthode FDM ait, en général, une moins bonne résolution, elle est plus abordable et plus facile à utiliser que la méthode SLA à base de résine. Les deux technologies d'impression 3D ont été exploitées dans diverses applications RMN, allant de la fabrication de systèmes d'éjection d'échantillons MAS [11], de bobines RF [12-15], de tubes d'échantillons RMN [16], de générateurs de parahydrogène [17], d'appareils de dégazage

d'échantillons RMN [18,19], de têtes de sondes RMN [20], etc. Outre ces exemples, Xu et al. ont récemment démontré qu'il était possible de fabriquer des capuchons de stator et d'entraînement MAS à l'aide de FDM, mais uniquement pour un système > 3,5 mm [9]. La technologie SLA à haute résolution a également été exploitée pour construire le système de filature MAS. Parmi les exemples notables, on peut citer la fabrication de stators de rotors sphériques de > 4 mm à l'aide d'une imprimante 3D de table par le groupe de Barnes [21,22], ainsi qu'un stator de rotor cylindrique de 3,2 mm et des capuchons d'entraînement produits par des entreprises de fabrication spécialisées, comme l'ont rapporté Banks et al [10]. Bien que l'externalisation du processus de fabrication permette d'économiser des ressources en main-d'œuvre, nous constatons que la qualité des pièces varie d'un lot à l'autre. Cela pourrait s'expliquer par le fait que les étapes d'impression et/ou de post-traitement réalisées par l'entreprise ne sont pas nécessairement les mêmes pour chaque lot. Par conséquent, l'absence de résultats cohérents pourrait conduire à un processus plus long et plus coûteux. En outre, la même publication indique que l'imprimante 3D de table (Form 3 avec une résolution XY de 25 µm) a été testée comme étant incapable de produire des capuchons d'entraînement de 3,2 mm [10]. Dans cette publication, nous réexaminons cette affirmation en montrant que non seulement l'imprimante 3D Form 3+ peut fabriquer des capuchons d'entraînement robustes de 3,2 mm, mais aussi des capuchons d'entraînement plus petits de 2,5 et 1,3 mm (avec des performances légèrement compromises). En particulier, les capuchons d'entraînement de 3,2 mm imprimés en 3D (Fig. 1) peuvent tourner jusqu'à = ¼ 22 kHz ± 1,3 Hz, ce qui a des performances similaires à celles des versions commerciales, mais ne coûte que < 1 US cents et 5 min/pièce à imprimer en 3D (en supposant une impression simultanée de 100 pièces en un seul travail d'impression). En outre, les capuchons d'entraînement imprimés en 3D et fabriqués en interne présentent une excellente stabilité de rotation, suffisante pour des expériences pratiques de RMN MAS multidimensionnelle.

Les capuchons d'entraînement ont été conçus dans Autodesk Inventor (Autodesk Inc, San Rafael) en suivant une conception similaire décrite dans Banks et al [10]. Les capuchons d'entraînement ont été imprimés à l'aide de la résine Clear v4 standard dans une imprimante Form 3+ (Formlabs) avec une résolution XY et une épaisseur de couche de 25 µm. L'imprimante 3D coûte environ 4000 USD et la résine environ 140 USD/litre. Les supports d'impression ont été placés sur le fond de la tige avec un point de contact de 0,3 mm. Il faut environ 4 heures pour imprimer simultanément en 3D 100 pièces de capuchons d'entraînement en un seul travail d'impression. Il est à noter que la plateforme de construction de l'imprimante 3D peut accueillir plus de 100 pièces en une seule impression (si nécessaire) sans augmenter de manière significative les heures d'impression. Une fois l'impression terminée, les pièces ont d'abord été rincées dans un mélange d'isopropanol et d'eau (rapport de 9:1 en volume) pour éliminer la résine non polymérisée et les irrégularités de la surface. Ensuite, les supports ont été retirés et rincés à nouveau avant d'être durcis sous lumière UV (Elegoo Mercury) pendant 1 heure (2x30 min, avec une autre étape de rinçage entre les deux sessions de durcissement) pour améliorer les propriétés mécaniques. Notez que les bouchons doivent être complètement secs après chaque étape de rinçage. Il

est connu que les pièces imprimées SLA rétrécissent progressivement au fil du temps, et le long temps de durcissement (1 heure) est une étape cruciale pour accélérer le processus de rétrécissement et, par conséquent, pour améliorer la stabilité à long terme. Pour tenir compte des changements de dimensions après les étapes de post-traitement, nous avons compensé ces changements de manière itérative en redessinant et en réimprimant les pièces. Outre l'imprimante 3D Form 3+, nous avons également testé une autre imprimante 3D de table (Elegoo Saturn), dont la résolution XY est inférieure (50 µm). Nous avons utilisé l'imprimante 3D Elegoo pour imprimer des bouchons de 4 mm (avec la résine grise standard Elegoo), et ils montrent des performances similaires à celles de la version commerciale (Bruker).

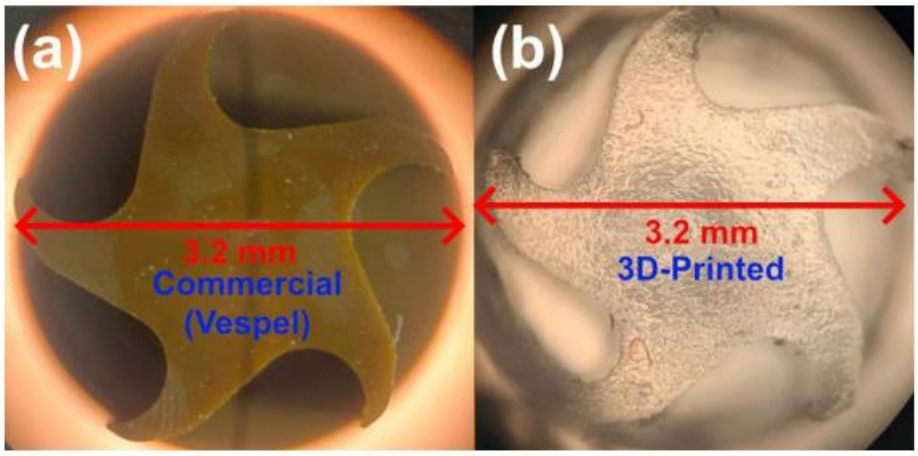

Fig 7: Image (a) d'un Vespel commercial (Bruker) et (b) d'un capuchon d'entraînement MAS de 3,2 mm imprimé en 3D.

Les capuchons imprimés en 3D ont été montés dans des rotors standard en ZrO_2 pour des expériences MAS dans des sondes MAS Bruker ou dans une station de filage de paillasse à température ambiante. Une unité Bruker MAS II a été utilisée pour réguler l'entraînement et la pression du gaz de roulement afin d'obtenir une fréquence de rotation stable. Nous avons testé au moins 10 pièces de chaque modèle pendant au moins 15 minutes pour évaluer les performances MAS. La pression de chaque entrée de gaz et la fréquence de rotation en fonction du temps en mode automatisé ont été enregistrées à l'aide de TopSpin (Bruker). Nous avons testé les capuchons d'entraînement de 3,2 mm sur des rotors en ZrO_2 et en saphir. Tous les rotors en zircone équipés de capuchons imprimés en 3D ont tourné à plus de 20 kHz sans problème majeur. Cependant, le rotor en saphir s'est cassé lorsqu'il a tourné à plus de 18 kHz (15 kHz à la température de référence). Pour les capuchons d'entraînement de 1,3 mm imprimés avec une imprimante 3D industrielle (Boston Micro Fabrication (BMF)), nous n'avons testé que 2 des 3 pièces commandées.

L'échantillon de L-Isoleucine ^{13}C-^{15}N a été acheté à CortecNet et utilisé sans purification supplémentaire. Pour l'échantillon de cadre organo-métallique (MOF-801) [23], le MOF a été synthétisé selon une procédure établie et lavé avec du D_2O à l'aide d'ultrasons [23]. L'étape de lavage au D_2O a été réalisée pour favoriser l'échange du proton hydroxyle (Zr-OH) avec le deutérium, ce qui permet d'attribuer sans ambiguïté le pic RMN du Zr-O ^1H observé dans un

échantillon de MOF lavé au H_2O. L'échantillon de MOF lavé au D_2O a ensuite été activé dans un four de séchage sous vide pendant 12 h à 100 °C pour éliminer l'excès de solvant. Pour minimiser l'exposition de l'échantillon de MOF séché à l'humidité de l'atmosphère, l'échantillon a été emballé dans un rotor de 3,2 mm fermé par un capuchon d'entraînement imprimé en 3D et scellé par une rainure remplie de silicone (Bluestar CAF 1) à l'intérieur d'une boîte à gants remplie d'argon. Les spectres RMN ont été acquis à l'aide d'un spectromètre 800 MHz équipé d'une console Avance Neo (Bruker). Nous avons utilisé une sonde MAS à trois canaux de 1,3 mm, 2,5 mm ou 3,2 mm (sans E) pour réaliser les expériences de RMN MAS. Les déplacements chimiques ^{1}H et ^{13}C ont été référencés par rapport au signal de l'adamantane à 38,5 ppm sur l'échelle du tétraméthylsilane (TMS). L'expérience RFDR (Fig. 8a) a été réalisée avec la sonde de 1,3 mm à une fréquence MAS de 45 kHz avec un temps de mélange RFDR d'environ 2 ms. L'expérience DARR (figure 8b) a été réalisée avec la sonde de 2,5 mm à = 20 kHz avec un temps de mélange DARR de 100 ms. Les spectres HETCOR (Fig. 8c&d) ont été acquis à l'aide d'une sonde de 3,2 mm à = 10 kHz. La durée de chaque expérience 2D est d'environ 2 heures. L'angle magique et l'homogénéité du champ ont été optimisés avec du KBr et de l'adamantane, respectivement.

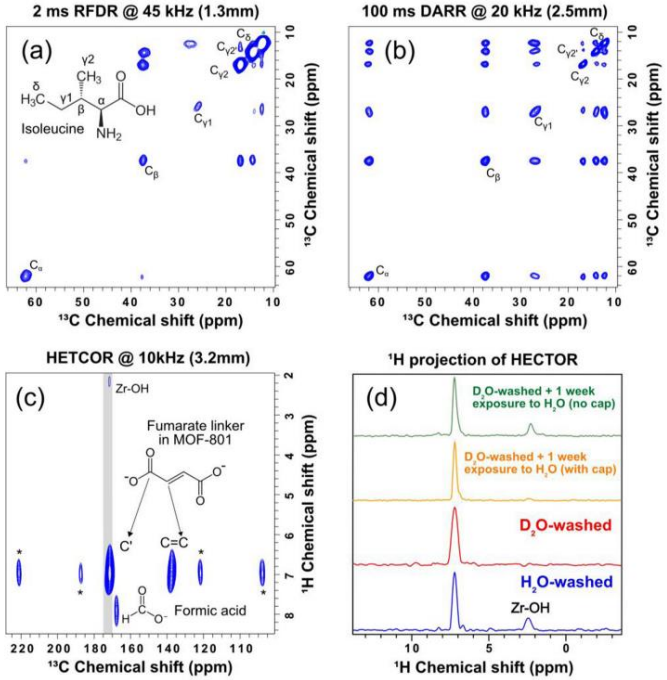

Fig. 8: Spectres RMN 2D acquis avec (a) des capsules imprimées en 3D de 1,3 mm, (b) de 2,5 mm ou (c) de 3,2 mm. (a) Spectre ^{13}C-^{13}C RFDR de L-Isoleucine dans un rotor de 1,3 mm à = 45 kHz. (b) Spectre ^{13}C-^{13}C DARR de L-Isoleucine dans un rotor de 2,5 mm à = 20 kHz. (c) Spectre ^{1}H-^{13}C HETCOR du MOF-801 dans un rotor de 3,2 mm à = 10 kHz. * indique les bandes latérales en rotation. Notez qu'il existe deux isomères de l'isoleucine qui donnent lieu à deux pics Cc2, le second pic étant étiqueté Cc20 [39]. (d) Projection 1D montrant la dimension ^{1}H (intégrer le long de la zone grise en (c)) pour le MOF-801 lavé dans H_2O (bleu), D_2O (rouge), MOF lavé dans D_2O exposé à la vapeur d'eau saturée pendant une semaine avec (jaune) ou sans (vert) le capuchon imprimé en 3D scellé avec de la silicone.

Part C: Kit de centrifugation imprimé en 3D pour l'emballage d'échantillons dans des rotors à l'état solide

La spectroscopie RMN à l'état solide est une technique puissante utilisée pour la caractérisation de divers matériaux, notamment la matière organique naturelle (MON), les solides moléculaires organiques, les composés inorganiques, les cocristaux pharmaceutiques, les polymères et les protéines. Elle fournit des informations structurelles et dynamiques précieuses sur ces matériaux (Mao et al., 2017 ; Dudenko et al., 2013 ; Cuny et al., 2008 ; Li et al., 2018 ; Seyger et al., 1999 ; Harris, 2016 ; Pacilio et al., 2014 ; Jensen et al., 2011). Le manque de résolution spectrale dans l'étude des solides biomoléculaires par RMN a conduit à l'utilisation de la rotation à angle magique de l'échantillon. Dans le MAS, l'échantillon est tourné à un angle de θ=54,74° par rapport au champ magnétique statique, moyennant les interactions de spin nucléaire qui ont une dépendance orientationnelle décrite par 3cos2 θ - 1, ce qui donne des spectres RMN avec des déplacements chimiques isotropes bien résolus [9-10]. Il est important que la fréquence MAS soit supérieure à la taille des interactions anisotropes pour obtenir un effet efficace de rétrécissement de la ligne. Dans la plupart des systèmes, la fréquence MAS jusqu'à 40kHz est suffisante pour annuler le couplage dipolaire hétéronucléaire et les interactions d'anisotropie de déplacement chimique (CSA). Mais pour les systèmes comportant des termes d'ordre supérieur dans l'expansion de l'hamiltonien, la vitesse MAS de 40 kHz ne fait que faiblement la moyenne des termes, ce qui se traduit par un élargissement homogène. Pour résoudre ce problème, une vitesse de rotation plus élevée est nécessaire. Pour obtenir des fréquences MAS aussi rapides sans chauffer de manière significative l'échantillon RMN, les rotors sont tournés pneumatiquement avec du gaz pour réduire l'échauffement par friction. Le moyen le plus efficace d'augmenter la fréquence MAS d'un rotor à entraînement pneumatique est de réduire le diamètre de la paroi extérieure du rotor. C'est ainsi qu'est née la fabrication de rotors de plus petit diamètre, comme les rotors de 1,3 mm et de 0,7 mm. Le rotor de 0,7 mm peut tourner jusqu'à 110 kHz.

Il est de plus en plus difficile de transférer et de conditionner efficacement les échantillons dans les rotors à mesure que les taux de MAS augmentent et que les diamètres des rotors diminuent. Cette difficulté est amplifiée lorsque les rotors doivent être remplis de solides biomoléculaires d'un diamètre inférieur à 1 mm et qu'ils doivent être maintenus humides pour les études qui reproduisent les conditions naturelles. Beaucoup de ces solides biomoléculaires sont des boues ou des gels mous et visqueux, ce qui les rend difficiles à manipuler. À l'aide d'une micro-spatule ou d'autres outils, il est possible de transférer manuellement ces échantillons dans des rotors plus grands, mais cette méthode entraîne souvent une perte ou une déshydratation de l'échantillon et est particulièrement difficile pour les très petits rotors. En outre, des protocoles efficaces et fiables de remplissage des rotors sont nécessaires si nous voulons profiter d'un autre avantage des petits rotors, à savoir la capacité de mesurer des échantillons pour lesquels seule une très petite quantité de matériau est disponible.

Le problème du remplissage de ces rotors de petit diamètre avec des gels ou des protéines hydratés a été résolu en utilisant le dispositif de remplissage du rotor centrifuge, où l'échantillon est canalisé dans le rotor grâce à la force centrifuge.

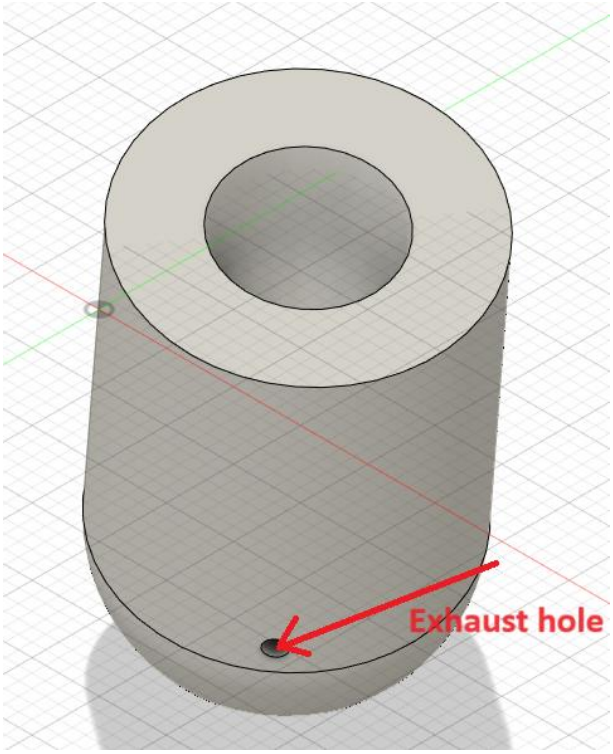

Fig. 9: Vue en coupe complète du kit d'ultracentrifugation de 0,7 mm avec le trou d'échappement indiqué sur la figure.

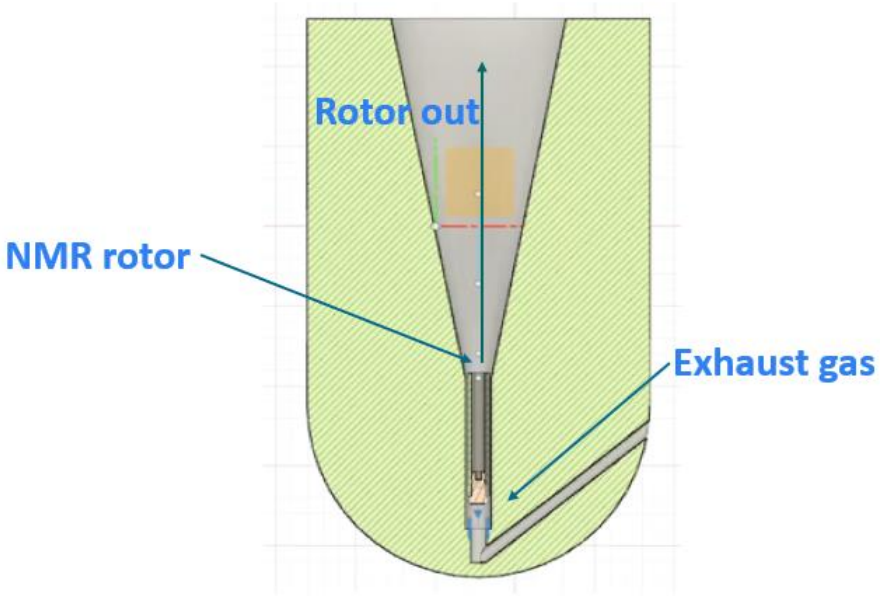

Fig. 10: Demi-coupe du kit d'ultracentrifugation de 0,7 mm avec l'orifice d'échappement et l'encoche du rotor illustrés dans la figure.

Les kits de centrifugation ont été conçus à l'aide d'Autodesk Fusion 360 (Autodesk Inc, San Rafael). Les kits ont été imprimés à l'aide de la résine standard clear v4 dans notre imprimante interne Form3+ (Formlabs) avec une résolution XY de 25 µm et une épaisseur de couche comme le montrent les figures 9 et 10. Le principe de fonctionnement du kit d'ultracentrifugation imprimé en 3D est le suivant : le rotor est d'abord placé dans la chambre du rotor du kit d'ultracentrifugation. Ensuite, la suspension aqueuse de l'échantillon est pipetée dans le kit et le kit est placé dans le tube de verre pour la centrifugeuse. Le tube de verre contenant le kit d'ultracentrifugation est placé dans le godet de la centrifugeuse pour l'ultracentrifugation. La centrifugation est effectuée pendant 1 à 2 heures avec une rotation à haute vitesse. Nous avons testé notre kit jusqu'à 400000Xg. L'échantillon sédimente pendant la centrifugation et est placé dans le rotor avec un peu de liquide. Le rotor est ensuite retiré du kit de centrifugation à l'aide de gaz. Nous pouvons pousser le rotor hors de la chambre en faisant circuler du gaz par l'orifice d'échappement.

References:

[1] Granwehr, Josef, Jörg Forrer, and Arthur Schweiger. "Longitudinally detected EPR: improved instrumentation and new pulse schemes." *Journal of Magnetic Resonance* 151, no. 1 (2001): 78-84

[2] I. Nicholson, F. Robb, D. Lurie, Imaging paramagnetic species using radiofrequency longitudinally detected ESR (LODESR imaging), J. Magn. Reson. B 104 (1994) 284–288.

[3] A. Bornet, J. Milani, B. Vuichoud, A.J. Perez Linde, G. Bodenhausen, S. Jannin, Microwave frequency modulation to enhance Dissolution Dynamic Nuclear Polarization, Chemical Physics Letters, 602 (2014) 63-67.

[4] Lê, Thanh Phong, Jean-Noël Hyacinthe, and Andrea Capozzi. "Multi-sample/multi-nucleus parallel polarization and monitoring enabled by a fluid path technology compatible cryogenic probe for dissolution dynamic nuclear polarization." *Scientific Reports* 13, no. 1 (2023): 7962.

[5] B. Reif, S.E. Ashbrook, L. Emsley, M. Hong, Nat. Rev. Methods Prim. 1 (2021) 2.

[6] E.R. Andrew, A. Bradbury, R.G. Eades, Nature 182 (1958) 1659

[7] I.J. Lowe, Phys. Rev. Lett. 2 (1959) 285.

[8] M. Schledorn, A.A. Malär, A. Torosyan, S. Penzel, D. Klose, A. Oss, M. Org, S. Wang, L. Lecoq, R. Cadalbert, A. Samoson, A. Böckmann, B.H. Meier, ChemBioChem 21 (2020) 2540.

[9] A. Böckmann, M. Ernst, B.H. Meier, J. Magn. Reson. 253 (2015) 71.

[10] A.B. Barnes, M.L. Mak-Jurkauskas, Y. Matsuki, V.S. Bajaj, P.C.A. van der Wel, R. DeRocher, J. Bryant, J.R. Sirigiri, R.J. Temkin, J. Lugtenburg, J. Herzfeld, R.G. Griffin, J. Magn. Reson. 198 (2009) 261.

[11] J.I. Kelz, J.E. Kelly, R.W. Martin, J. Magn. Reson. 305 (2019) 89.

[12] H. Vanduffel, C. Parra-Cabrera, W. Gsell, R. Oliveira-Silva, L. Goossens, R. Peeters, U. Himmelreich, B. Van Hooreweder, D. Sakellariou, W. Vanduffel, R. Ameloot, Adv. Mater. Technol. 2200647 (2022) 2200647.

[13] J.I. Kelz, J.L. Uribe, R.W. Martin, J. Magn. Reson. Open 6–7 (2021).

[14] S.J. Elliott, M. Ceillier, O. Cala, Q. Stern, S.F. Cousin, S. Jannin, J. Magn. Reson. Open 10–11 (2022).

[15] Z. Long, J. Ruthford, S.J. Opella, J. Magn. Reson. 327 (2021).

[16] F. Ellermann, A. Pravdivtsev, J.-B. Hövener, Magn. Reson. 2 (2021) 49.

[17] L. Delage-Laurin, R.S. Palani, N. Golota, M. Mardini, Y. Ouyang, K.O. Tan, T.M. Swager, R.G. Griffin, J. Am. Chem. Soc. 143 (2021) 20281.

[18] K.O. Tan, L. Yang, M. Mardini, C.B. Cheong, B. Driesschaert, M. Dincaˇ, R.G. Griffin, Chem. – A Eur. J. 13 (2022) 287.

[19] J. Xie, X. You, Y. Huang, Z. Ni, X. Wang, X. Li, C. Yang, D. Zhang, H. Chen, H. Sun, Z. Chen, Nat. Commun. 11 (2020) 1.

[20] K. Xu, O. Pecher, M. Braun, J. Schmedt auf der Günne, J. Magn. Reson. 333 (2021).

[21] P. Chen, B.J. Albert, C. Gao, N. Alaniva, L.E. Price, F.J. Scott, E.P. Saliba, E.L. Sesti, P.T. Judge, E.W. Fisher, A.B. Barnes, Sci. Adv. 4 (2018) eaau1540.

[22] C. Gao, P.T. Judge, E.L. Sesti, L.E. Price, N. Alaniva, E.P. Saliba, B.J. Albert, N.J. Soper, P.-H. Chen, A.B. Barnes, J. Magn. Reson. (2019).

[23] D. Banks, B. Michael, N. Golota, R.G. Griffin, J. Magn. Reson. 335 (2022).
[24] H. Furukawa, F. Gándara, Y.-B. Zhang, J. Jiang, W.L. Queen, M.R. Hudson, O.M. Yaghi, J. Am. Chem. Soc. 136 (2014) 4369.
[25] E.R. Andrew, A. Bradbury, R.G. Eades, Removal of Dipolar Broadening of Nuclear Magnetic Resonance Spectra of Solids by Specimen Rotation, Nature 183 (1959) 1802–1803, https://doi.org/10.1038/1831802a0.
[26] I.J. Lowe, Free induction decays of rotating solids, Phys. Rev. Lett. 2 (1959) 285–287, https://doi.org/10.1103/PhysRevLett.2.285.

2. Introduction:

Nuclear magnetic resonance (NMR) spectroscopy is a powerful method that can give insights into chemical processes and has the capability to characterize a wide variety of molecules. The simplicity of the preparation, the absence of damage to the analyte, and the moderate sample volumes needed are among the important reasons that make NMR a widely used spectroscopy method.

In 1933, it was experimentally demonstrated that certain atomic nuclei (like protons) possess spin and a magnetic moment [1, 2]. This had long been suspected since the original Stern-Gerlach experiment [3] in 1922, which proved the same characteristics for electrons [4].

The work of Rabi *et al.* [5] in 1938 led to the first observation of NMR using a beam of LiCl molecules. NMR observations on proton and deuteron beams [6] came after this impressive accomplishment (which earned Rabi the Nobel Prize in 1944), but those studies were only focused on the nuclei in small molecules operating in a molecular beam at extremely high vacuum. Two separate research groups that published their observations within a few weeks of one another in 1946 were the first to observe NMR in condensed matter. Namely, Bloch, Hansen, and Packard at Stanford [7-9] and Purcell, Torrey, and Pound at Harvard [10].

At the time, the continuous wave (CW) method was the standard for NMR observations, in which the radio frequency (RF) circuit in the apparatus was tuned to a given frequency while magnetic field strength was varied through the resonance condition. Bloch [8] suggested as an alternative method that one can expect to obtain a nuclear induction signal in the absence of an applied RF field after having suddenly perturbed the spin ensemble by the application of a short RF pulse at the resonance condition. It was Hahn who showed this method experimentally [11, 12]. In addition, he introduced spin echoes by using a sequence of pulses [13].

Nuclear magnetic resonance (NMR) is a powerful analytical technique that can provide structural information on analytes. However, its major drawback is its low sensitivity. Several methods can help overcome the low sensitivity of NMR, such as (a) optimizing the hardware: using smaller-diameter NMR coils (micro coils), increasing the magnetic field strength, and improving the coupling between the coil and the sample can enhance the signal-to-noise ratio and the intensity of the NMR signals. and (b) using hyperpolarization techniques: These techniques involve transferring the polarization of electrons to nuclei using microwave irradiation or photoexcitation, which increases the population difference between the nuclear spin levels and thus boosts the NMR signal. Examples of hyperpolarization techniques are dynamic nuclear polarization (DNP), optical pumping of noble gas, parahydrogen-induced polarization, and chemically induced dynamic nuclear polarization (CIDNP).

Dynamic nuclear polarization (DNP) consists of transferring high electron spin polarization (the unpaired electron having a gyromagnetic ratio of approximately 660 times larger than protons) to target nuclear spins with the help of microwave irradiation, which leads to a substantial nuclear polarization enhancement and hence an increase in the sensitivity of NMR spectroscopy.

In 1953, Overhauser suggested the idea of transferring polarization from electrons to nuclei in metals [14]. The work of Carver and Slichter [15] provided experimental support for this idea. They used lithium metal for their DNP experiments. Soon after, Abragam suggested the same effect in nonmetals as well [16]. The next steps in this field were mostly experimental and theoretical explorations into different DNP processes and mechanisms, starting with the work by Abragam and Proctor in 1958 [17], in which they introduced the DNP mechanism “Solid Effect” (SE). This kind of research continued well into the 1980s. During this period, numerous notable works were done by scientists like Provotorov [18, 19], Borghini [20, 21], and Abragam and Goldman [22], to name just a few, that led to the discovery and development of another DNP mechanism called “Thermal Mixing” (TM). Another mechanism called the “Cross Effect” (CE) was also introduced during this period by Hwang and Hill in 1967 [23].

At this point, the DNP studies seemed to be a field that offered few perspectives for further improvement. There were not many promising and attractive hyperpolarization applications discovered by then, mainly because achieving very low temperatures on the order of a few Kelvins was required to acquire a hyperpolarized signal. However, the frozen static sample didn’t offer well-resolved spectra, which are needed in most applications. It took a few decades until modern DNP techniques emerged thanks to technical improvements such as high magnetic fields provided by superconducting magnets and, especially, powerful microwave sources, which allowed achieving hyperpolarization while spinning a rotor at the magic angle (to obtain high resolution) at high fields and near liquid nitrogen temperatures ($90 < T < 110$ K) [24].

Such an apparatus is called magic angle spinning-DNP (MAS-DNP) and offers an attractive and useful area of DNP that is currently the subject of much new research in view of boosting the sensitivity of solid-state NMR (SSNMR). Wind and co-workers first attempted to implement an MAS-DNP setup in 1985 [25], but a lack of high-power microwave sources was an obstacle to extending DNP to higher fields [26]. It took years until MAS-DNP became popular, mainly due to the efforts of Griffin and co-workers at MIT, who performed many successful MAS-DNP experiments at high magnetic fields using gyrotrons to produce high-power microwaves [27–30]. Another big breakthrough in the field of DNP happened in 2003, when the work by Ardenkjær-Larsen *et al.* [31] demonstrated that hyperpolarization can survive a temperature jump caused by the rapid dissolution of a frozen sample at liquid helium temperatures ($1.2 < T < 4.2$ K) followed by signal acquisition in the solution state (typically > 300 K), which yields gains in sensitivity that can be as high as 104.

However, due to the lack of knowledge of the electron and nuclear spin systems, DNP has not yet reached its full potential, which is further aggravated by the decreasing efficiency of DNP in high fields over 14 Tesla. In order to optimize the efficiency of DNP, it has been shown that various factors play a crucial role, such as electron spin-lattice relaxation time, g anisotropy, electron-electron couplings, electron scattering, and nuclear spin diffusion. Studies often evaluate these parameters with pulsed EPR at the X or Q band, i.e., at lower magnetic fields, but many of the relevant EPR parameters are either field-dependent or difficult to resolve at lower magnetic fields. Therefore, to accurately evaluate the DNP parameters and characterize the spin-dynamic properties of samples containing the same concentration and solvent and subjected to the same microwave irradiation power, cryogenic temperature, and magnetic field, a dual detection capability of NMR and EPR is required.

A dual DNP/EPR probe is a device that can perform both dynamic nuclear polarization (DNP) and electron paramagnetic resonance (EPR) experiments on the same sample under the same conditions. DNP is a technique that enhances the signal of nuclear magnetic resonance (NMR) by transferring polarization from unpaired electrons to nuclei via microwave irradiation. EPR is a technique that measures the properties of unpaired electrons, such as their spin relaxation, g-factor, and spectral diffusion. A dual DNP/EPR probe can help optimize the DNP performance and understand the DNP mechanisms by measuring the parameters that affect the polarization transfer process.

While dual EPR/DNP probes would be a critical tool for DNP studies, only a handful of such instruments exist. A dual DNP/EPR probe has been designed and constructed for cryogen-free operation at high magnetic fields (14.1 T). The probe has a modular design that allows for different configurations of microwave transmission, detection, and diagnostics. The probe can perform simultaneous pulsed EPR and NMR experiments, as well as frequency-swept CW EPR and ELDOR experiments under DNP conditions. The probe can also measure the DNP frequency profile and power curve automatically. An important drawback is the lack of commercial availability of dual EPR/NMR probes and spectrometers, as well as the limited availability of high-field EPR hardware components, including solid-state microwave (μw) sources, amplifiers, and receiver systems sensitive enough to detect EPR signals. The limitations of a dual DNP/EPR probe are: (a) the complexity and cost of designing and building such a device, especially for high magnetic fields and cryogenic temperatures. (b) the limited availability of commercial components and spectrometers for high-field EPR and DNP experiments (c) the trade-off between the sensitivity and resolution of the EPR and NMR signals depends on the choice of microwave frequency, magnetic field, and sample geometry; and (d) the challenges of optimizing the microwave transmission, detection, and diagnostics for different sample systems and experimental conditions.

The limitations of a dual DNP/EPR probe can be overcome by: (a) using a cryogen-free magnet and cryostat that can provide stable and continuous operation at high magnetic fields and low temperatures without consuming

liquid helium, (b) developing and testing new components and spectrometers for high-field EPR and DNP experiments, such as solid-state microwave sources, amplifiers, receivers, and resonators, (c) designing a modular and versatile probe that can accommodate different sample geometries and configurations of microwave transmission, detection, and diagnostics, (d) implementing automated and flexible methods for measuring the DNP frequency profile, power curve, EPR spectrum, and other relevant parameters under DNP conditions, and (e) minimizing the interference and thermal effects of microwave irradiation by using appropriate shielding, filtering, and cooling techniques.

In order to easily and cost-effectively build an EPR/NMR probe, the longitudinal detected EPR technique is used here. Longitudinal detection (LOD) of EPR is based on a pickup coil aligned parallel to the static magnetic field (B_0) to measure a changing longitudinal magnetization. The measured saturation-relaxation curve is then acquired in the National Instruments (NI) data acquisition device (DAQ) for lock-in detection or in the oscilloscope for a particular microwave frequency or magnetic field. Then, it is possible to acquire the EPR by sweeping the magnetic field or the microwave frequency. The detection coil is placed orthogonally to the transmit coil and tuned to a different frequency range, which reduces the transmit crosstalk and noise. An amplitude modulation of the microwave can periodically saturate the electron magnetization by modulating longitudinal magnetization. The resulting time-dependent longitudinal magnetization then induces an alternating voltage in the EPR coil with an axis parallel to B_0.

The advantages LOD-EPR has over a conventional EPR setup are: (a) LOD-EPR can detect fast-decaying signals in the nanosecond or even sub-nanosecond range, which are difficult to measure by conventional EPR due to instrument dead time or low SNR; and (b) it can have superior resilience against transmit crosstalk and noise by placing the receive coil orthogonal to the transmit coil and tuning it to a different frequency range.

Reference:

[1] R. Frisch, O. Stern, Über die magnetische Ablenkung von Wasserstoffmolekülen und das magnetische Moment des Protons. I, Zeitschrift für Physik, 85 (1933) 4-16.
[2] I. Estermann, O. Stern, Über die magnetische Ablenkung von Wasserstoffmolekülen und das magnetische Moment des Protons. II, Zeitschrift für Physik, 85 (1933) 17-24.
[3] W. Gerlach, O. Stern, Der experimentelle Nachweis der Richtungsquantelung im Magnetfeld, Zeitschrift für Physik, 9 (1922) 349-352.
[4] E.D. Becker, A Brief History of Nuclear Magnetic Resonance, Analytical Chemistry, 65 (1993) 295A- 302A.
[5] I.I. Rabi, J.R. Zacharias, S. Millman, P. Kusch, A New Method of Measuring Nuclear Magnetic Moment, Physical Review, 53 (1938) 318-318.
[6] J.M.B. Kellogg, I.I. Rabi, N.F. Ramsey, J.R. Zacharias, The Magnetic Moments of the Proton and the Deuteron. The Radiofrequency Spectrum of H2 in Various Magnetic Fields, Physical Review, 56 (1939) 728- 743.
[7] F. Bloch, W.W. Hansen, M. Packard, Nuclear Induction, Physical Review, 69 (1946) 127-127.
[8] F. Bloch, Nuclear Induction, Physical Review, 70 (1946) 460-474.
[9] F. Bloch, W.W. Hansen, M. Packard, The Nuclear Induction Experiment, Physical Review, 70 (1946) 474-485.
[10] E.M. Purcell, H.C. Torrey, R.V. Pound, Resonance Absorption by Nuclear Magnetic Moments in a Solid, Physical Review, 69 (1946) 37-38.
[11] E.L. Hahn, An Accurate Nuclear Magnetic Resonance Method for Measuring Spin-Lattice Relaxation Times, Physical Review, 76 (1949) 145-146.
[12] E.L. Hahn, Nuclear Induction Due to Free Larmor Precession, Physical Review, 77 (1950) 297-298.
[13] E.L. Hahn, Spin Echoes, Physical Review, 80 (1950) 580-594.
[14] A.W. Overhauser, Polarization of Nuclei in Metals, Physical Review, 92 (1953) 411-415.
[15] T.R. Carver, C.P. Slichter, Experimental Verification of the Overhauser Nuclear Polarization Effect, Physical Review, 102 (1956) 975-980.
[16] A. Abragam, Overhauser Effect in Nonmetals, Physical Review, 98 (1955) 1729-1735.
[17] A. Abragam, W.G. Proctor, Une Nouvelle Methode De Polarisation Dynamique Des Noyaux Atomiques Dans Les Solide, Comptes rendus de l'Académie des Sciences, 246 (1958) 2253-2256.
[18] B.N. Provotorov, A quantum-statistical theory of cross relaxation, Soviet Physics JETP, 15 (1962) 611- 614.
[19] B.N. Provotorov, Magnetic resonance saturation in crystals, Soviet Physics JETP, 14 (1962) 1126-1131.
[20] M. Borghini, Spin-Temperature Model of Nuclear Dynamic Polarization Using Free Radicals, Physical Review Letters, 20 (1968) 419-421.
[21] M. Borghini, Nuclear spin relaxation and dynamic polarization versus electron spin-spin relaxation, Physics Letters A, 26 (1968) 242-244.
[22] A. Abragam, M. Goldman, Principles of dynamic nuclear polarisation, Reports on Progress in Physics, 41 (1978) 395-467.

[23] C.F. Hwang, D.A. Hill, New Effect in Dynamic Polarization, Physical Review Letters, 18 (1967) 110-112.
[24] V.A. Atsarkin, Dynamic nuclear polarization: Yesterday, today, and tomorrow, Journal of Physics: Conference Series, 324 (2011) 012003.
[25] R.A. Wind, M.J. Duijvestijn, C. van der Lugt, A. Manenschijn, J. Vriend, Applications of dynamic nuclear polarization in ^{13}C NMR in solids, Progress in Nuclear Magnetic Resonance Spectroscopy, 17 (1985) 33-67.
[26] A.B. Barnes, G.D. Paëpe, P.C. van der Wel, K.N. Hu, C.G. Joo, V.S. Bajaj, M.L. Mak-Jurkauskas, J.R. Sirigiri, J. Herzfeld, R.J. Temkin, R.G. Griffin, High-Field Dynamic Nuclear Polarization for Solid and Solution Biological NMR, Applied Magnetic Resonance, 34 (2008) 237-263.
[27] D.A. Hall, D.C. Maus, G.J. Gerfen, S.J. Inati, L.R. Becerra, F.W. Dahlquist, R.G. Griffin, Polarizationenhanced NMR spectroscopy of biomolecules in frozen solution, Science, 276 (1997) 930-932.
[28] A.B. Barnes, B. Corzilius, M.L. Mak-Jurkauskas, L.B. Andreas, V.S. Bajaj, Y. Matsuki, M.L. Belenky, J. Lugtenburg, J.R. Sirigiri, R.J. Temkin, J. Herzfeld, R.G. Griffin, Resolution and polarization distribution in cryogenic DNP/MAS experiments, Physical Chemistry Chemical Physics, 12 (2010) 5861-5867.
[29] M. Rosay, L. Tometich, S. Pawsey, R. Bader, R. Schauwecker, M. Blank, P.M. Borchard, S.R. Cauffman, K.L. Felch, R.T. Weber, R.J. Temkin, R.G. Griffin, W.E. Maas, Solid-state dynamic nuclear polarization at 263 GHz: spectrometer design and experimental results, Physical Chemistry Chemical Physics, 12 (2010) 5850- 5860.
[30] R.G. Griffin, T.F. Prisner, High field dynamic nuclear polarization—the renaissance, Physical Chemistry Chemical Physics, 12 (2010) 5737-5740.
[31] J.H. Ardenkjær-Larsen, B. Fridlund, A. Gram, G. Hansson, L. Hansson, M.H. Lerche, R. Servin, M. Thaning, K. Golman, Increase in signal-to-noise ratio of > 10,000 times in liquid-state NMR, Proceedings of the National Academy of Sciences of the United States of America, 100 (2003) 10158.

3. **Continuous Wave EPR Spectroscopy:**

Since the beginning of magnetic resonance spectroscopy, modulation of the static magnetic field and phase-sensitive detection have been used to reduce the noise of weak continuous-wave (CW) signals [1]. In contrast to nuclear magnetic resonance (NMR), where pulsed techniques have long replaced continuous wave techniques, the latter are still frequently used in electron paramagnetic resonance (EPR) experiments.

The beginning of World War II called for efficient radar technology, which led to the development of an instrument that made it possible to detect EPR signals. In 1945, Zavoisky [2] made the first observation of the electron paramagnetic resonance signal. He detected a radio-frequency absorption line for the sample. He observed a magnetic resonance signal at a magnetic field of 4.76 mT at a frequency of 133 MHz. Zavoisky's results were interpreted by Frenkel [2] as electron paramagnetic resonance absorption.

After World War II, EPR studies were undertaken in the United States by Cummerow and Halliday [3] and in England by Bagguley and Griffiths [4]. Improved microwave systems enabled spectrometers to operate at higher fields and commercially become available from manufacturers. One remarkable accomplishment in recent years was the observation of an EPR signal from a single electron held in space by a combination of applied electric and magnetic fields (in a so-called Penning trap) [5].
Fig. 14 shows the "microwave bridge" that comprises the microwave source, the detector, and the resonant cavity that contains the sample. In conventional EPR, the spectra are recorded by putting the sample in the cavity. The microwave is sweeping the external magnetic field while irradiating the sample at a constant frequency. The microwave is transferred to the cavity through waveguides and a circulator. Because of the critical coupling, the resonator completely absorbs the incoming microwave radiation. Additional absorption causes the resonator to detune, and the microwave is reflected through the waveguide and circulator to the detector. The reflected power is taken as a function of the magnetic field to get the EPR spectrum. The magnetic field is usually modulated at a frequency of 100 kHz to increase the signal-to-noise (SNR) ratio, and this gives the first derivative spectra.

The general outlay of the EPR spectrometer is shown in Figures- 11 and 12.

Fig. 11: BRUKER EPR Spectrometer with the microwave bridge, magnet, and electronics console.

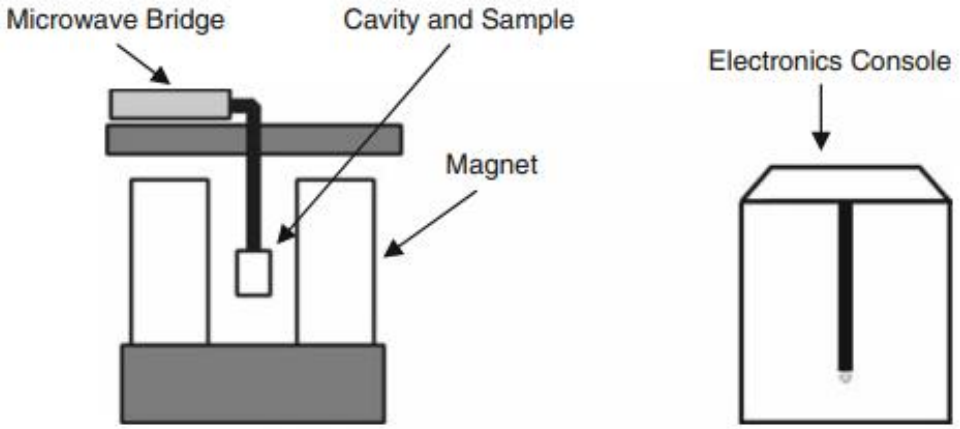

Fig. 12: The general outlay for an EPR spectrometer consists of the microwave bridge, cavity, magnet, and electronics console.

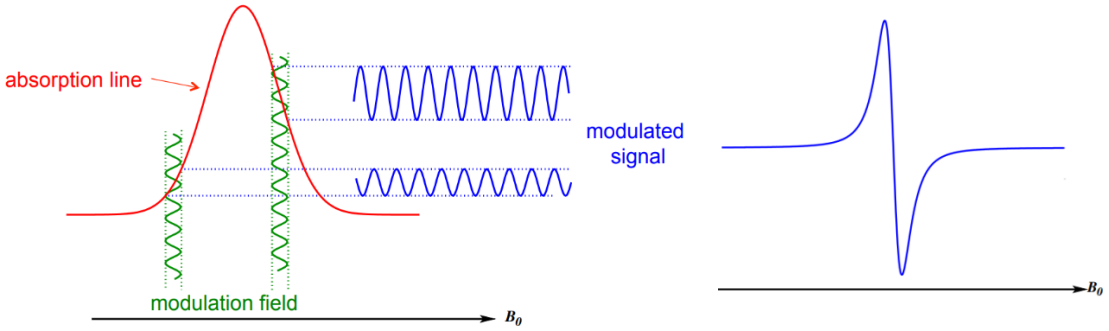

Fig. 13: The amplitude modulation of the field and the first derivative of the EPR spectra.

3.1 The different components of an EPR spectrometer:

In this section, a detailed description of the different components of the EPR spectrometer is given below.

3.1.1 The Microwave Bridge:

In this section, we only review the most important components of the microwave bridge and will not detail other parts such as the power supply, the control system, or other security electronics. As written above, the microwave bridge houses the microwave source and the detector. A detailed picture of the microwave bridge is shown in Fig. 14. Even though there are other components in the bridge, like the power supply, control system, and other security electronics, in this section only the most important components will be discussed.

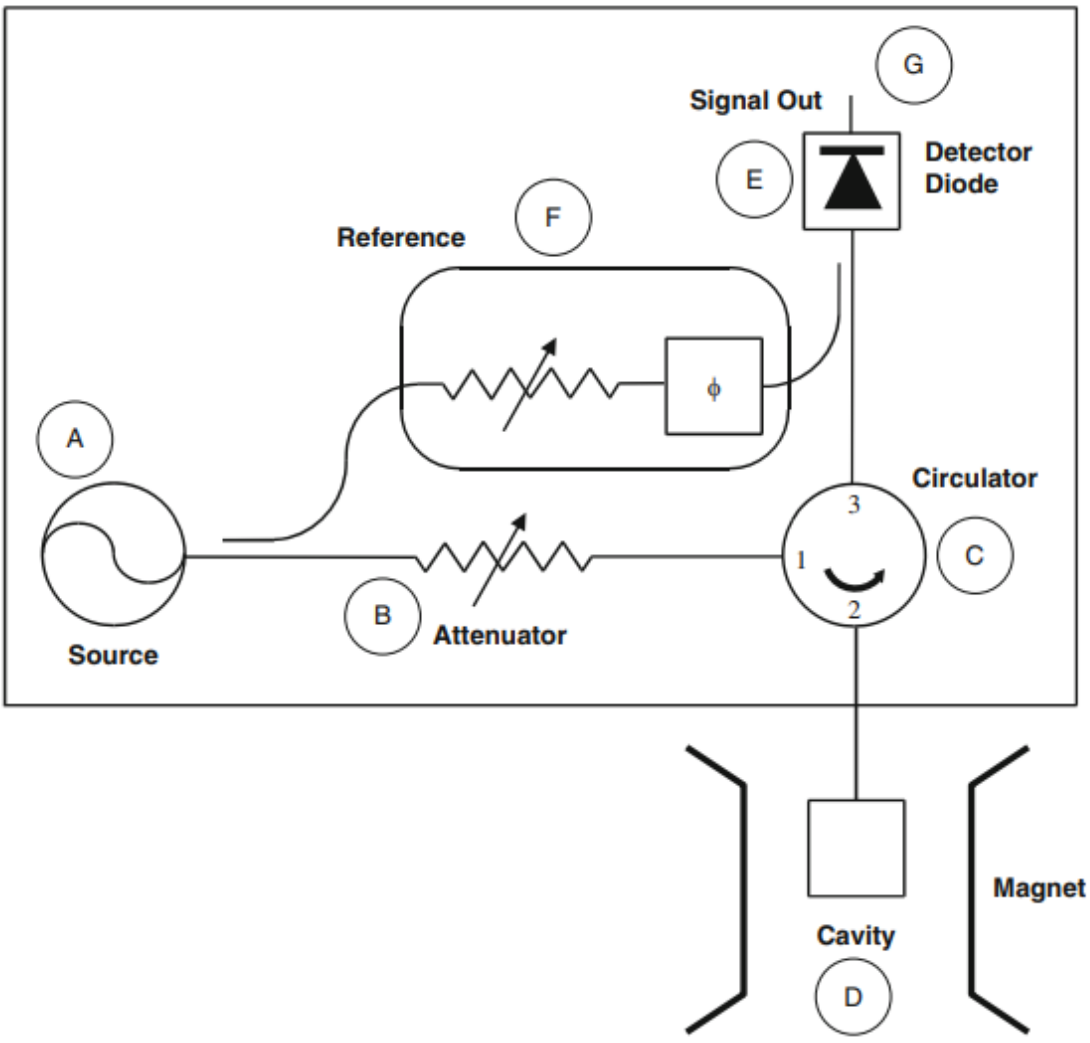

Fig. 14: Block diagram for the microwave bridge with the source, circulator, reference arm, and detector diode mentioned in the figure.

The microwave source, denoted by ‘A’ in the block diagram, is a solid-state device (a gun diode), which has replaced the formerly used klystron tubes. The variable attenuator (B) is used to control the microwave power accurately, in particular to avoid saturating the sample.

EPR spectroscopy is dependent on the reflected power. Indeed, one measures the changes in the amount of radiation reflected from the microwave cavity containing the sample (point ‘D’ in the figure). Therefore, the detector should only see the microwave radiation traveling back from the cavity through the circulator (point ‘C’ in the figure). The role of the circulator is thus to allow for the incoming microwaves through port 1 to only reach the cavity through port 2 and not the detector, which is attached to port 3. Conversely, the reflected microwaves are directed only to the detector (port 3) and isolated from the microwave source.

In commercial Bruker spectrometers, Schottky diodes are used as detectors. The diode absorbs the reflected microwave power and converts it to an electrical current. At low power levels (less than ~ 1 mW), the diode current is proportional to the microwave power, and the diode behaves as a square-law detector. At higher power levels (greater than ~ 1 mW), the diode current is proportional to the square root of the microwave power, so that the detector is a linear detector. The transition between the two regions is gradual. To ensure that the detector operates in the linear range, a so-called reference arm (point ‘F’ in Fig. 14) is used that supplies the detector with extra microwave power, or "bias." Some of the source power is tapped off into the reference arm, where a second attenuator controls the power level (and consequently the diode current) for optimal performance. A phase shifter is also necessary to ensure that the microwave coming from the reference arm is in phase with the reflected microwave signal when both are combined at the detector diode.

The detector diodes are very sensitive to damage from excessive microwave power and tend to lose their sensitivity with time. To prevent this from happening, there is protection circuitry in the bridge that monitors the current from the diode. When the current exceeds 400 mA, the bridge automatically protects the diode by lowering the microwave power level. This reduces the risk of damage due to accidents or improper operating procedures.

3.1.2 **The EPR Cavity:**

This section discusses the properties of microwave (EPR) cavities and how these are altered due to absorption, resulting in the EPR signal. Resonators are used to amplify weak signals from the sample. Without loss of generality, the resonator can be thought of as a mere cavity, i.e., a metal box of rectangular or cylindrical shape that is in resonance with the microwave frequency used. However, other resonant devices have been proposed for EPR spectroscopy (Poole 1967). Resonance means that the cavity stores microwave energy. Therefore, at the resonance frequency of the cavity, microwaves remain inside the cavity and are not reflected.

Cavities are characterized by their quality factor Q, which indicates how efficiently the cavity stores microwave energy. As Q increases, the sensitivity of the spectrometer increases.

A consequence of resonance is that there will be a standing wave inside the cavity. Standing electromagnetic waves have their electric and magnetic field components exactly out of phase, i.e., where the magnetic field is maximum, the electric field is minimum, and vice versa.

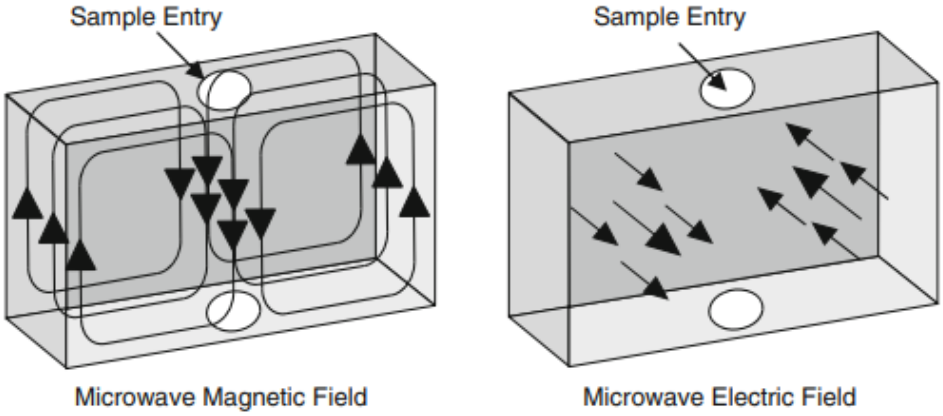

Fig. 15: A sketch of the magnetic and electric field patterns in a microwave cavity.

The spatial distribution of the amplitudes of the electric and magnetic fields in the commonly used EPR cavity (the TE_{102} cavity) is shown in Fig. 15. The spatial separation of the electric and magnetic fields in a cavity is used to great advantage. Most samples have non-resonant absorption of the microwaves via the electric field (this is how a microwave oven works), and Q is degraded by an increase in the dissipated energy.

The microwave's magnetic field drives the absorption in EPR. Therefore, if the sample is placed between the microwave electric field minimum and the magnetic field maximum, the biggest signals and the highest sensitivity are achieved. Cavities are designed to provide optimal placement of the sample. Microwaves are coupled into the cavity via a hole called an iris. The size of the iris controls how much of the microwave power is reflected from the cavity and how much enters the cavity. The iris accomplishes this by carefully matching or transforming the impedances (the resistance to the waves) of the cavity and the waveguide (a rectangular pipe used to carry microwaves). An iris screw in front of the iris allows the user to adjust the "matching." When impedances are matched, the resonator is said to be "critically coupled." This adjustment can be visualized by noting that as the screw moves up and down, it effectively changes the size of the iris.

When a sample is placed inside the cavity, the impedance of the latter is altered (if, for instance, the sample absorbs microwave energy), and the coupling of the cavity with the transmission line is also altered. The Q-factor also decreases due to increased losses. In this case, the cavity is no longer critically coupled, and microwaves are reflected to the bridge, resulting in an EPR signal.

3.1.3 **The Signal Channel:**

EPR spectroscopists use a technique known as phase-sensitive detection to enhance the sensitivity of the spectrometer. In this approach, the EPR signals are made distinguishable from the various sources of noise or interference. The encoding helps to decrease the impact of noise from the detection diode and

eliminate baseline instabilities due to drift in the electronic devices. The signal channel, a unit in the spectrometer console, contains the electronics required for phase-sensitive detection.

The detection scheme works as follows: The magnetic field strength that the sample sees is varied sinusoidally at the modulation frequency (usually 100 kHz). If there is an EPR signal, the field modulation quickly sweeps through part of the signal, and the amplitude of microwaves reflected from the cavity is modulated at the same frequency. For an EPR signal that is approximately linear over an interval as wide as the modulation amplitude, the EPR signal is transformed into a sine wave with an amplitude that is proportional to the slope of the signal. The signal channel (more commonly known as a lock-in amplifier or phase-sensitive detector) produces a DC signal that is proportional to the amplitude of the modulated EPR signal. It compares the modulated signal with a reference signal having the same frequency as the field modulation, and it is only sensitive to signals that have the same frequency and phase as the field modulation. Any signals (such as noise and electrical interference) that do not fulfill these requirements are suppressed. To further improve the sensitivity, a time constant is used to filter out more of the noise.

Phase-sensitive detection with magnetic field modulation increases the sensitivity by several orders of magnitude; however, the user must be careful in choosing the appropriate modulation amplitude, frequency, and time constant. A poor choice of any of these variables can distort the EPR signals and make interpretation of the results difficult.

3.1.4 **The Magnetic Field Controller:**

The magnetic field controller defines the center field and sweeps the magnetic field for signal acquisition. It consists of two parts: a digital part that defines the field values and the timing of the field sweep, and an analog part that regulates the current in the windings of the magnet to attain the requested magnetic field value. A microprocessor in the controller controls the setting of the magnetic field and the timing of the magnetic field sweep. In older Bruker field controllers, a field sweep is divided into a maximum of 4,096 discrete steps (12-bit accuracy) called sweep addresses. Newer instruments will have higher resolution. At each step of the field sweep, a reference voltage corresponding to the magnetic field value is sent to the part of the controller that regulates the magnetic field. The sweep rate is controlled by varying the waiting time between the individual steps.

The magnetic field regulation is achieved using a Hall probe placed in the gap of the magnet. It produces a voltage that is dependent on the component of the magnetic field that is perpendicular to the probe. The relationship between field and voltage is not linear, and the voltage changes with temperature; however, this is easily compensated for by keeping the probe at a constant temperature slightly above room temperature and characterizing the nonlinearities so that the microprocessor in the controller can make the appropriate corrections. Regulation is accomplished by comparing the voltage from the Hall probe with the reference voltage given by the other part of the controller. When the two voltages are different, a correction voltage is sent to the magnet power supply, which changes the amount of current flowing

through the magnet windings and hence the magnetic field. Eventually the error voltage drops to zero and the field is "stable" or "locked." This voltage comparison occurs at each discrete step of a magnetic field scan.

3.1.5 **Application of CW EPR Spectroscopy:**

For any kind of analytical technique, methodology and application go side by side, and their progress can be summarized by creating a 2-dimensional diagram. In Fig. 16, we showed a 3-dimensional diagram where the z-axis depicts the current CW EPR methods, the y-axis represents the typical application, and the x-axis shows possible areas that are currently being explored.

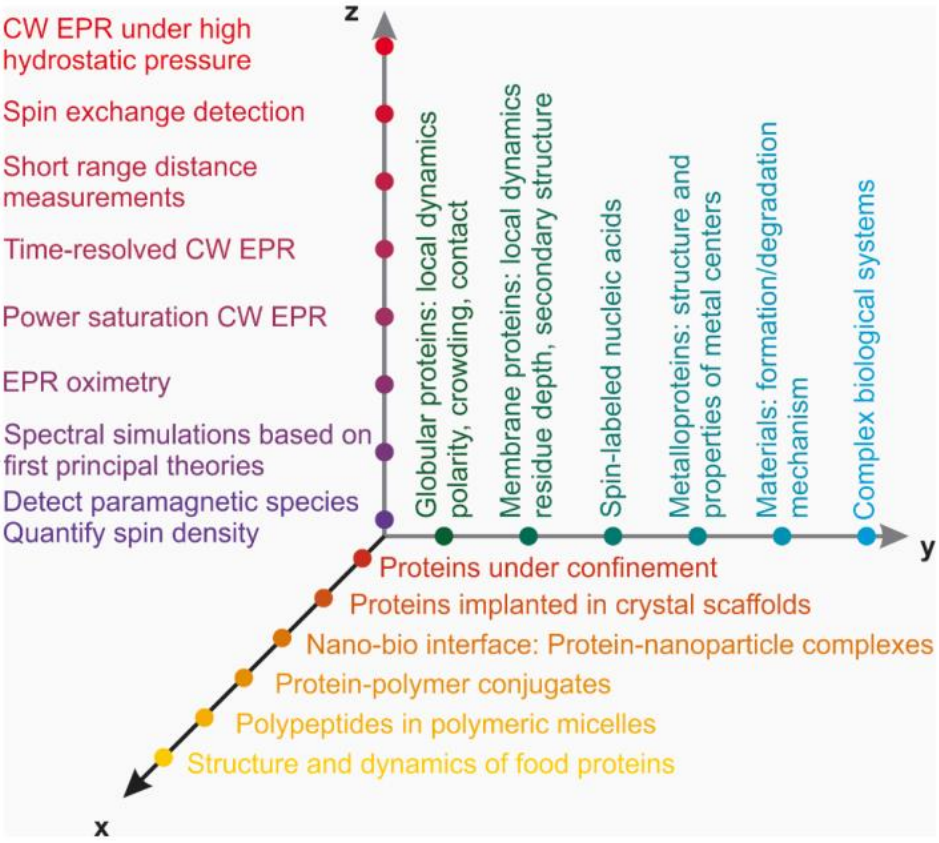

Fig. 16: Diagram of the current CW EPR methodology (z-axis), typical applications (y-axis), and new areas being explored (x-axis).

Information obtained from a CW EPR experiment includes the nature of a paramagnetic species center (metals or radicals), the quantity of the present paramagnetic species, and the influence of the environment on the species [6–8]. Aside from being sensitive to single electrons, EPR has another unique benefit: it can isolate and study only the single electrons, no matter what nuclei are nearby or what phase the sample is in (the dielectric losses of samples in a watery environment at room temperature, and therefore the properties of the electric dipoles of the water molecules, must be minimized by reducing the sample volume). The acquired spectra can be analyzed using software packages like EasySpin [29]. CW EPR can also be used in a time-resolved mode, allowing the processes to be monitored in real time. In combination with the power saturation, the CW EPR can be

used to probe the spin-lattice relaxation [30, 31]. EPR oximetry can be used for the detection of the collision of nitroxide with molecular oxygen, which reflects the local polarity [32, 33]. CW EPR is also sensitive to spin exchange interaction and distance measurement between spins in proximity [34].

With the advancement of EPR methodology, the range of EPR applications has extended and diversified. CW EPR can be used to probe the local dynamics of globular and membrane proteins. It can also be used to retrieve information about the depth of protein residues buried inside the cell membrane bilayer and the helical structure of the transmembrane domain based on oxygen [35, 36]. Both nucleic acids and polymers can be spin-labeled, and the CW EPR can be used to probe information regarding local dynamics and polarity. It can also be used to probe the metal centers in the metalloprotein without using artificial spin labeling [37, 38].

3.2 **Limitations of CW EPR:**

Even though CW EPR has a broad range of advantages, like its sensitivity and resolution, there are some limitations too. One of the limitations is that it can't perform pulse experiments like ENDOR and ELDOR. The microwave resonator's bandwidth and quality factor, which limit the available microwave frequency and magnetic field, are its limitations. Instrumentation limitations have become critical in higher fields and high power, where most of the microwave components are either very expensive or not available.

3.3 **Longitudinal Detection of EPR:**

With the recent development of high-frequency microwave technology, dynamic nuclear polarization (DNP) has become one of the most versatile hyperpolarization techniques for nuclear magnetic resonance (NMR). DNP is used to enhance the signal intensities of the NMR spectra. Usually, DNP experiments are performed in high fields for better resolution. To better understand several fundamental and other aspects of DNP, it is important to gather information not only on relaxation and nuclear polarization buildup time constants but also on relaxation properties of the electron spin system itself, preferably on conditions as closely matched to the DNP experiment as possible. However, while the MW channel in most polarizers is designed for high power, it does not provide the frequency and power stability necessary to perform EPR experiments with heterodyne detection. Also, the limitation of microwave detectors at higher frequency ranges restricts traditional EPR operations.

In 2001, Arthur Schweiger created longitudinal detection of EPR (LOD EPR) to perform EPR [9, 10]. In this thesis, we have extended this technique and merged it with the existing DNP technique to develop a DNP/EPR probe for high-field instruments. In longitudinal detection of EPR, a solenoid pickup coil is aligned parallel to the static magnetic field and is therefore sensitive to the changes in magnetic flux along this direction. The signal is thus measured via the voltage induced in the pickup coil by the changes in longitudinal magnetization. In our experiments, the microwave is amplitude modulated (AM). The microwave gate changes the magnetization of the pickup coil. Sweeping the microwave frequency or magnetic field allows for the acquisition of the EPR spectra.

In the LOD-EPR setup, the excitation and detection circuits are independent and well isolated from each other. The excitation and detection frequencies are usually a few orders of magnitude apart from each other. This allows for low-frequency signals to be detected, while high-power microwaves can be used for sample irradiation [9]. This robustness allows proper optimization of different parts, like the microwave channel, which can be modified for high power, while the detection circuit can be modified for wide bandwidth, high sensitivity, and sample fluctuations [11].

LOD has been previously shown to work for a wide range of excitation frequencies, from the MHz [12] to the GHz scales. While excitation is performed at high frequency, the detection operates from HZ to tens of kHz. In our experiments, the experiments are usually performed at a detection frequency below 10 Hz. Since the detection circuit works at audio or radio frequency, it is easier to setup compared to the common heterodyne EPR detectors working at the same mW frequency as used for excitation.

3.4 **LOD EPR Circuit:**

The LOD EPR circuit consists of multiple sub-units. A detailed description of the sub-units is given below.

3.4.1 **Detection Circuit:**

The detection circuit [13] is made up of a CFP outer capillary (B) and a dynamic sealing (C). This lets the sample be loaded into the polarizer in the same way that the sample stick is loaded into a normal dissolution DNP setup. The detection coil is a 600-turn copper wire split solenoid made of 0.1 mm enameled copper wire wound around a PEEK coil former (E). A small gap allows the microwaves to reach the sample. The bottom portion of the coil former has an outer diameter of 7.5 mm, which is small enough to enter the NMR coil of the DNP insert. Up to 120 µL of sample can be loaded into the sample cup (F). The latter slides and locks inside the coil former. The coil former is permanently screwed to the vial top part (D).

The two ends of the detection coil are routed inside the coil former and soldered to a twisted pair of silver-plated copper wires that run upwards through the black capillary to carry the signal out of the polarizer. Electrical connections are provided at the outer end of the probe (A). The pickup coil (600 turns using 0.1 mm-diameter copper wire) is aligned parallel to the static magnetic field. The coil is non-resonant and well isolated from the ground to reduce crosstalk with the power modulation signal.

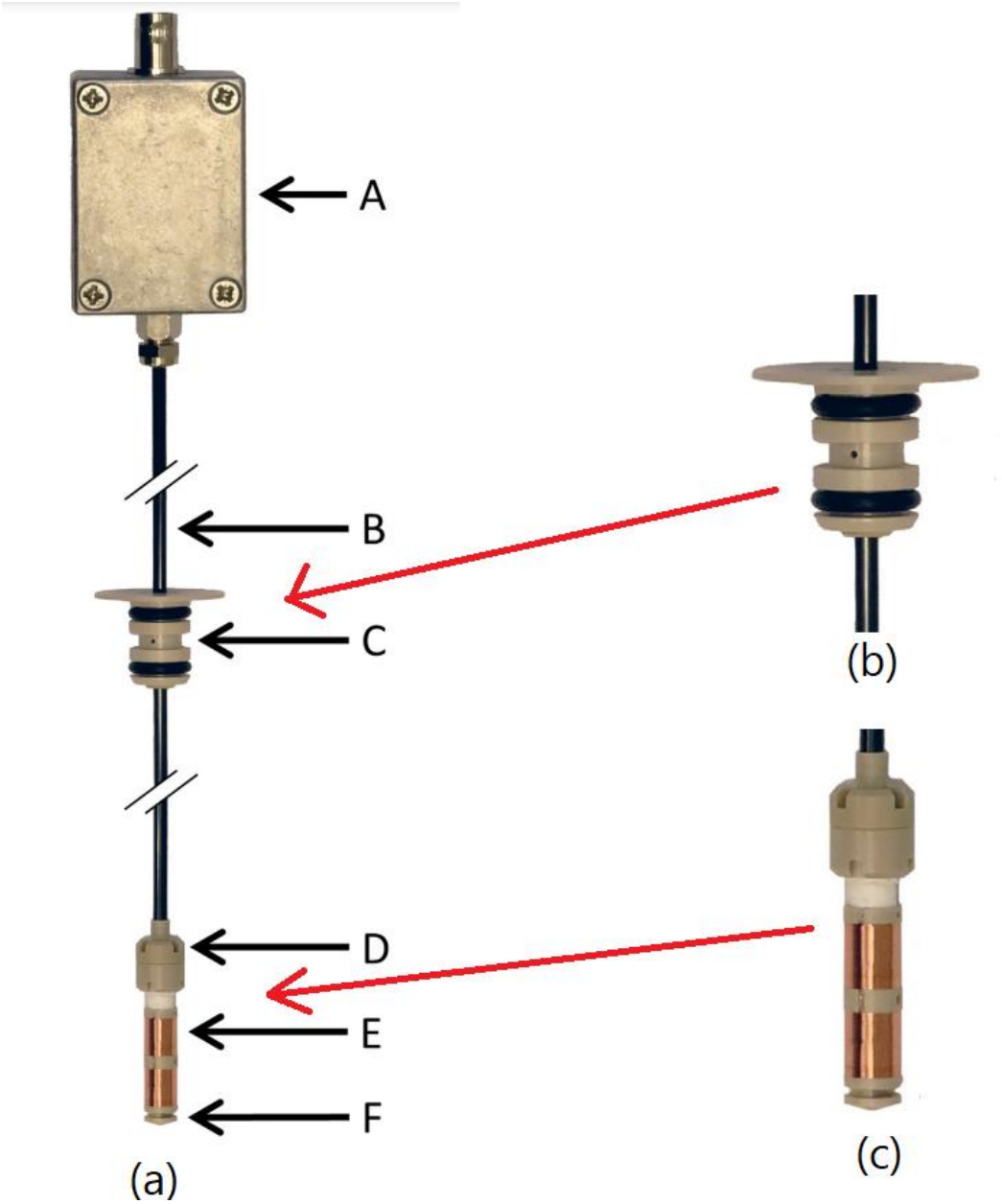

Fig. 17: (a) The probe is composed of the following elements: a leak-tight connection box that transforms the twisted pair carrying the signal to a BNC Twinax connector (A); a CFP 1/800 outer capillary (B) with its dynamic sealing (C) and laser-welded vial top-part (D); a coil former supporting a 600-turn spit solenoid (E); a sample cup (F). (b) and (c) depict the enlarged form of the dynamic sealing and the pickup coil. In Fig. (b), the gap for the microwave can be clearly seen.

Two types of hardware setups for the measurement of signals are shown here. (1) The first one involves connecting the pickup coil directly to an audio differential preamplifier, then adding a 10 Hz low-pass filter. And the signal is measured using an NI data acquisition device (DAQ). The amplitude modulation (AM) is produced by the NI DAQ 6001 before it is fed to the microwave source. To periodically saturate the electrons, a square wave is generated for the AM modulation by the DAQ and fed to the microwave source. Its amplitude controls how much the attenuator at the MW outlet is opened. At a maximum of 5 V, the total available power is delivered. The total microwave power that the AnaPico synthesizer can produce is 100 mW.

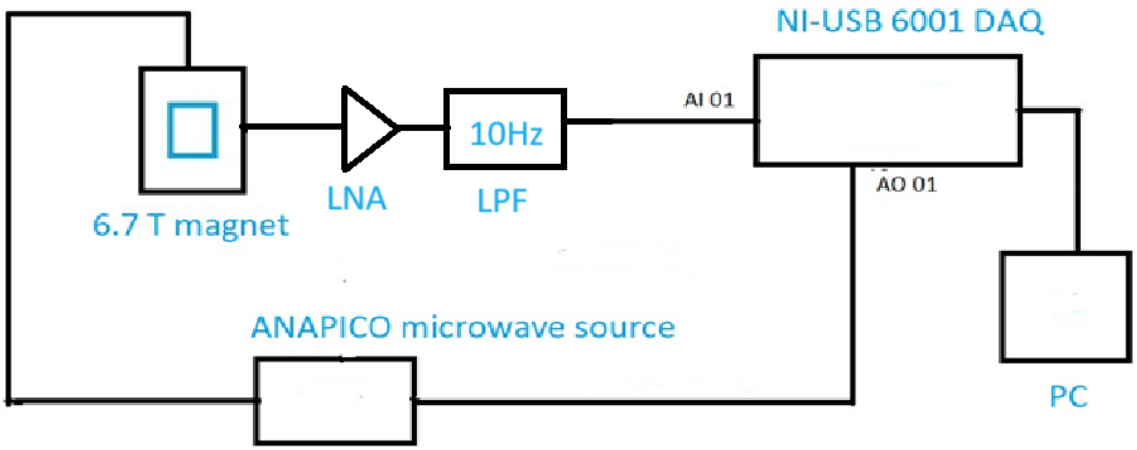

Fig. 18: LOD EPR setup using an audio low-noise amplifier with a 10 Hz low-pass filter; and the acquisition is done using a National Instruments (NI) data acquisition device (DAQ).

3.4.1.1 **Implementation of LabVIEW:**

Control of LOD measurements was entirely implemented in LabVIEW (National Instruments). The modulation speed is controlled by the frequency of the NI DAQ-generated square wave applied to the source. After the amplifier, the NI DAQ card uses one of its ports (AI01) to acquire the signal. The data handling system samples the signal with a frequency of 5000 Hz on the AI01 input. To suppress noise sources further, the signal is low-pass filtered with a digital fourth-order 10 Hz low-pass Bessel filter.

The synchronous detector is built with the square wave source, the multiplier, a low-pass filter, and the phase shifter. Because the source is a square wave generator, it detects all odd harmonics in the signal from the detector coil. Higher-order harmonics will be strongly attenuated thanks to signal filtering. The square wave source controls the MW power level via a phase shifter. The control signal to the MW attenuator input is also sampled at 5000 Hz. The output from the multiplier is low-pass filtered with a digital fourth-order 0.1 Hz Bessel low-pass filter to remove all unwanted signals except the DC signal. The signal from the low-pass filter is plotted on a graph, averaged down to one sample per source period, and stored in a file.

In the second setup, the pickup coil is connected to a low-noise audio differential preamplifier, like in the previous setup. But here, this amplifier is connected to a Stanford Research System (SRS) preamplifier. In this setup, no physical low-pass filter is used; instead, the low-pass filter function of the SRS preamplifier is used. The signal is then measured on the oscilloscope. The square wave signal for the amplitude modulation (AM) is generated using a function generator. The signal that is used for AM is also connected to another port of the oscilloscope. This signal is used as the trigger signal. The oscilloscope is connected directly to the PC and Raspberry Pi. The function generator and the microwave source are controlled using the Raspberry Pi via a Python script. In this setup, the entire process is automated, and the frequency of the microwave and the acquisition and saving of data are done

automatically. The low-pass filter used in the SRS preamplifier is 10 Hz. A detailed schematic is shown in Fig. 19.

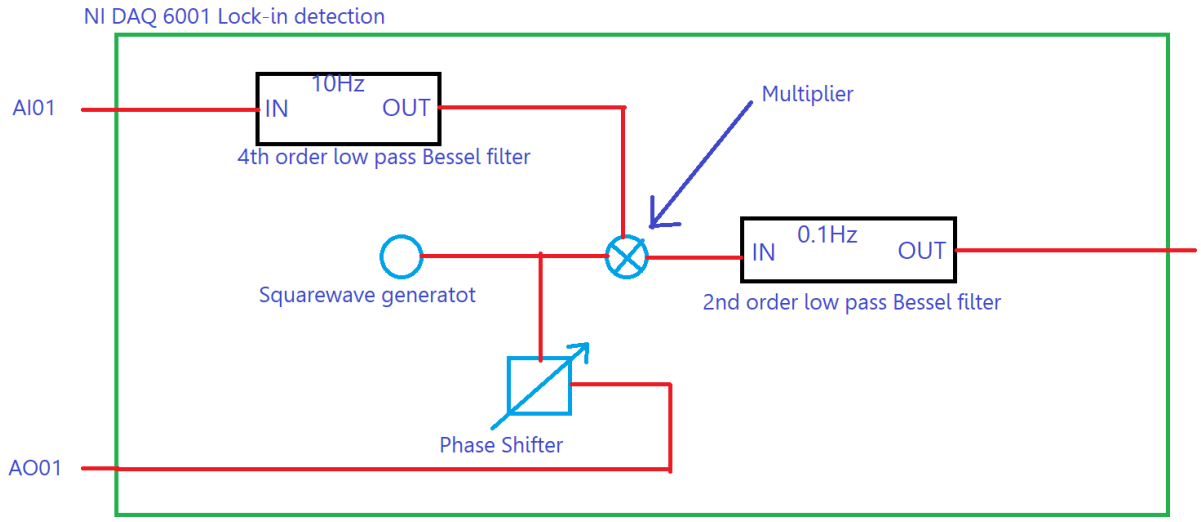

Fig. 19: The LabVIEW program is for the acquisition and measurement of EPR signals.

In Fig. 21, the induced LOD EPR signal shows the saturation recovery signal expected from the LOD EPR setup. The LOD signal intensity is proportional to the first-time derivative of the electron magnetization, i.e., the electron longitudinal relaxation rate and the saturation efficiency. The signal is usually averaged using the averaging function of the oscilloscope, and for the signal intensity, the peak-to-peak value is recorded. The averaging is required to improve the signal-to-noise ratio and provide accurate data.

The LabView control panel is shown in Fig. 20. The data acquisition is done here. The parameters we usually use are the amplitude modulation (AM) frequency and the two-digital low-pass Bessel filter, whose cutoff frequency is changed according to the AM frequency. The sample rate for all our experiments is set at 5 kHz, which is the maximum input sample rate of the National Instruments (NI) USB-6001 device. The “V ON” and “V OFF” are kept at 4.6 V and 0 V, respectively, for most of our microwave sources. The program can be terminated using the “Stop” button.

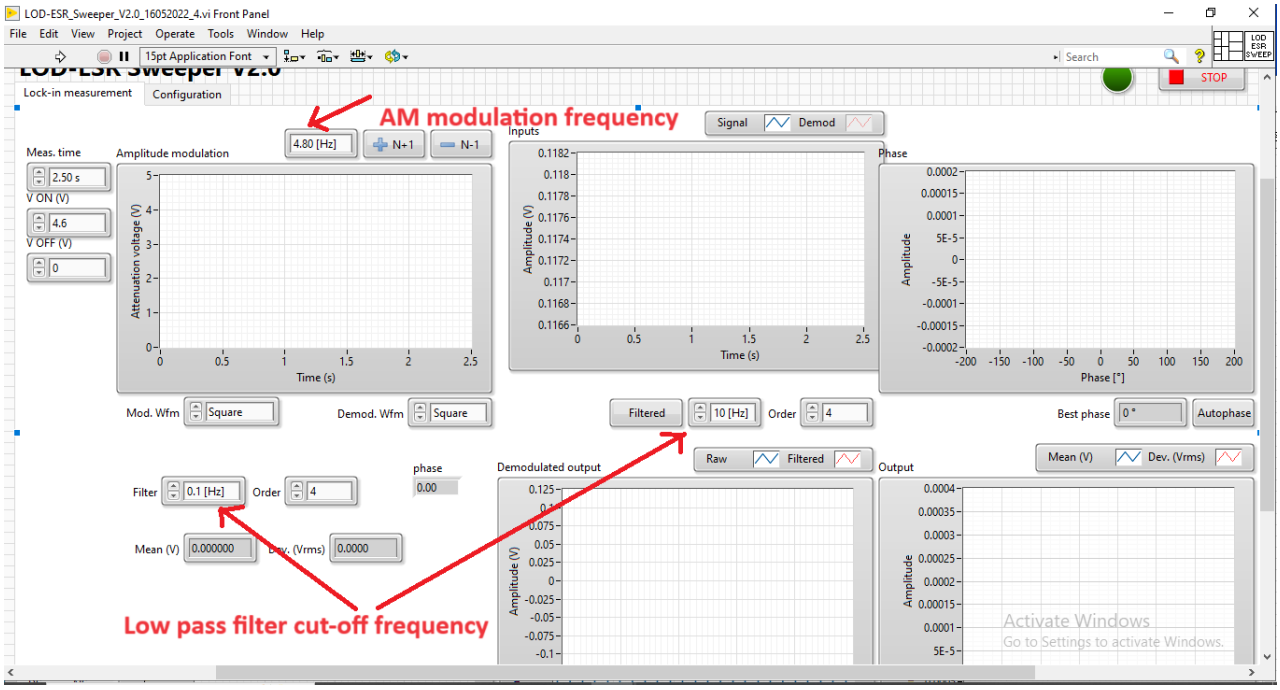

Fig. 20: LabView control panel for the LOD EPR data acquisition. The AM frequency and the low-pass filter cut-off frequency are shown in the picture.

The LOD-EPR signal using the normal low-noise amplifier and analog 10 Hz low-pass filter is shown in the following Fig. 21.

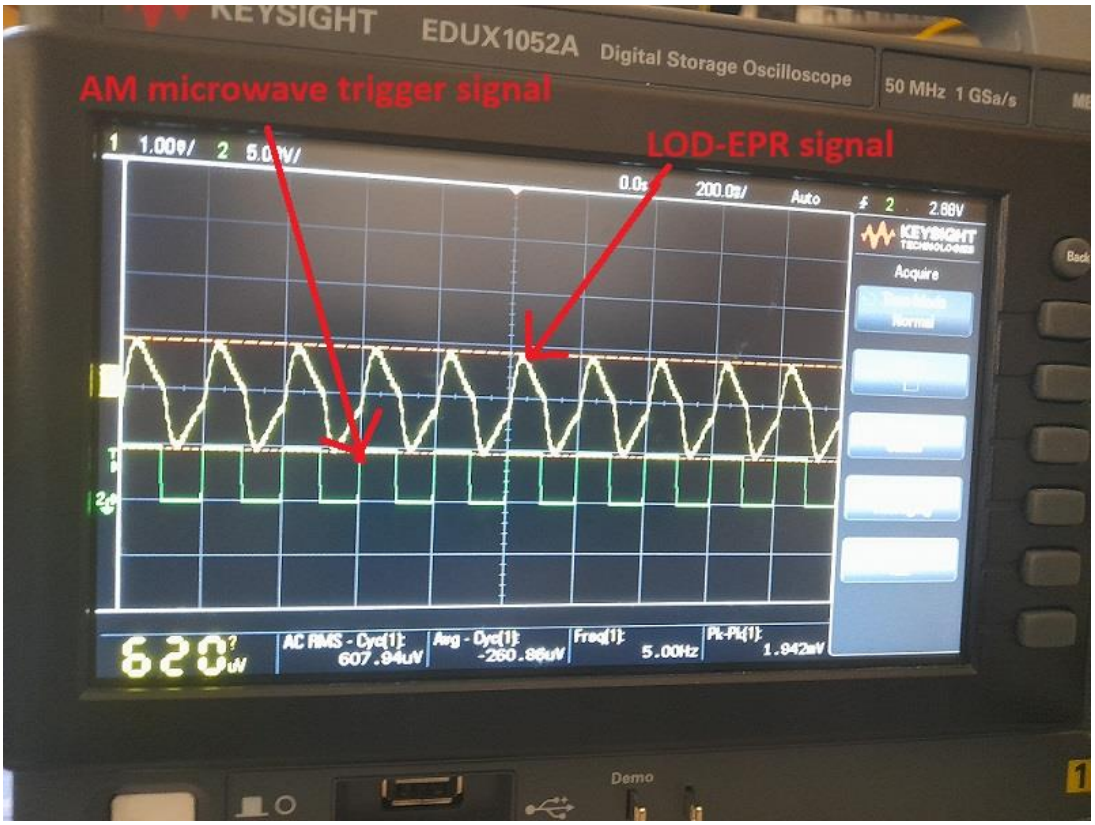

Fig. 21: The acquired LOD EPR signal for a particular microwave frequency and the microwave trigger/AM signal generated by the function generator using the normal amplifier and low-pass filter.

In the next section, we will talk about the incorporation of the LOD EPR setup with the existing DNP setup to perform DNP and EPR using the same setup.

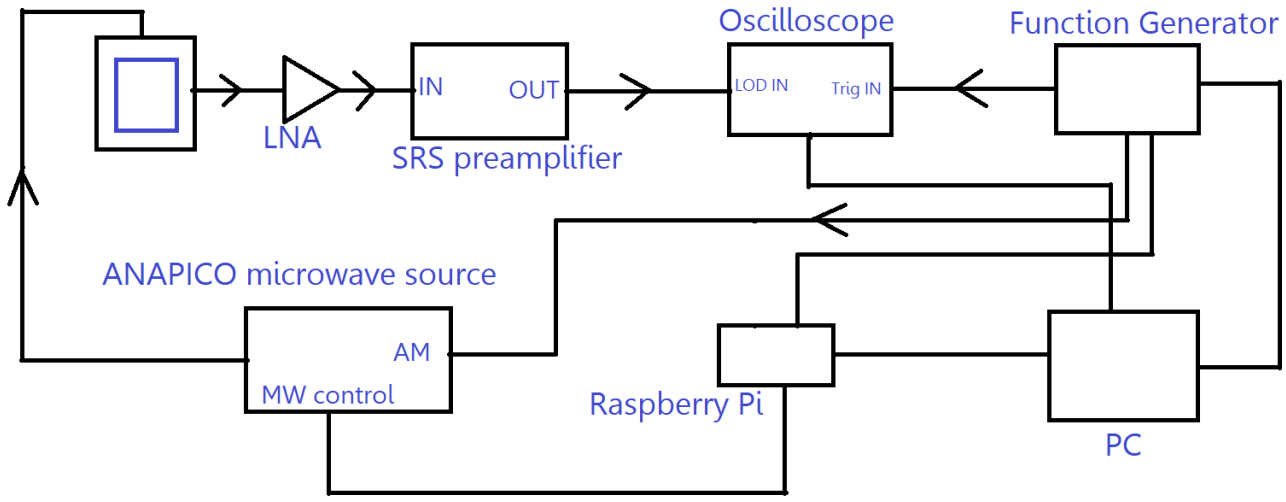

Fig. 22: LOD EPR setup with the differential amplifier, SRS amplifier, oscilloscope, function generator, and Raspberry Pi.

The LOD EPR signal and the trigger signal are shown in Fig. 23.

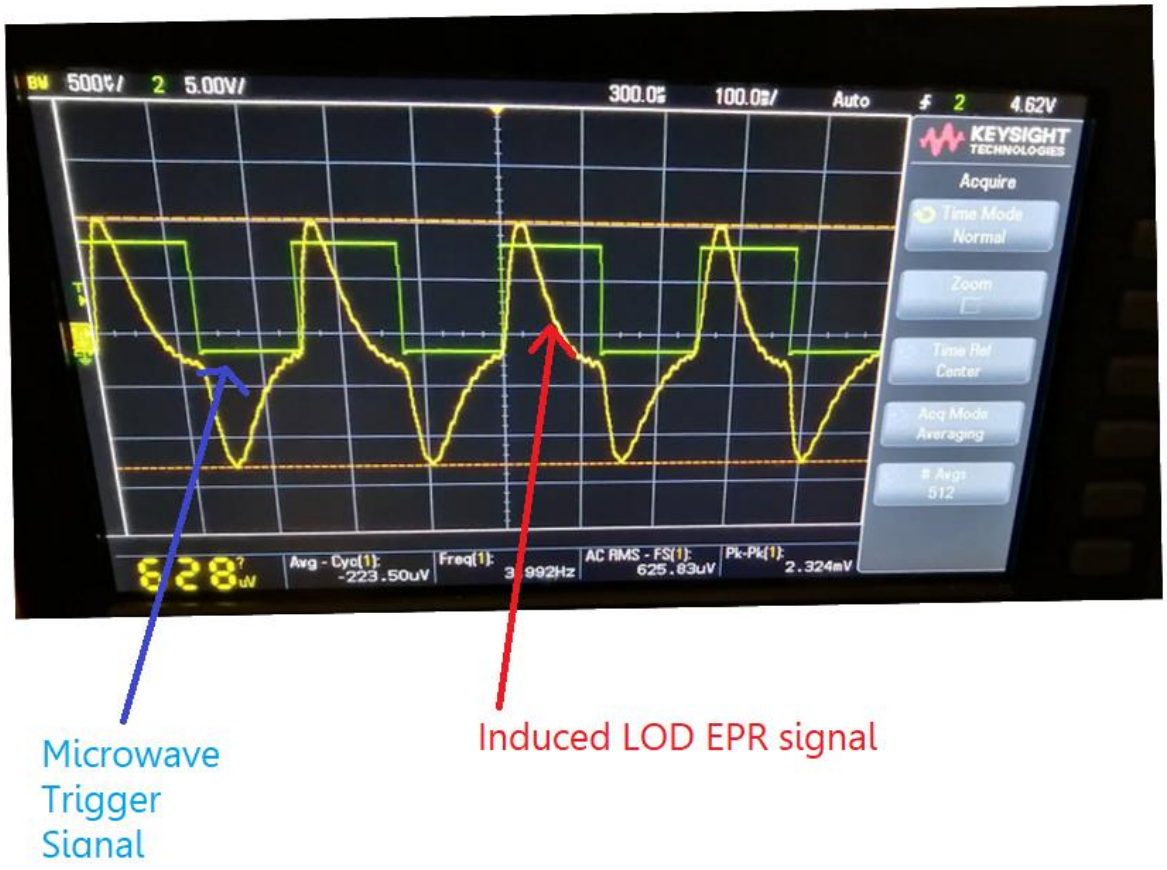

Fig. 23: The acquired LOD EPR signal for a particular microwave frequency and the microwave trigger/AM signal generated by the function generator using the SRS amplifier.

The difference between Fig. 21 and Fig. 23 is that in Fig. 23, the saturation and recovery curve of the LOD EPR signal are better because the SRS amplifier has a faster response than a normal amplifier and a low-pass filter.

3.4.2 **6.7T/188GHz polarizer:**

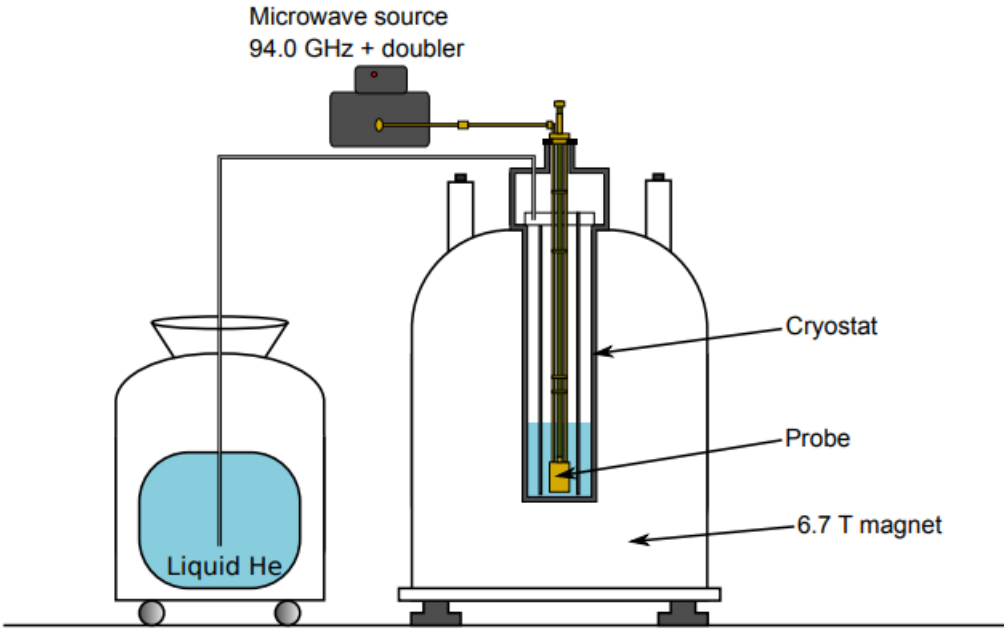

Fig. 24: The 6.7 T polarizer with the cryostat, probe, microwave bridge, and helium detector.

3.4.3 **The Dissolution DNP probe:**

In this apparatus, the microwaves are provided by either an ELVA1 source directly at 188 GHz or an AnaPico source coupled to a multiplier chain (X 12). Microwave frequency modulation is usually implemented to saturate a large fraction of the EPR spectrum [12]. In addition to radio-frequency (RF) capabilities, a d-DNP probe transfers microwaves from the source through a wave guide to the sample. An overview of a typical d-DNP probe is shown in Fig. 25.

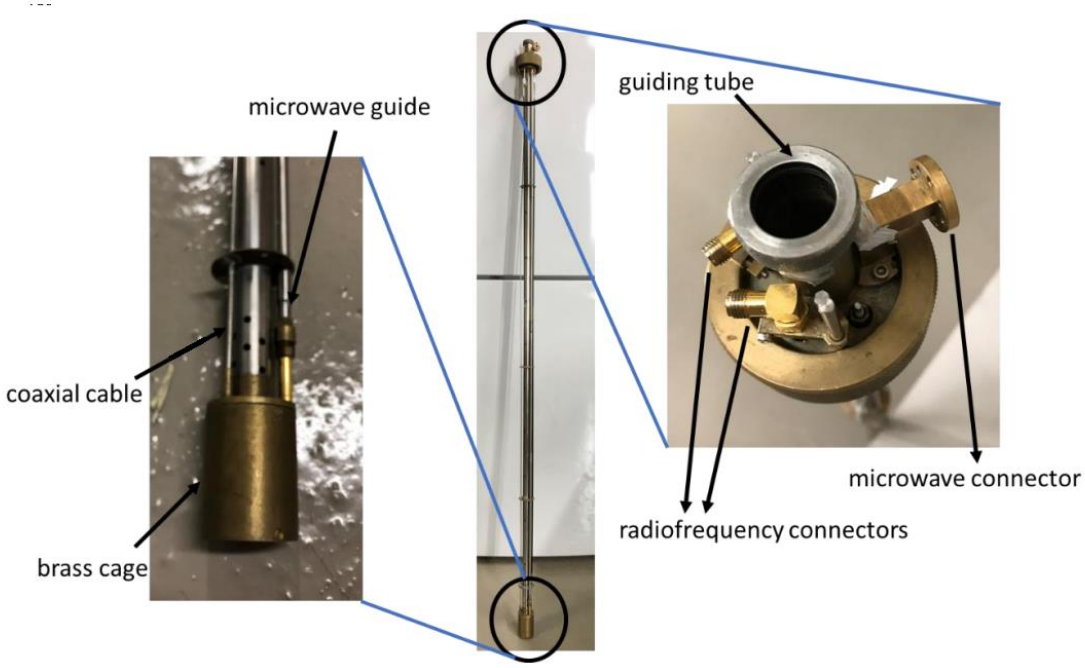

Fig. 25: - A view of a d-DNP probe (middle). The top part is magnified (right), which shows the guiding tube for insertion of the sample stick and RF and microwave connectors. A closer view of the bottom part is also shown (left), where the microwave guide, a coaxial cable, and a brass cage to protect the resonator are revealed.

This probe is placed inside the cryostat of the polarizer. Semi-rigid 50 Ω coaxial cables are used for the RF circuit. In addition to protecting the resonator, the brass cage confines the microwave field inside for maximum effect. Fig. 26 demonstrates a closer look inside the RF components of the probe. The coaxial cables go from the top to the bottom of the probe and are connected to the induction coils at the bottom. These induction coils are coupled to the saddle coils mounted on a glass cylinder (Fig. 26 (a)). When inserting a sample via the sample stick, the sample is placed inside this glass cylinder, and the microwave mirror is right in front of it. The sample is exposed both to microwaves and RF pulses at this position. Fig. 26 (a) shows the saddle coils mounted on the cylinder. Depending on whether the probe is a single resonance or a double resonance probe, there will be two or four saddle coils placed there. There are either just two coils in front of each other or another two are added perpendicular to the previous ones. Because each pair is perpendicular to the other, they are not coupled together. Each pair has its own induction coil and is tuned at a chosen nuclear frequency with the help of a few small, fixed capacitors, as seen in Fig. 26 (a). This type of circuit is tuned as close as possible to the desired nuclear frequencies, but small variations occur due to changes in the temperature and susceptibility of the different samples. Consequently, a tune and match box is designed for each nucleus to carry out the fine adjustment. This box (Fig. 26 (b)) is placed outside of the cryostat between the preamplifier and the RF connector on top of the probe.

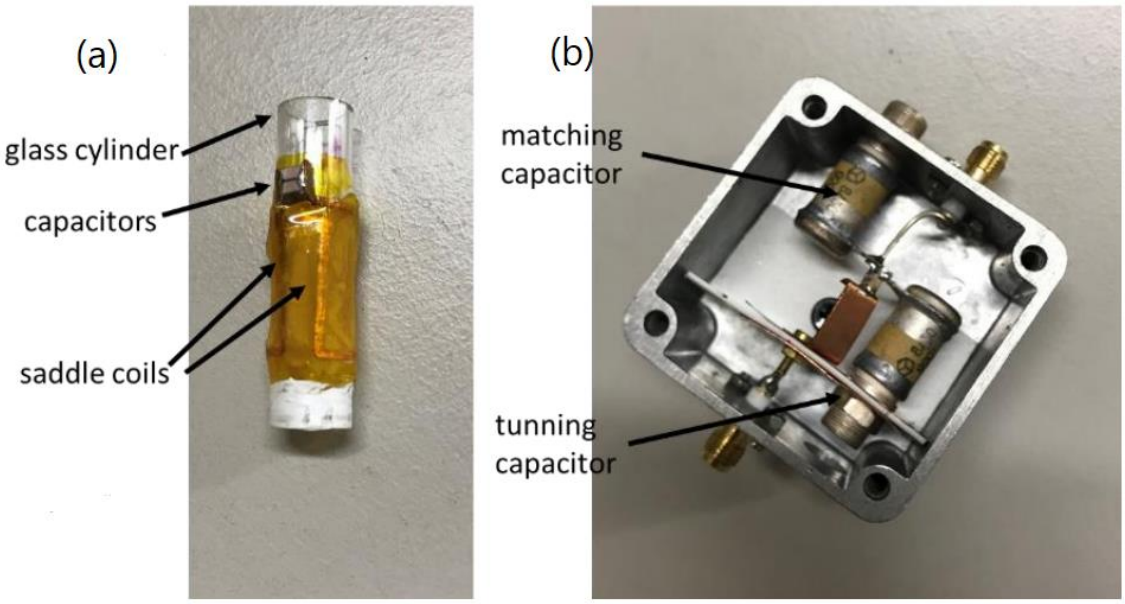

Fig. 26: Different parts of the RF circuit of the d-DNP probe. (a) A magnified look at the resonator's setup. (b) Tune and match the box for fine adjustments outside the polarizer.

3.4.4 **Dual DNP/EPR detection probe:**

In this setup, we will discuss the dual DNP/EPR setup. The LOD EPR coil in Fig. 27 (a) is inserted into the preexisting dissolution DNP probe, as shown in Figs. 27 (b) and (c).

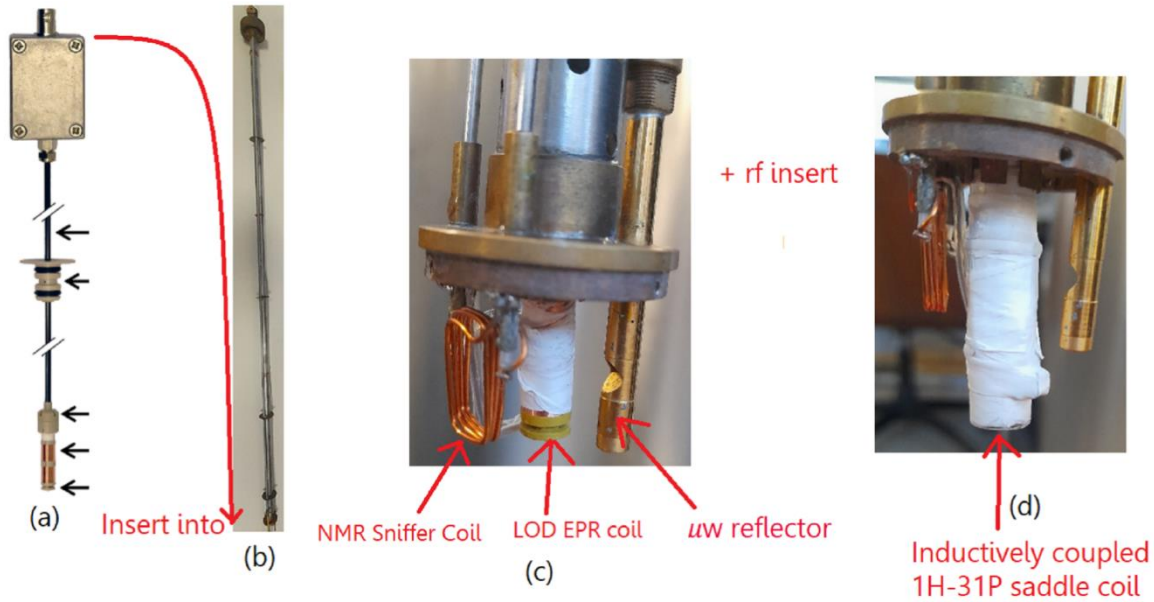

Fig. 27: The probe is composed of the following components: (a) the LOD EPR detection coil; (b) the dissolution DNP probe; (c) an enlarged picture of the bottom of the probe depicting the microwave reflector, NMR sniffer coil, and LOD coil; and (d) the ^{1}H-^{31}P RF insert.

The dissolution DNP probe is equipped with the waveguide needed to connect to the microwave source. And near the sample, there is a microwave reflector to irradiate the sample. The EPR coil is inside the RF insert, and the sniffer coil is facing the respective coil of the RF insert. The proper orientation of the RF insert is extremely crucial for NMR experiments. The tuning and matching box is used to tune and match as close as possible to the desired nuclear frequencies, but small variations occur due to changes in temperature.

3.4.5 **Microwave source Bridge:**

The microwave source used for most of our experiments is the AnaPico synthesizer, along with many other components. A detailed picture of the AnaPico microwave source at 188 GHz is shown in Fig. 28. Even though there are other components like the power supply for the multipliers, the synthesizer, and the control unit of the synthesizer. In this section, we will mainly talk about the important parts.

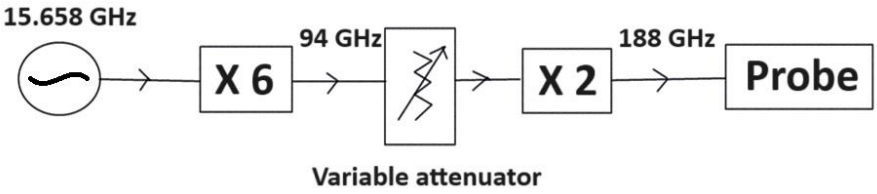

Fig. 28: Different components of the microwave source. Mainly the synthesizer and the multipliers.

The first component of the block diagram is the microwave synthesizer. The synthesizer used here is a solid-state device. In solid-state devices, usually Gunn diodes are used. The maximum power output of the synthesizer is 100 mW. A Raspberry Pi oversees the control of the source. The second component after the source is the X-6 multiplier. This multiplier is connected to a manual attenuator. The first multiplier multiplies the microwave that the source generates before it passes through the attenuator. The attenuation can be controlled using a manual knob. The attenuator is connected to a doubler (X-2), which multiplies the frequency to the 188 GHz range. The maximum output power after the doubler is 28 mW. The X-6 multiplier and the attenuator are shown in Fig. 29.

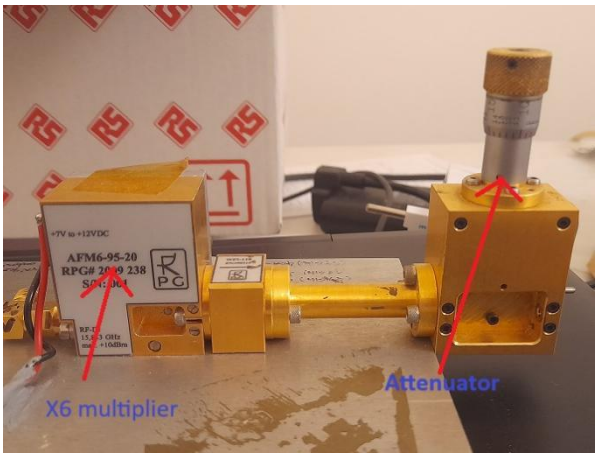

Fig. 29: The frequency multiplier and the attenuator of the AnaPico microwave source.

The other microwave source used for our experiments is the Elva source, rated at 188 GHz. It is also a solid-state device, and an Impatt diode is used as the source diode. The maximum output power is 150 mW. The input impedance of the microwave source modulation input is 10 kΩ. The modulation voltage must always be in the range [0V–10V] to avoid hardware damage at the FM port. The voltage is controlled using a Keysight 33511B function generator, as shown in Fig. 31. A schematic depicting the source and the probe is shown in Fig. 30.

Additionally, a custom-made hardware adapter with diodes is provided for use as hardware protection at the frequency modulation (FM) input to the ELVA-1 microwave source. The additional custom-made adapter is comprised of a Zener diode (unknown type, 5.1V), a Schottky diode (1N5822), and a resistor (to limit the Zener diode power). The circuit design and protection hardware diagram are shown in Fig. 32.

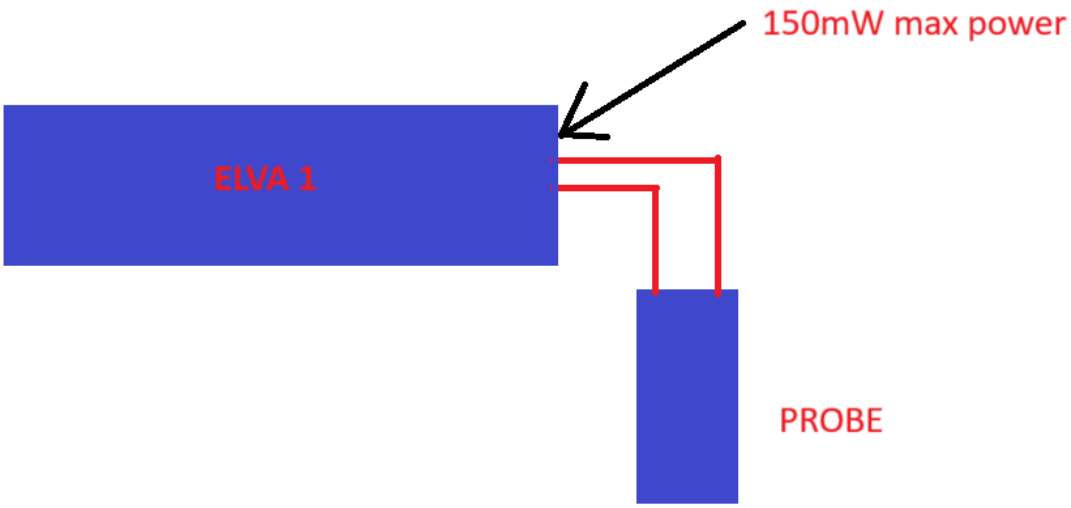

Fig. 30: A schematic of the connection between the Elva source and the probe.

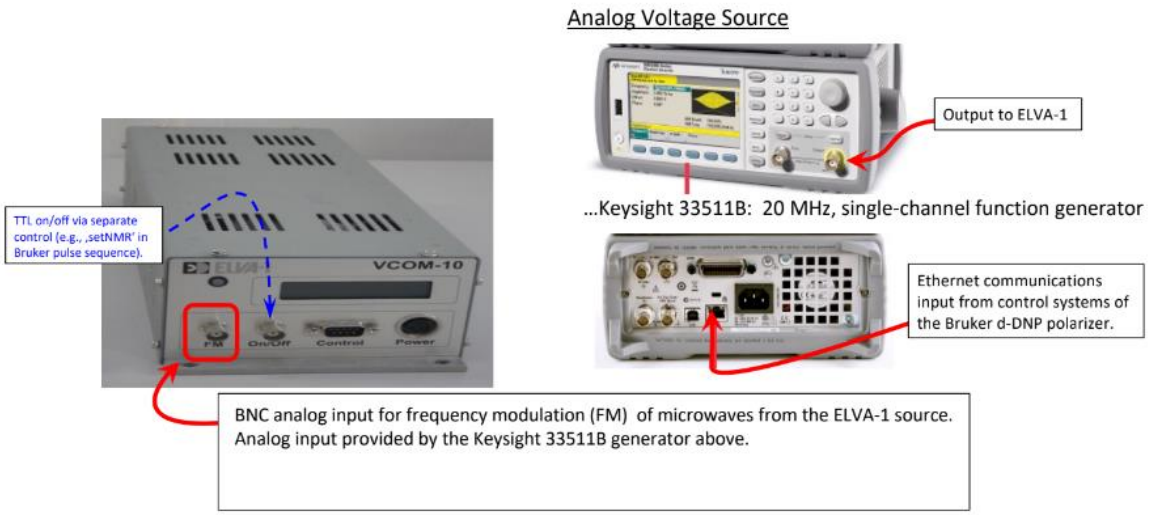

Fig. 31: The Elva microwave source and the Keysight function generator (analog voltage source).

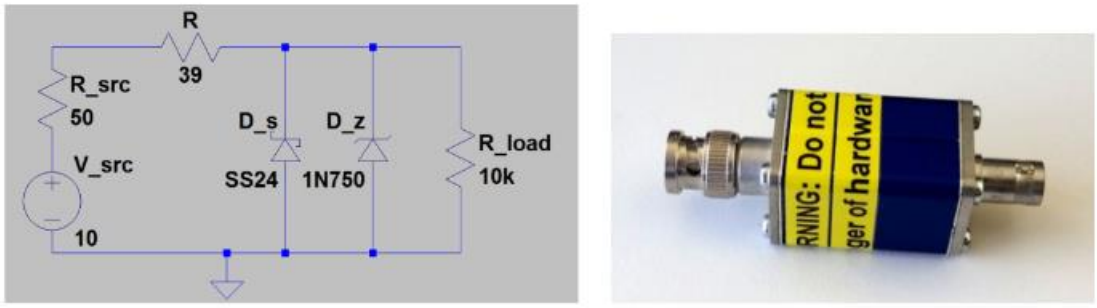

Fig. 32: The circuit diagram of the protection adaptor and the adaptor.

3.4.6 **Sample Preparation:**

For this experiment, TEMPO (4-hydroxy-2,2,6,6-tetramethylpiperidin-1-oxyl) was used as a polarizing agent. Tempol was dissolved at a 50 mM concentration in a mixture of glycerol-d8/D_2O/H_2O (V: V: V=50:40:10). A total volume of 400 µL was prepared for the experiment.

3.4.7 **Result:**

The preliminary experiments were conducted using TEMPOL radicals in DNP juice. Fig. 33 shows the DNP and EPR profiles of the sample at 4.2 K. AnaPico is used as the microwave source, with a maximum power of 28 mW in the 188 GHz range. For the LOD EPR experiment, the microwave is modulated by a square wave generated from the NI DAQ card. The acquisition is also performed using NI DAQ, where a lock-in detection technique is used. The EPR intensity is at the zero-crossing position of the DNP profile. The microwave amplitude modulation frequency is 5 Hz. In the DNP profile, the positive and negative DNP peaks can be seen, and the EPR peak matches the zero-crossing position of the DNP profile. The three hyperfine couplings with ^{14}N can also be seen. The positive and negative DNP peaks are almost proton Larmor frequencies away from the EPR peak.

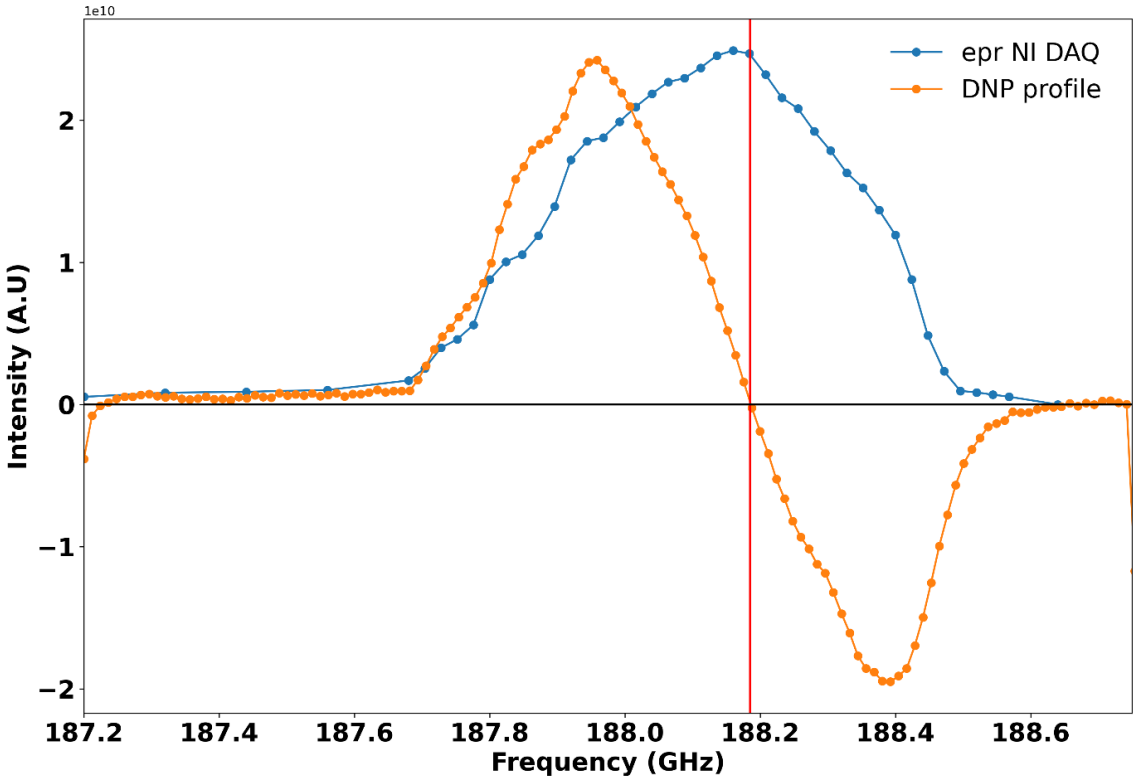

Fig. 33: It shows the DNP profile (orange) and the LOD EPR profile (blue) using NI DAQ, and the red line shows the EPR peak, which matches the zero-crossing position of the DNP profile.

The LOD EPR signal intensity is dependent on the microwave power. So, a power dependence curve for the microwave source is shown in Fig. 34. In the curve, the X-axis denotes the number of manual turns on the microwave attenuator. Here '0' means no attenuation, and the points after that correspond to the number of turns, and the Y-axis is the LOD EPR peak intensity.

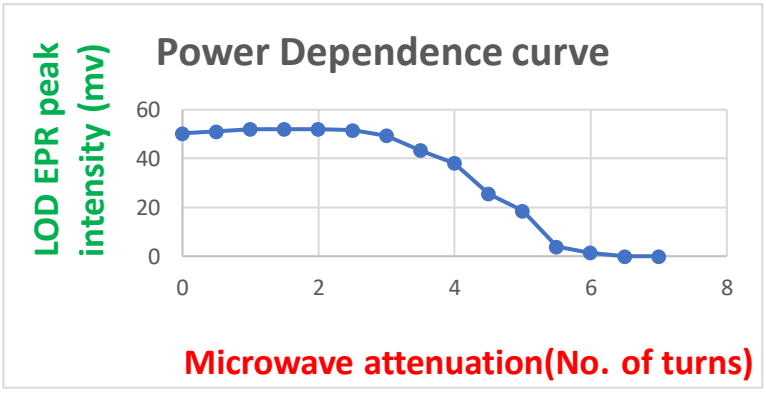

Fig. 34: Power dependence curve of the microwave power with the LOD EPR peak intensity.

4. LOD EPR for different radical:

Even though the preliminary experiments with the TEMPOL radical were successful and we got the EPR profile repeatedly, we needed to test the setup for other radicals. The next radical we used was the BDPA sample. It was dissolved at a

concentration of 40 mM in hexaflurobenzene and toluene (V: V = 50:50). Fig. 35 shows the EPR spectra of the BDPA radical at 4.2 K. The line width of the spectra is ~ 44.6 MHz.

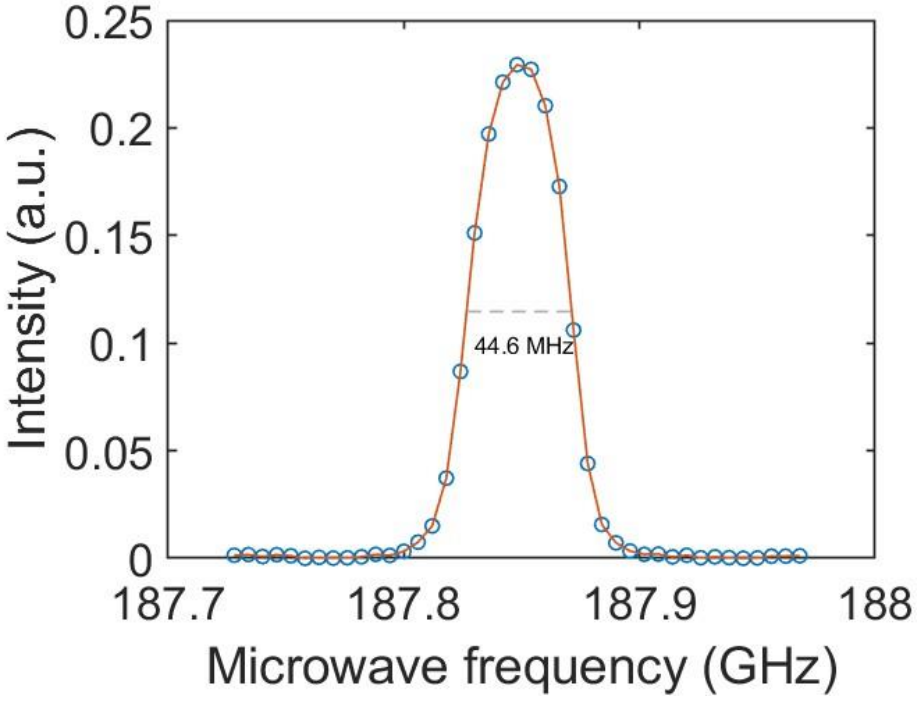

Fig. 35: LOD EPR spectra of the BDPA spectra with a width of 44.6 MHz.

For some time, we used an Elva source at 188 GHz for some of our experiments. The radical we used for these experiments is the trityl radical. It was dissolved in a 50 mM concentration in DNP juice. The LOD EPR spectra for different microwave powers are shown in Fig. 36.

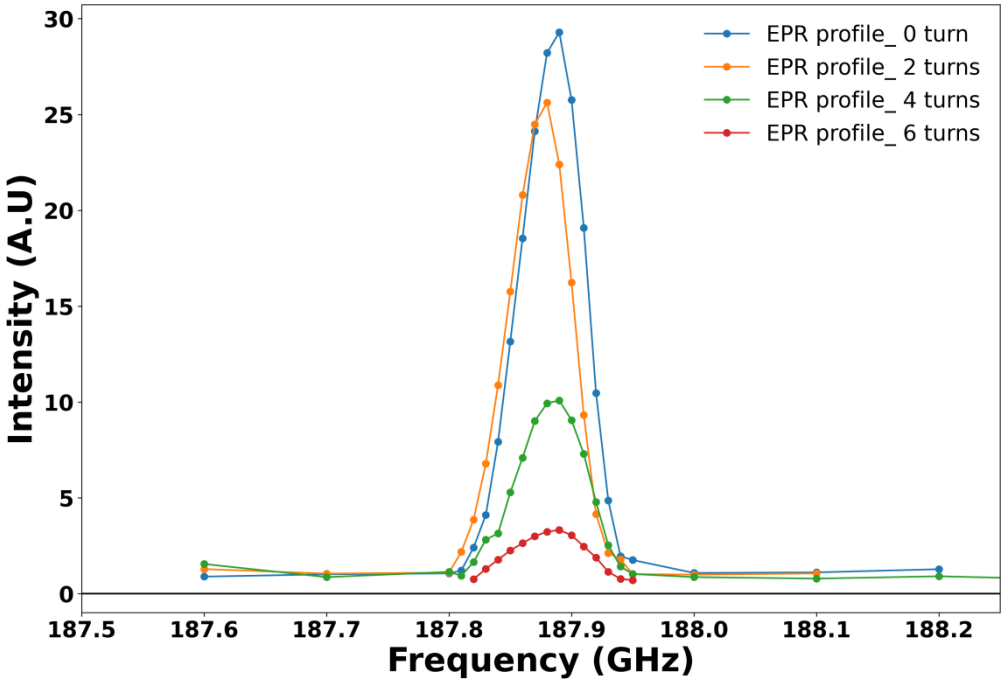

Fig. 36: LOD EPR spectra of the Trityl radical for different microwave powers.

In Fig. 36, we also showed here the power dependence curve of EPR intensity for the trityl radical. In our microwave bridge, we had a manual microwave attenuator. In the curve, 0 turns mean no attenuation; that means full power. Then the next curve has two turns, and we can see that the EPR intensity decreases. Then we put another two turns in, and the peak intensity dropped a lot. With an additional 2 turns, we can see that the EPR intensity decreased again. And if we put another two turns in, then we lose the EPR signal. This is always good to show the power dependence curve for EPR.

5 LOD EPR using optical chopper:

Till now, all the LOD EPR experiments have been performed using solid-state devices. To perform DNP at higher fields, a gyrotron needs to be used. The gyrotron cannot be gated using a trigger signal. And to perform EPR at a higher field, like 18.8 T, it is very hard to develop the microwave components required at that field. To develop a cost-effective system for both DNP and EPR measurement at higher fields and higher power LOD EPR techniques, proper modifications are required. In normal LOD EPR, the microwave is modulated using a trigger signal from a function generator or DAQ card. But it is not possible to perform this with the gyrotron. The solution that we came up with to solve this problem is to use an optical chopper to modulate the microwave. A schematic of the setup is shown in Fig. 37.

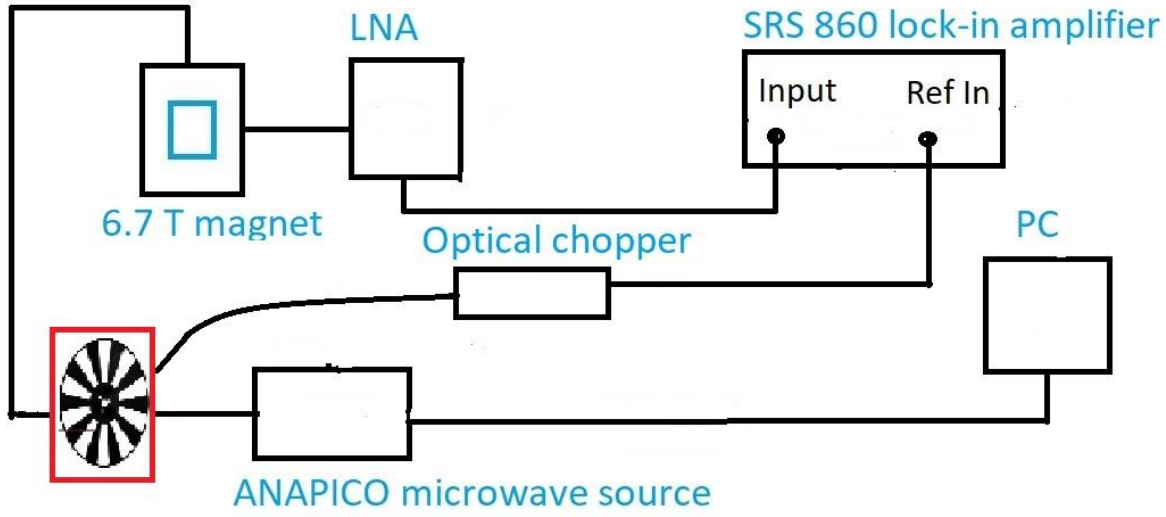

Fig. 37: Schematic diagram for the optically chopped EPR setup for the 6.7 T/188 GHz system.

In Fig. 36, the diagram depicts the setup for the 188 GHz system. This system was developed as a proof-of-principle experiment. Here, the microwave source used is the same as the AnaPico solid-state source used for the normal LOD EPR experiment.

5.1 Different components of the setup:

A detailed description of the different components of the setup is given below.

5.1.1 Optical Chopper:

The most common form of optical chopper is a rotating disc chopper. Its central part is a chopper disc (also called a chopper blade), which is typically made of black-coated metal and has the shape of a circle with some pattern of holes or slits (slots). The wheel is driven by a small electric motor, as shown in Fig. 38.

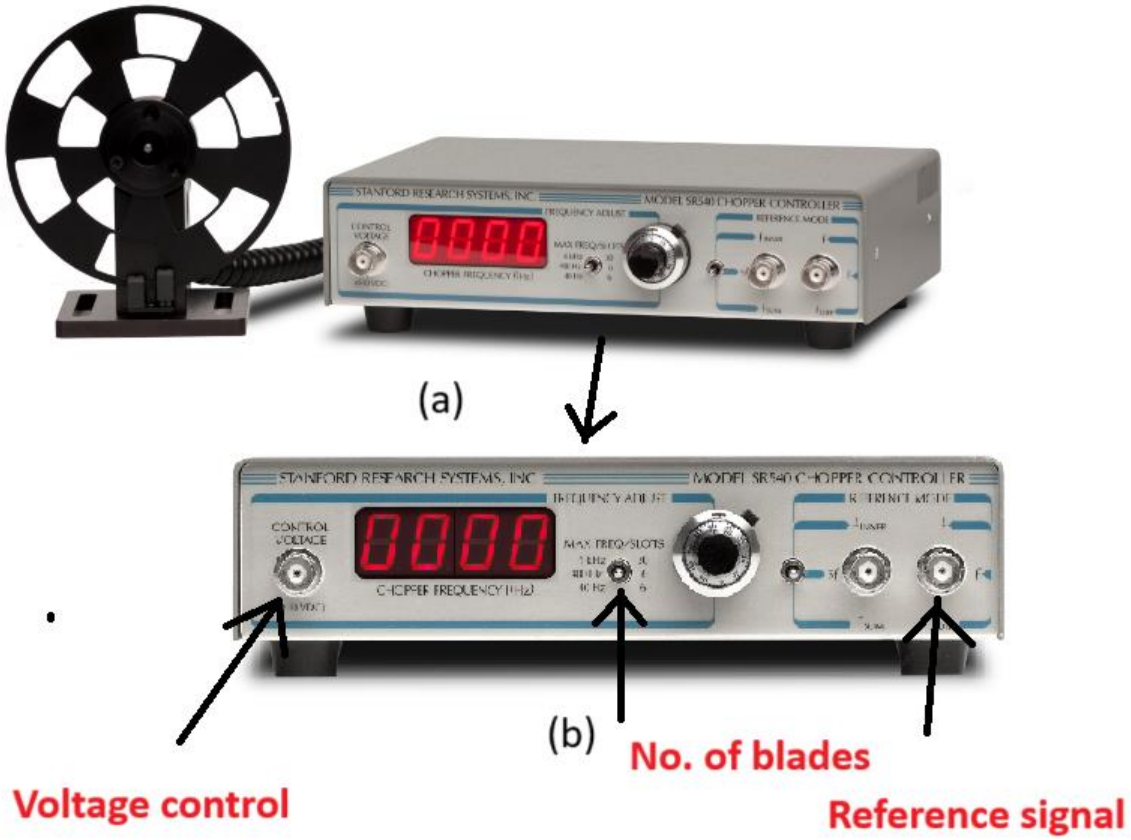

Fig. 38: (a) the complete SRS 540 optical chopper system with the chopper controller and the blades; and (b) the enlarged view of the controller showing the voltage control and reference signal output BNC port and the number of blade switches.

The rotation frequency of the chopper blade can be controlled using the voltage control input on the controller. One of the applications of the optical chopper is its use in lock-in detection. The optical chopper can be connected to the lock-in amplifier for controlling and detecting the signal. The number of blade slots can be fixed in the lock-in amplifier by inserting the required frequency on the screen of the amplifier to control the chopper.

The simplest mechanical working principle for the optical chopper is to block or pass a light beam or microwave. It is a commonly used technique in the domain of optical physics.

As shown in Fig. 39, there can be two (and rarely more) rows of slits, often with different numbers of holes, so that different chopping frequencies can be achieved with a given rotation frequency. Due to the integer frequency ratios, the term harmonic blades is sometimes used, or otherwise, dual frequency blades. Normally, the outer row has the highest number of slits.

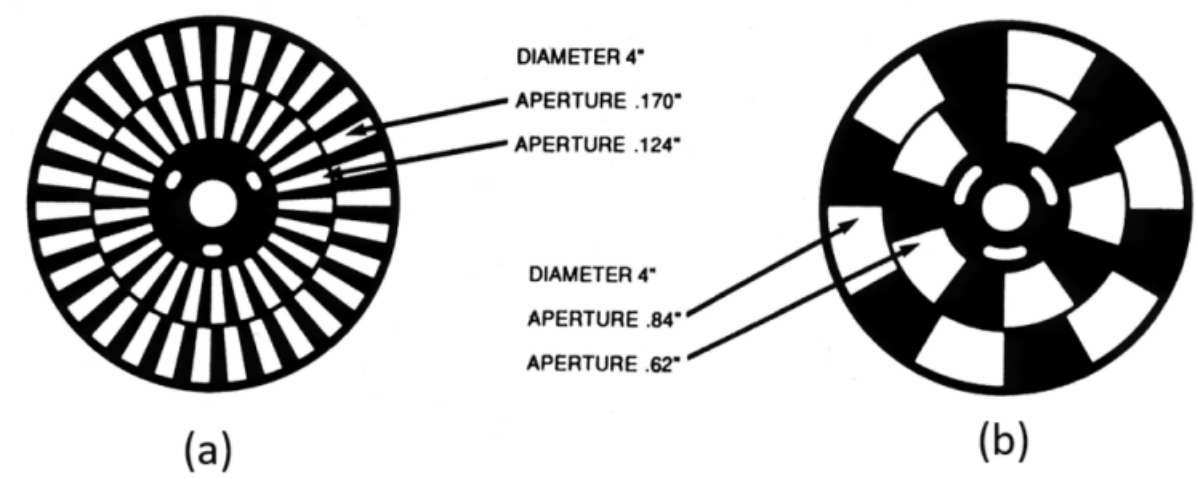

Fig. 39: (a) 30/25 slots and (b) 6/5 slots chopper blades

For LOD EPR detection, the optical chopper is placed at an angle of 45 degrees (Fig. 40) to reduce the reflection of the microwave back to the source. The reflection of microwaves can be extremely harmful for the microwave components. The 6/5 slot chopper blade is used for the experiment due to its ability to completely block and pass the microwave, allowing amplitude modulation of the microwave. Amplitude modulation is the change in magnetization, which induces a voltage in the pickup coil. This signal is first fed to the low-noise amplifier.

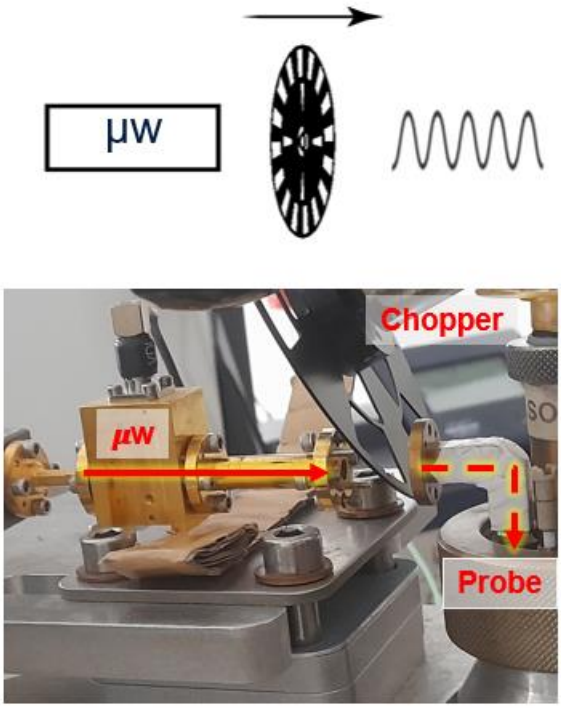

Fig. 40: The optical chopper is placed between the waveguide at an angle of 45 degrees. The flow of microwaves is depicted with a red arrow.

5.1.2 **Lock-in Amplifier:**

A lock-in amplifier is an instrument with dual capabilities. It can recover signals in the presence of an overwhelmingly noisy background or, alternatively, it can provide high-resolution measurements of relatively clean signals over several orders of magnitude and frequency. A lock-in amplifier provides a DC output proportional to the input AC signal. A rectifier called the phase-sensitive detector (PSD) is used for the AC-to-DC signal conversion. The PSD rectifies only the signal of interest while suppressing all the background noise associated with it.

The detector operates by multiplying two signals together. For example, when a noise-free sinusoidal signal is used as the input signal “Signal In" in Fig. 41, the instrument is fed with a reference signal from which it generates an input sinusoidal reference.

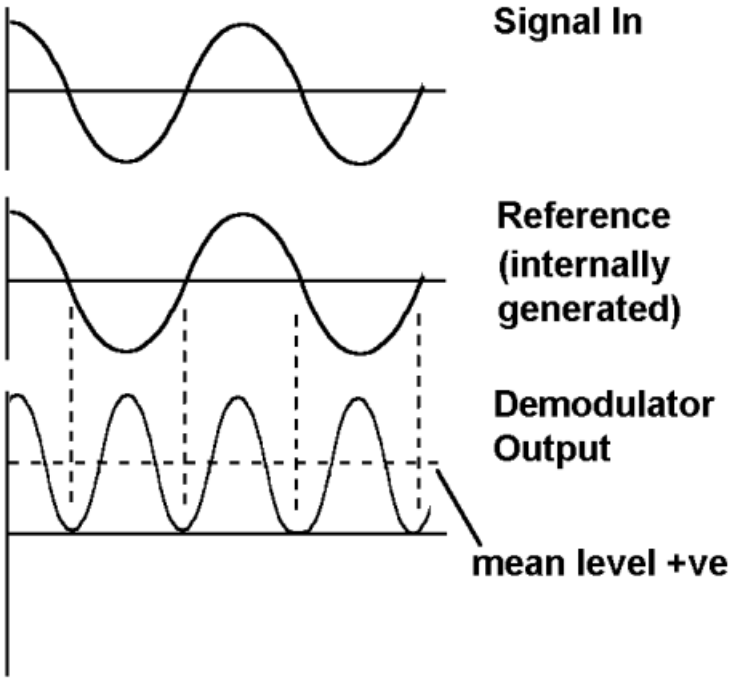

Fig. 41: Lock-in amplifier working principle depicting the input signal, reference signal, and demodulated output signal.

The demodulator operates by multiplying the two signals together to get the signal identified as the demodulated output. Since there is no relative phase difference between the input signal phase and the reference signal phasing, the demodulated output takes the form of a sinusoidal signal with twice the reference frequency but a positive mean level.

Fig. 42 depicts the situation where the input signal phase is 90 degrees behind the reference signal. In this case, although the demodulated output is still twice the reference signal, the mean level is zero.

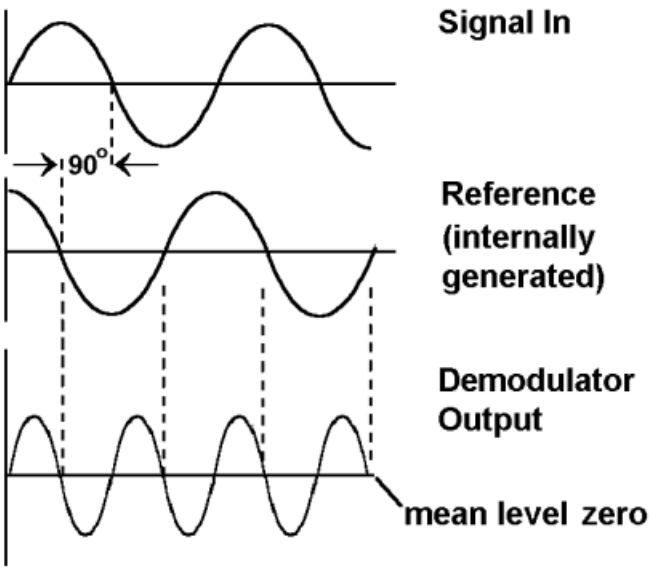

Fig. 42: Lock in the amplifier working principle when the input signal and the reference signal have different phases and the corresponding demodulated output signal.

The reference phase is adjusted to ensure a relative phase shift of zero degrees, and then by measuring the mean level, the amplitude of the input signal can be determined. The DC component of the signal is acquired by using a low-pass filter.

Even though the aforementioned discussion is based on a noise-free input signal, in our experiments, noise is present. This noise, which doesn't have any fixed frequency or phase relationship to the reference signal, is also multiplied by the reference signal in the demodulator, but it doesn't change anything about the mean DC level. Noise components with frequencies very close to the reference frequency do cause demodulated outputs at very low frequencies, but these can be thrown out by setting the low-pass filter to a low enough cut-off frequency.

A schematic diagram of the lock-in amplifier is shown in Fig. 43.

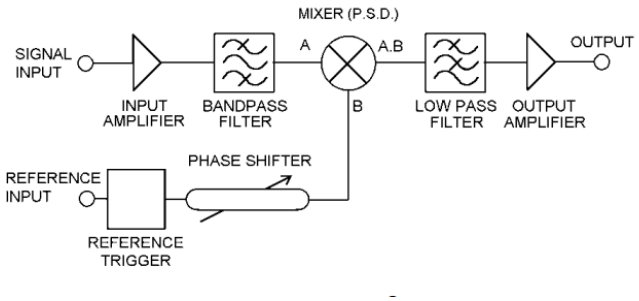

Fig. 43: A schematic diagram of the lock-in amplifier

For our experiments, the Stanford Research Systems SRS 860 model is used. The reference signal used for the optically chopped EPR comes from the controller of the optical chopper. To correctly configure the reference signal setting on the front panel of the SRS 860, the chop setting must be pressed on the "Source" section. As for the "External" section, a positive TTL is used. The input of the LOD signal after the low-

noise amplifier is connected to the single-ended (A) voltage unit of the lock-in amplifier. The sensitivity and the time constant are dependent on the LOD signal. The digital 24 dB/octave filter is used for the experiment. "Auto phase and range" is used to phase the input signal with the reference signal. The auto range" is needed when the signal is overshooting.

Fig. 44: The front panel of the SRS 860 lock-in amplifier

The settings on the SRS lock-in amplifier used for all the experiments are given in the following table.

Filter	Input range	Time Const.	Sensi-tivity	Ground	Couple	Source	External
24dB/octave	300mV	300ms	200mV	Float	AC	Chop	Positive TTL

Table 1: Experimental settings of the SRS lock-in amplifier.

5.2 Sample Preparation:

For this experiment, TEMPO (4-hydroxy-2,2,6,6-tetramethylpiperidin-1-oxyl) was used as a polarizing agent. Tempol was dissolved at a 50 mM concentration in a mixture of glycerol-d8/D_2O/H_2O (V: V: V=50:40:10). A total volume of 400 µL was prepared for the experiment.

5.3 Result:

The preliminary experiments were conducted using TEMPOL radicals in DNP juice. Fig. 45 shows the DNP and EPR profiles of the sample at 4.2 K. AnaPico is used as the microwave source, with a maximum power of 28 mW in the 188 GHz range. For the LOD EPR experiment, the microwave is modulated by an optical chopper placed at 45° to mitigate the microwave reflection. The EPR intensity is at the zero-crossing position of the DNP profile. The microwave amplitude modulation frequency is 5 Hz.

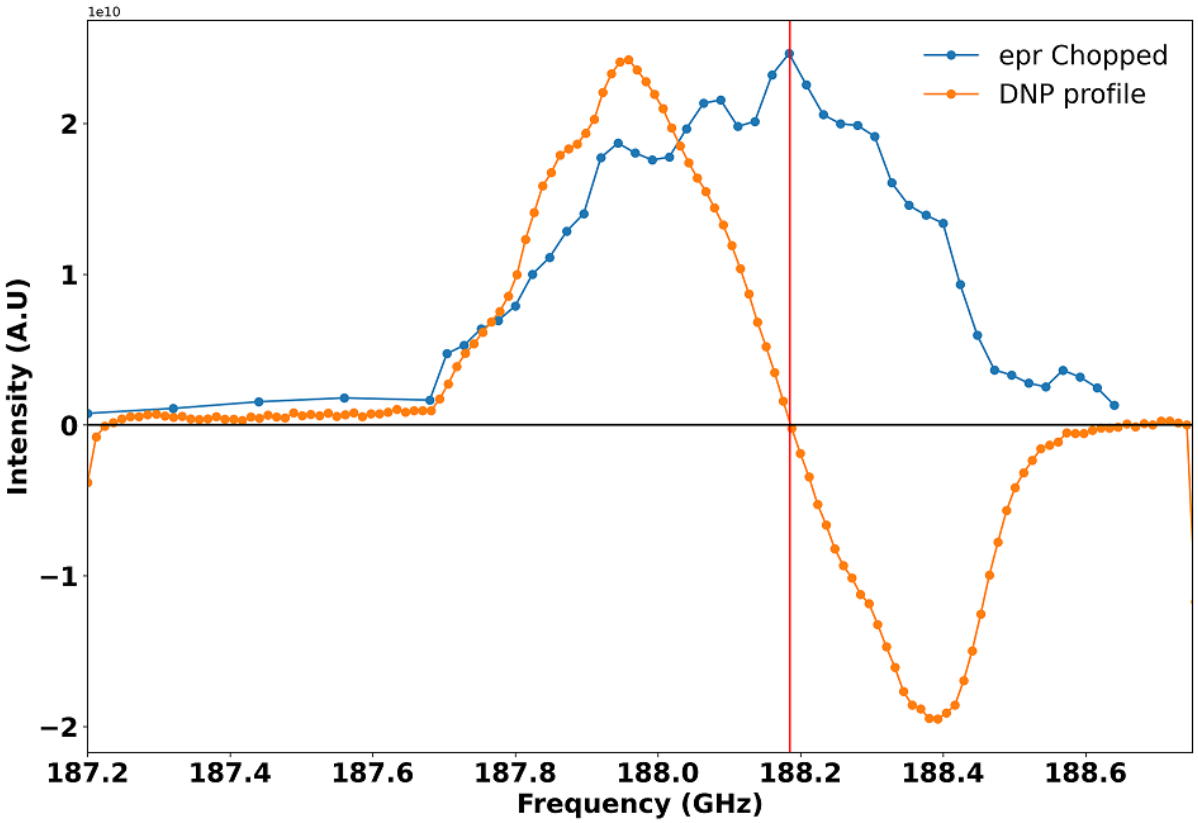

Fig. 45: It shows the DNP profile (orange) and the LOD EPR profile (blue) using an optical chopper, and the red line shows the EPR peak, which matches the zero-crossing position of the DNP profile.

In the DNP profile, the positive and negative DNP peaks can be seen, and the EPR peak matches the zero-crossing position of the DNP profile. The three hyperfine couplings with ^{14}N can also be seen. The positive and negative DNP peaks are almost proton Larmor frequencies away from the EPR peak.

6. Gyrotron based DNP:

Recently, a renewed and growing interest in dynamic nuclear polarization (DNP) enhanced nuclear magnetic resonance (NMR) spectroscopy has driven the development of high-frequency, low- and moderate-power, continuous wave (CW) gyrotrons. Although solid-state NMR is a widely used and powerful spectroscopic method, its inherent low sensitivity can limit its efficacy for some applications. DNP, which is one of several techniques used to enhance the sensitivity of high-frequency NMR, involves the transfer of the large polarization present in the electron spin reservoir of a sample, normally doped with a paramagnetic polarizing agent, to the nuclear spins via the irradiation of the sample with millimeter or terahertz waves. Generally, tens or hundreds of watts of power at the source are required for optimal DNP enhancement at NMR frequencies in the range of 400–900 MHz and beyond. Although solid-state and slow-wave devices are available and have been used for DNP at millimeter-wave frequencies, gyrotrons are generally more capable of producing moderate output powers at high frequencies than other device types and are, therefore, of particular interest as DNP sources.

In the past several decades, following the pioneering work at the Massachusetts Institute of Technology [18, 19], research efforts in the design, development, and implementation of gyrotrons in DNP/NMR systems have been carried out at several institutions around the world [20–25]. The success of these numerous research efforts in proving the significant NMR signal enhancement capabilities, often more than 100, ultimately led to the development of commercial gyrotron-based DNP systems [26–28]. A schematic diagram of a typical commercial gyrotron-based solid-state DNP/NMR system is shown in Fig. 46. The system consists of an NMR spectrometer, including a superconducting magnet, a low-temperature magic-angle-spinning DNP/NMR probe, and an NMR control system; a gyrotron and dedicated magnet, along with a power supply and control system; and a transmission line to connect the gyrotron source to the DNP/NMR probe.

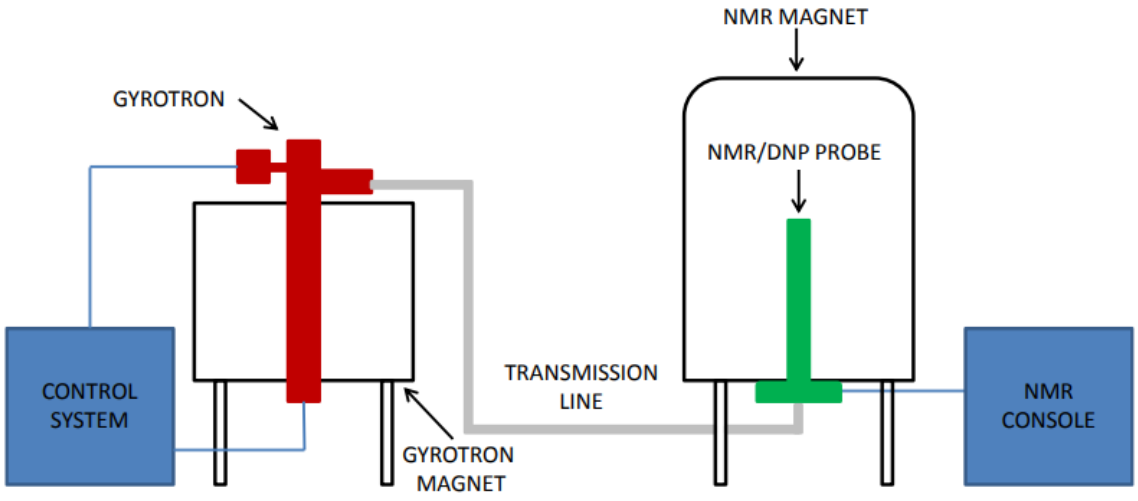

Fig. 46: Schematic diagram of a typical commercial solid-state DNP/NMR system.

6.1 Gyrotron microwave source:

A gyrotron is a specialized type of microwave oscillator that plays a crucial role in dynamic nuclear polarization (DNP), a technique used in nuclear magnetic resonance (NMR) spectroscopy and magnetic resonance imaging (MRI) to enhance the sensitivity of NMR signals. DNP is particularly useful for studying the structure and properties of complex molecules, biological systems, and materials.

The high-power MW radiation required by the low Q of the sample cavity is generated with a gyrotron oscillator. Prior to the use of a gyrotron, there was a dearth of high-power sources operating in the 100–600 GHz regime. This fact, more than any other, has impeded the development of DNP experiments for the magnetic fields used in contemporary high-resolution NMR experiments.

In summary, a gyrotron operates by exploiting the resonance between the cyclotron motion of electrons in a strong magnetic field and a high-frequency alternating electric field. This resonance results in the emission of coherent microwave radiation, making gyrotrons valuable as high-power microwave sources for a wide range of applications, including nuclear magnetic resonance (NMR) spectroscopy.

Gyrotrons are appropriate for use with high-field DNP because they are fast-wave millimeter devices, differing from slow-wave sources that rely on structures that scale with the microwave wavelength and become prohibitively fragile for the generation of high-power levels at higher frequencies required for DNP. Gyrotrons employ a resonator that can be overmoded with dimensions larger than the operation wavelength, allowing for high power output for extended periods due to reduced thermal and ohmic losses in the resonator walls. Gyrotrons capable of generating watts of CW power at 140 GHz [14], 250 GHz [15], and 460 GHz [16] have been built for integration into DNP spectrometers. The availability of these sources enables

DNP experiments to be performed in situ at high fields and avoids the necessity of shuttling.

6.2 Corrugated waveguide for transmission:

Transmitting the microwaves from the gyrotron to the sample in the probe with minimal loss and monitoring the microwave power output is another challenge that has been addressed by Woskov et al. [17]. Fundamental mode waveguides have unacceptable insertion losses and do not couple to a free-space Gaussian beam that is used for quasi-optical manipulation of the beam demanded by the physical geometric restrictions of the experiment. A corrugated overmoded waveguide with a cross-sectional diameter greater than the wavelength supports the efficient HE11 mode. The HE11 mode has a very low insertion loss and couples efficiently to a free-space Gaussian beam.

6.3 3.2mm LT MAS Probe:

DNP experiments are performed at low temperatures (100 K) for efficient transfer of polarization from electron spins to nuclear spins. The spinning frequency at 100 K is limited to 15 kHz with a 3.2 mm rotor. Nitrogen gas is used to spin the rotor using the three lines, which are bearing, drive, and VT. Inside the probe is also a corrugated waveguide for shining the microwave into the sample. There is a horn waveguide at the bottom of the probe, which is used as a bridge between the gyrotron waveguide and the probe waveguide.

6.4 Modification to the LT MAS probe for static DNP application using optical chopper:

To enable the LT MAS probe for LOD EPR detection, some changes were made to the probe. The 3.2-mm stator was taken out of the probe, and in place, a 3D-printed box was placed with a saddle coil inside. The saddle coil is for NMR detection. The 3D-printed box is shown in Fig. 47.

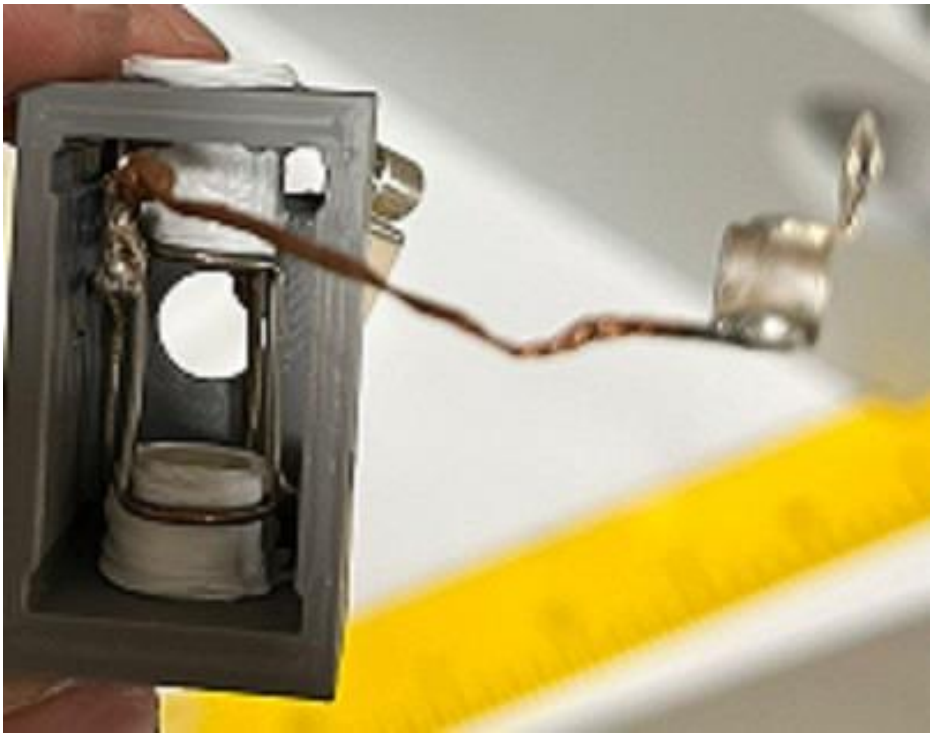

Fig. 47: The 3D-printed box with the saddle coil.

The nitrogen gas flows directly from the sides of the probe to the sample. The NMR signal is detected using the saddle coil inside the 3D-printed box.

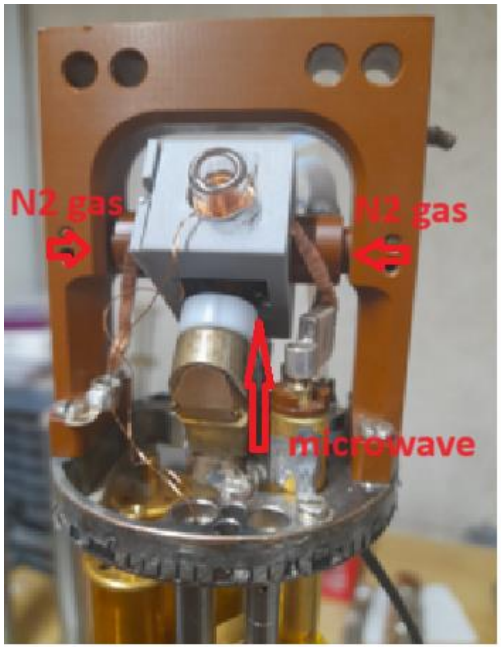

Fig. 48: The 3D-printed box was mounted on the probe with all the gas connections connected. The gap for the microwave can also be seen in the picture.

6.5 Gyrotron Interlock:

In the BRUKER gyrotron, there is a safety mechanism in which the gyrotron can only be switched on when the probe is cold (~ 100K). The probe has a sensor that

detects the temperature and sends the information to the gyrotron console through the gyrotron interlock, as shown in Fig. 49. In normal room temperature, the gyrotron control screen shows "RT," or room temperature, as shown in Fig. 50.

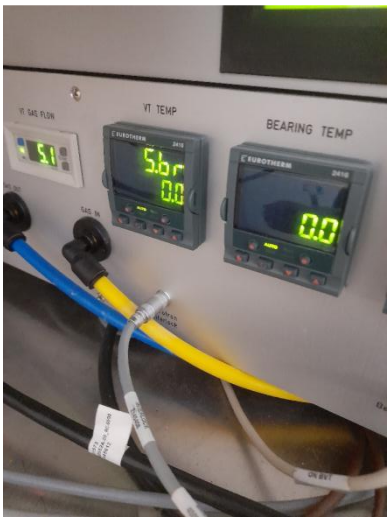

Fig. 49: The gyrotron interlock is connected to the DNP condition in normal conditions.

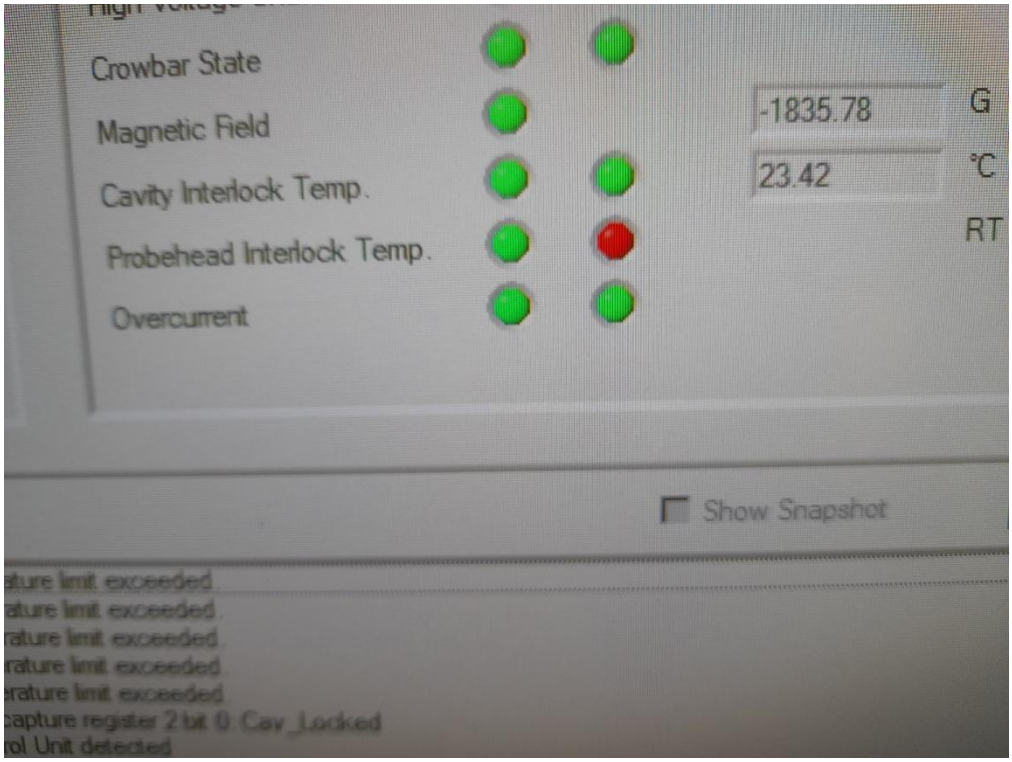

Fig. 50: The corresponding gyrotron screen where the probe head interlock temperature is shown is 'RT'.

To test or perform experiments at too high a temperature, a gyrotron interlock is made. A resistance (470 Ω) corresponding to the 100K temperature is connected to the twinax connector, as shown in Fig. 51. The sensors in the LT MAS probes usually have a sensor that changes the resistance depending on the temperature.

So, we found out the resistance for low temperature and connected it to the twinax connector, which in turn is connected to the gyrotron console (Fig. 51), and this resistor fakes the gyrotron to think that the probe is at low temperature. When the console detects the low temperature, the probe head interlock temperature changes from RT to LT, as shown in Fig. 53. After this, the mouth of the waveguide also needs to be covered by Kapton tape to switch on the gyrotron.

Fig. 51: The gyrotron is interlocked with the resistor connected to it.

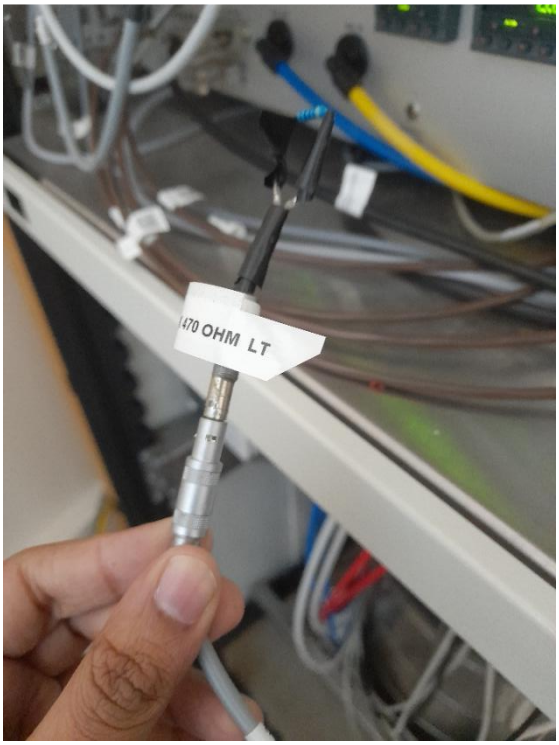

Fig. 52: The gyrotron interlock is connected to the cable for the console.

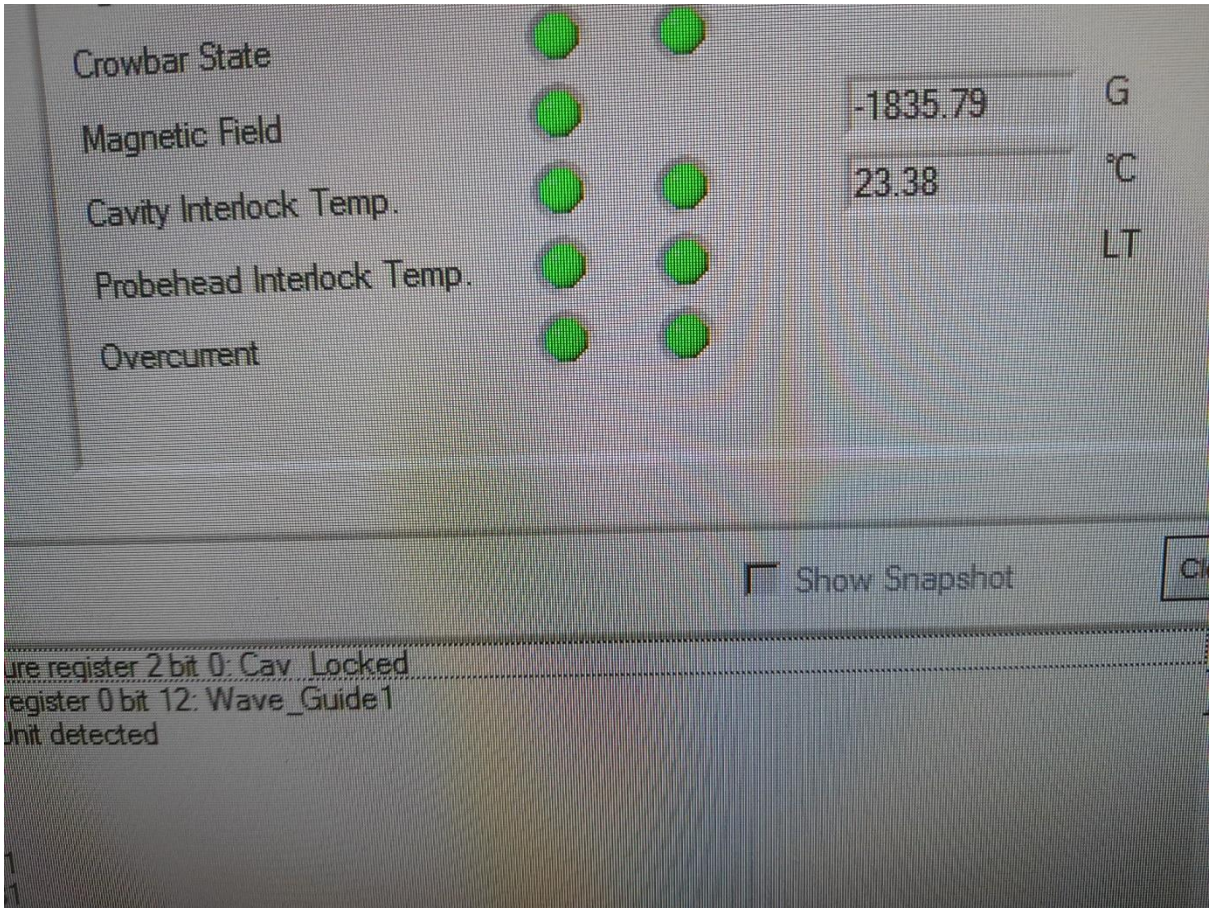

Fig. 53: The corresponding gyrotron screen shows the probe head interlock temperature as 'LT'.

6.6 Gyrotron based DNP with optical chopper:

To perform the DNP experiment with the optical chopper, a gap is made between the gyrotron waveguide and the horn waveguide of the probe. The mouth of the gyrotron wave guide is covered with Kapton tape. The gap between the waveguides is enough to purge the optical chopper at 45°, as shown in Fig. 54. The optical chopper is set at 45° to reduce microwave reflection. The rotation frequency of the chopper is 100 Hz.

6.7 Sample preparation:

For this experiment, BDPA is used as a polarizing agent. BDPA was dissolved at a concentration of 40 mM in a mixture of hexafluorobenzene and toluene (V: V= 50:50). A total volume of 400 µL was prepared for the experiment.

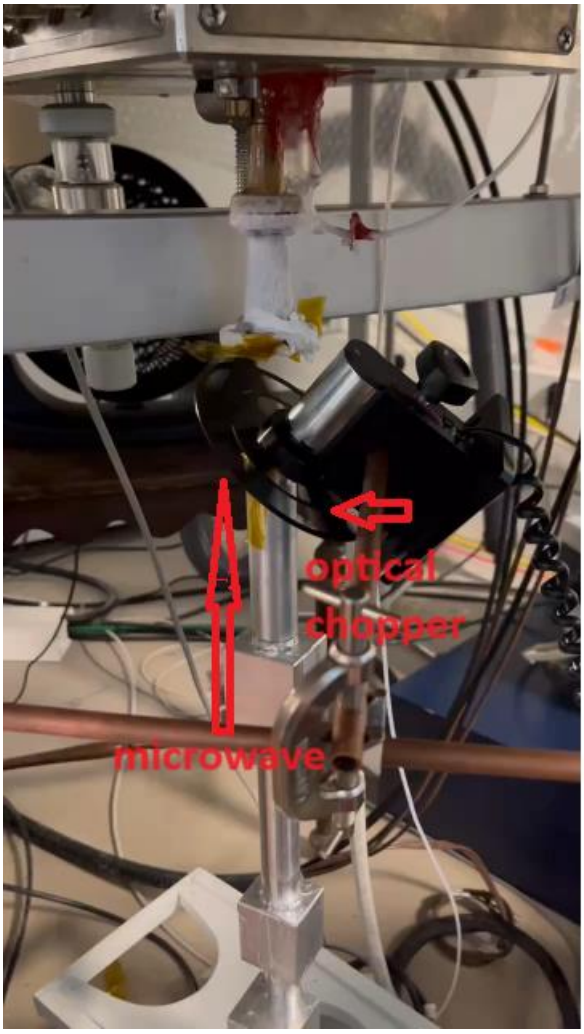

Fig. 54: Optical chopper setup with the gyrotron for the 800 MHz system

6.8 Result:

The preliminary experiments were conducted using the BDPA radical in hexafluorobenzene and toluene. Fig. 55 shows the DNP profile of the sample at 90K with and without an optical chopper. The gyrotron is used as the microwave source, with a maximum power of 10 W in the 527 GHz range. For the DNP experiment, the microwave is modulated by an optical chopper placed at 45° to mitigate the microwave reflection. The decrease in intensity proves that an optical chopper can be incorporated with a gyrotron to perform LOD EPR experiments at 527 GHz. The chopper is used at 100 Hz. So, the microwave is modulated at a frequency of 100 Hz.

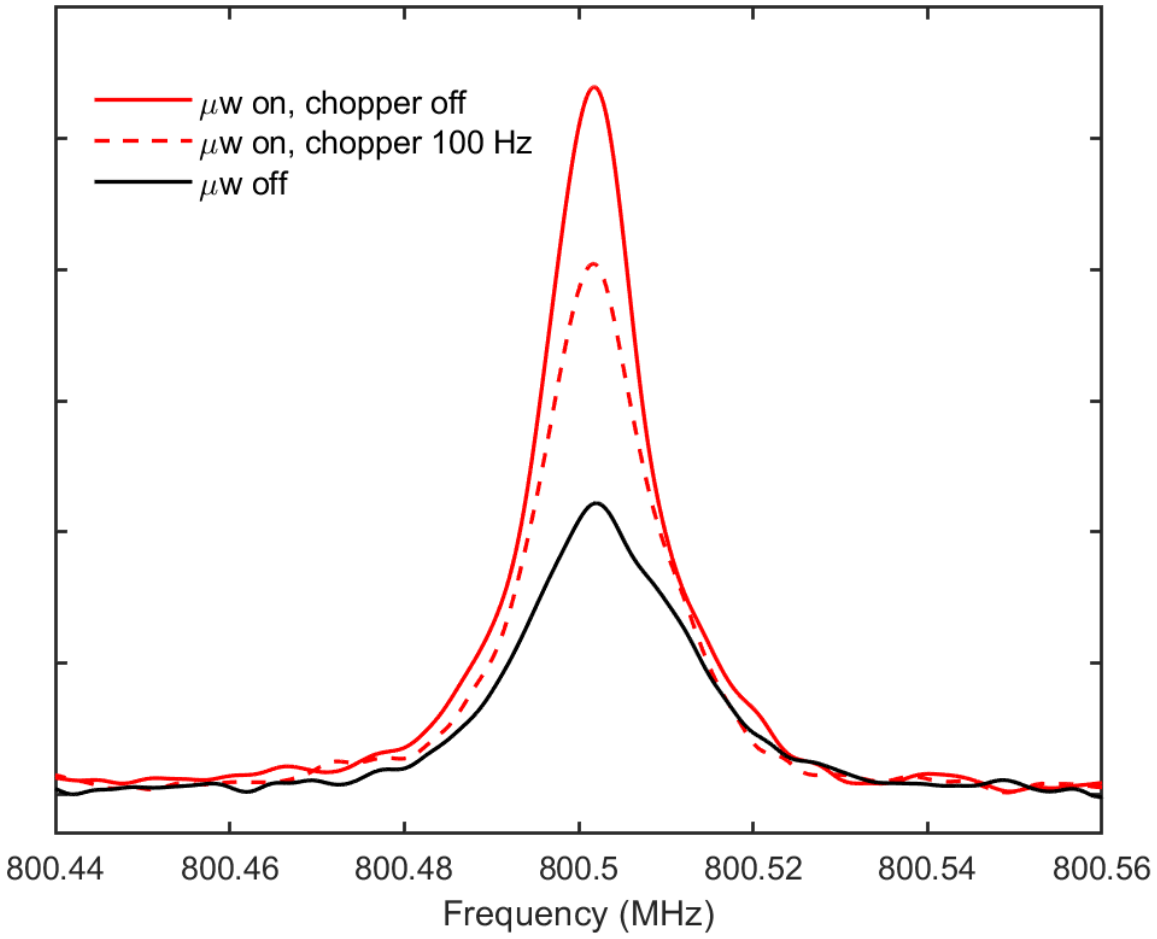

Fig. 55: DNP profile of BDPA radicals without microwave (black) With a microwave (red) and with an optical chopper (red dashed).

References:

[1] F. Bloch, W.W. Hansen, M. Packard, Phys. Rev. 70 (1946) 474.

[2] J. Frenkel, J. Phys. U.S.S.R., 9, 299 (1945).

[3] R. L. Cummerow, D. Halliday, Phys. Rev., 70, 433 (1946).

[4] D. M. S. Bagguley, J. H. E. Griffiths, Nature (London, U.K.), 160, 532 (1947).

[5] H. Dehmelt, Am. J. Phys., 58, 17 (1990)

[6] W.R. Hagen, Chapter 4 - EPR spectroscopy, in: R.R. Crichton, R.O. Louro (Eds.), Practical Approaches to Biological Inorganic Chemistry (Second Edition), Eds, Elsevier, 2020, pp. 121–154, https://doi.org/10.1016/B978-0-444-64225- 7.00004-3.

[7] M.M. Roessler, E. Salvadori, Principles and applications of EPR spectroscopy in the chemical sciences, Chemical Society Reviews 47 (8) (2018) 2534–2553.

[8] G.I. Likhtenshtein, J. Yamauchi, S. Nakatsuji, A.I. Smirnov, R. Tamura, Nitroxides: Brief History, Fundamentals, and Recent Developments, Springer, 2020

[9] Granwehr, Josef, Jörg Forrer, and Arthur Schweiger. "Longitudinally detected EPR: improved instrumentation and new pulse schemes." *Journal of Magnetic Resonance* 151, no. 1 (2001): 78-84.

[10] Granwehr, Josef, James Leggett, and Walter Köckenberger. "A low-cost implementation of EPR detection in a dissolution DNP setup." *Journal of Magnetic Resonance* 187, no. 2 (2007): 266-276.

[11] I. Nicholson, F. Robb, D. Lurie, Imaging paramagnetic species using radiofrequency longitudinally detected ESR (LODESR imaging), J. Magn. Reson. B 104 (1994) 284–288.

[12] A. Bornet, J. Milani, B. Vuichoud, A.J. Perez Linde, G. Bodenhausen, S. Jannin, Microwave frequency modulation to enhance Dissolution Dynamic Nuclear Polarization, Chemical Physics Letters, 602 (2014) 63-67.

[13] Lê, Thanh Phong, Jean-Noël Hyacinthe, and Andrea Capozzi. "Multi-sample/multi-nucleus parallel polarization and monitoring enabled by a fluid path technology compatible cryogenic probe for dissolution dynamic nuclear polarization." *Scientific Reports* 13, no. 1 (2023): 7962.

[14] Becerra LR, Gerfen GJ, Temkin RJ, Singel DJ, Griffin RG. Phys. Rev. Lett 1993; 71:3561–3564. [PubMed: 10055008].

[15] Kreischer, KE.; Farrar, C.; Griffin, RG.; Temkin, RJ.; Vieregg, J. Proceedings of 24th International Conference on Infrared and Millimeter Waves. Lombardo, L., editor. Monterey, Calif.: UC Davis; 1999.

[16] Hornstein MK, Bajaj VS, Griffin RG, Temkin RJ. IEEE Trans. Plasma Sci 2006; 34:524–533.

[17] Woskov PW, Bajaj VS, Hornstein MK, Temkin RJ, Griffin RG. IEEE Trans. Microwave Theory Tech 2005; 53:1863–1869.

[18] L.R. Becerra, G.J. Gerfen, R.J. Temkin, et al. “Dynamic nuclear polarization with a cyclotron resonance maser at 5 T”. Phys. Rev. Lett., 71, 3561-3564 (1993).

[19] L.R. Becerra, G.J. Gerfen, B.F. Bellew, et al. “A spectrometer for dynamic nuclear polarization and electron paramagnetic resonance at high frequencies”. J. Magn. Reson. A, 117, 28-40 (1995).

[20] M.K. Hornstein, V.S. Bajaj, R.G. Griffin, et al. “Continuous-wave operation of a 460 GHz second harmonic gyrotron oscillator”. IEEE Trans Plasma Sci, 34, 524-533 (2006).

[21] Y. Matsuki, H. Takahashi, K. Ueda, et al. “Dynamic nuclear polarization experiments at 14.1T for solid-state NMR”. Phys. Chem. Chem. Phys., 12, 5799–5803 (2010).

[22] S. Alberti, J. Ph. Ansermet, F. Braunmuller, et al. “Experimental results on a modular gyrotron operating at 0.26 THz for 400 MHz DNP/NMR spectroscopy applications”. 38th Int. Conf. on Infrared, Millimeter. and Terhertz Waves (IRMMW-THz 2012), Woolongong, Australia, Sept 23-28, Thu-A-2-3 (2012).

[23] S. Jawla, Q.Z Ni, A. Barnes, et al., “Continuously tunable 250 GHz gyrotron with a double disk window for DNP-NMR spectroscopy”. J. Infrared Milli Terahz Waves, 34, 42-52 (2013)

[24] R. Ikeda, Y. Yamaguchi, Y. Tatematsu, et al. “Broadband continuously frequency tunable gyrotron for 600 MHz DNP-NMR spectroscopy”. Plasma Fusion Res., 9, 1206068 (2014)

[25] T. Idehara, Y. Tatematsu, Y. Yamaguchi, et al. “The development of 460 GHz gyrotrons for 700 MHz DNP NMR spectroscopy”. J. Infrared Milli Terahz Waves, 36, 613-627 (2015).

[26] V. Denysenkov, M.J. Prandolini, M. Gafurov, et al. “Liquid-state DNP using a 260 GHz high power gyrotron”. Phys. Chem. Chem. Phys. 12, 5786-5790 (2010).

[27] M.Yu. Glyavin, A.V. Chirkov, G.G. Denisov, et al. “Experimental test of a 263 GHz gyrotron for spectroscopic applications and diagnostics of various media”. Rev. Sci. Instrum. 86, 054705 (2015).

[28] M. Rosay, L. Tometich, S. Pawsey, et al. “Solid-state dynamic nuclear polarization at 263 GHz: spectrometer design and experimental results”. Phys. Chem. Chem. Phys. 12, 5850-5860 (2010).

[29] S. Stoll, A. Schweiger, EasySpin, a comprehensive software package for spectral simulation and analysis in EPR, Journal of Magnetic Resonance 178 (1) (2006) 42–55, https://doi.org/10.1016/j.jmr.2005.08.013.

[30] N. Hirota, S. Yamauchi, Short-lived excited triplet states studied by time-resolved EPR spectroscopy, Journal of Photochemistry and Photobiology C: Photochemistry Reviews 4 (2) (2003) 109–124, https://doi.org/10.1016/S1389-5567(03)00024-8.

[31] R. Bittl, S. Weber, Transient radical pairs studied by time-resolved EPR, Biochimica et Biophysica Acta (BBA) - Bioenergetics 1707 (1) (2005) 117–126, https://doi.org/10.1016/j.bbabio.2004.03.012.

[32] M. A. Voinov, T. I. Smirnova, A. I. Smirnov, EPR Oximetry with Nitroxides: Effects of Molecular Structure, pH, and Electrolyte Concentration. Applied Magnetic Resonance 10.1007/s00723-021-01446-8(2021) 10.1007/s00723-021-01446-8.

[33] R. Ahmad, et al., Multisite EPR oximetry from multiple quadrature harmonics, Journal of Magnetic Resonance 214 (2012) 135–143, https://doi.org/10.1016/j.jmr.2011.10.016

[34] C. Altenbach, W. Froncisz, R. Hemker, H. McHaourab, W.L. Hubbell, Accessibility of Nitroxide Side Chains: Absolute Heisenberg Exchange Rates from Power Saturation EPR, Biophysical Journal 89 (3) (2005) 2103–2112, https://doi.org/10.1529/biophysj.105.059063.

[35] M. Swartz et al. (2014) Advances in Probes and Methods for Clinical EPR Oximetry. in Oxygen Transport to Tissue XXXVI, eds H. M. Swartz, D. K. Harrison,D. F. Bruley (Springer New York, New York, NY), pp 73-79.

[36] M. Swartz, T. Walczak, "Developing in Vivo EPR Oximetry for Clinical use" in Oxygen Transport to Tissue XX, A. G. Hudetz, D. F. Bruley, Eds. (Springer US, Boston, MA, 1998), 10.1007/978-1-4615-4863-8_29, pp. 243-252.

[37] L. Hubbell, C. Altenbach, Investigation of structure and dynamics in membrane proteins using site-directed spin labeling, Current Opinion in Structural Biology 4 (4) (1994) 566–573, https://doi.org/10.1016/S0959-440X(94)90219-4.

[38] L. Hubbell, A. Gross, R. Langen, M.A. Lietzow, Recent advances in site-directed spin labeling of proteins, Current Opinion in Structural Biology 8 (5) (1998) 649–656, https://doi.org/10.1016/S0959-440X(98)80158-9.

7. In-house Fabrication of MAS drive caps:

Solid-state NMR is a powerful characterization technique that has been widely applied to study solid-state samples ranging from small molecules, biological macromolecules, to inorganic materials [1]. Although solid-state samples usually have broad peaks due to anisotropic interactions such as dipolar couplings and chemical shift anisotropy, they can be averaged out by performing magic angle spinning (MAS) experiments [2,3], where the sample is spun at an angle of 54.74 with respect to the static magnetic field. It is essential that the MAS frequency (υ_r) should be sufficiently larger than the size of the anisotropic interactions to achieve an efficient line-narrowing effect, i.e., the rotors can spin up to υ_r = 160 kHz depending on their sizes [4,5].

MAS frequencies without significantly heating the NMR sample, the rotors are pneumatically spun with gas to reduce frictional heating. Besides achieving faster MAS frequencies, maintaining a stable spinning frequency (usually within a deviation of few Hz) is important over the course of experiments, especially for 2D or 3D NMR experiments that could last several days or week(s). Hence, the choices of material for both the rotor and MAS drive cap are important as they must be mechanically rigid (high tensile or flexural strength), and easily fabricated—especially the drive cap with an intricate spiral feature. Some of the materials that fulfill these criteria are ZrO_2, Macor, boron nitride, Kel-F, Vespel, and Torlon. Among these choices, ZrO_2 and Vespel are popular materials for the drive cap because ZrO_2 has superior mechanical strength and a low thermal expansion coefficient, which is preferred for low-temperature dynamic nuclear polarization (DNP) experiments [6–8]. However, machining ZrO_2 is challenging and, hence, expensive, i.e., a 3.2 mm ZrO_2 cap costs 1k USD (CortecNet). Although the Vespel drive cap is more affordable (~130 USD for 3.2 mm), it is still a non-negligible expense because the delicate fins on the drive cap wear out easily if they are mishandled or after repeatedly fitted/removed from the rotor. These effects are noticeably noted for smaller rotors, i.e., the 0.7 mm drive cap is usually for one-time use only, and it must be replaced with a new piece when packing new samples into the same rotor. To minimize the expenditure on these consumables (MAS drive caps), it has been recently demonstrated that the MAS drive caps can be fabricated using relatively low-cost 3D printing technology [9,10].

There are two main categories of 3D printing technology: fused deposition modelling (FDM) and stereolithography (SLA). Although the FDM method has, in general, a poorer resolution, it is more affordable and easier to use relative to the resin-based SLA method. Both 3D printing technologies have been exploited in various NMR applications, ranging from fabricating MAS sample eject systems [11], RF coils [12–15], NMR sample tubes [16], parahydrogen generator [17], NMR sample degassing apparatus [18,19], NMR probe heads [20], etc. Besides these examples, Xu et al. have recently demonstrated that it is possible to fabricate MAS stator and drive caps using FDM, but only for > 3.5 mm system [9]. High-resolution SLA technology has also been exploited for constructing MAS spinning system. Notable examples include the fabrication of > 4 mm spherical-rotor stators using a benchtop 3D printer by the Barnes' group [21,22], and a 3.2 mm cylindrical-rotor stator and drive caps

produced by dedicated manufacturing companies reported by Banks et al. [10]. Although outsourcing the manufacturing process can save labour resources, we note that the quality of the parts varies across different batches. This could be because the printing and/or post-processing steps performed by the company are not necessarily the same for each batch. Consequently, the lack of consistent results could lead to a more time- and cost-consuming process. Moreover, the same publication commented that the benchtop 3D printer (Form 3 with 25 μm XY resolution) was tested to be incapable of producing the 3.2 mm drive caps [10]. In this publication, we re-examine this statement by showing that not only the Form 3+ 3D printer can fabricate robust 3.2 mm drive caps, but also smaller 2.5- and 1.3-mm drive caps (with slightly compromised performances). In particular, the 3.2 mm 3D-printed drive caps (Fig. 56) can spin up to ν_r = 22 kHz ± 1.3 Hz, which has similar performances as the commercial versions, but only costs < 1 US cents and 5 min/piece to be 3D-printed (assuming a simultaneous printing of 100 pieces in a single print job). Additionally, the in-house fabricated 3D-printed drive caps exhibit excellent spinning stability that is sufficient for practical multi-dimensional MAS NMR experiments.

7.1. Experimental methods:

7.1.1 3D printing and post processing process:

The drive caps were designed in Autodesk Inventor (Autodesk Inc, San Rafael) following a similar design described in Banks et al. [10]. The drive caps were printed using standard Clear v4 resin in a Form 3+ (Formlabs) printer with a 25 μm XY resolution and layer thickness. The 3D printer costs ~ 4 k USD, and the resin costs ~ 140 USD/litre. The printing supports were placed on the bottom of the stem with a contact point size of 0.3 mm. It takes ~ 4 h to simultaneously 3D-print 100 pieces of drive caps in a single print job. Note that the build platform of the 3D printer can accommodate >100 pieces in a single print (if needed) without significantly increasing the printing hours. After the printing job finished, the parts were first rinsed in an isopropanol-water mixture (9:1 by volume ratio) to remove the uncured resin and irregularities on the surface. Then, the supports were removed and rinsed again before being cured under UV light (Elegoo Mercury) for 1 h (2x30 min, with another rinsing step between the two curing sessions) to enhance the mechanical properties. Note that the caps should be completely dry after every rinsing step. It is known that the SLA-printed parts gradually shrink in size over time, and the long curing time (1 hr) is a crucial step to accelerate the shrinking process and, hence, more stable in the long term. To account for the change in dimension after the post-processing steps, we have iteratively compensated for the changes by redesigning and reprinting the parts. In addition to the Form 3+ 3D printer, we have also tested another benchtop 3D printer (Elegoo Saturn), which has a lower XY resolution (50 μm). We have used the Elegoo 3D printer to print 4 mm caps (with Elegoo standard grey resin), and they show similar performances as the commercial (Bruker) version.

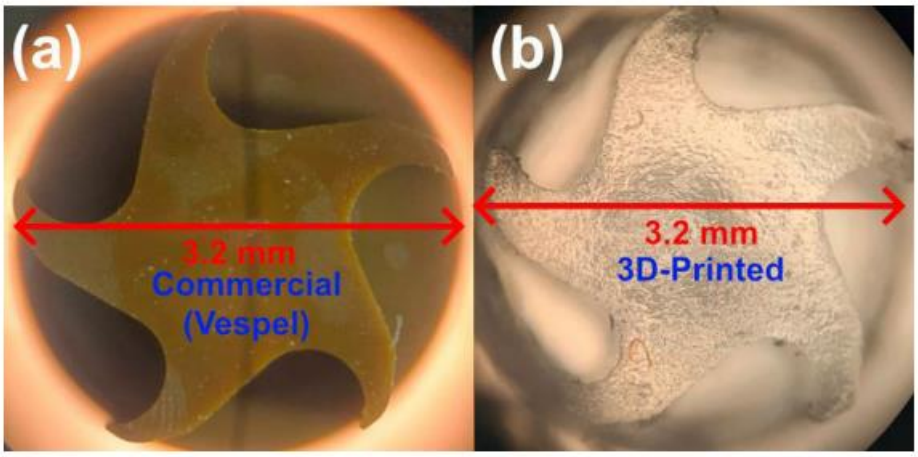

Fig. 56: Image of (a) a commercial (Bruker) Vespel and (b) a 3D-printed 3.2 mm MAS drive cap

7.1.2 Artefact compensation by iterative design modification:

The dimensions of the 3D-printed pieces could be slightly different from the computer-aided design (CAD) due to the properties of the resins, printing environment (temperature), post-processing steps, printing orientations, etc. Nevertheless, some of these undesired changes could be compensated by minor modifications (often iterative) in the CAD. An example of this is the 'overhang' feature that occurs when the resin tends to bulge downward due to gravity (Fig. 57a). The artefact has resulted in a small gap between the drive cap and the rotor and, hence, compromised the spinning performances, i.e., it does not spin up beyond 22 kHz. Although this feature can be partially compensated by reversing the printing orientation, it, unfortunately, affects the form of the fins (Fig. 57b). Thus, we introduced a concave curvature to the horizontal slab (Fig. 57c). Consequently, the printed part (Fig. 57d) did result in a better fit and a higher spinning frequency to ~ 26 kHz.

Besides that, we have also made the fins on the 1.3 mm drive cap sharper (Fig. 58d and e) to compensate for the broader-than-expected fins (Fig. 58a and b) due to the finite size of the laser beam used in the Form 3+ 3D printer (85 µm). The corrected drive caps (Fig. 58e) were able to achieve the same spinning frequency with less drive gas (vide infra, Fig. 61a), and the maximum ν_r was improved from 37 to 45 kHz. Additionally, we would like to highlight that the diameters of the stem (the component that fits into the rotor) and the slab (Fig. 57c) of the drive caps require very tight tolerances, i.e., they must be fabricated within a ~ 10 µm accuracy for optimal performances.

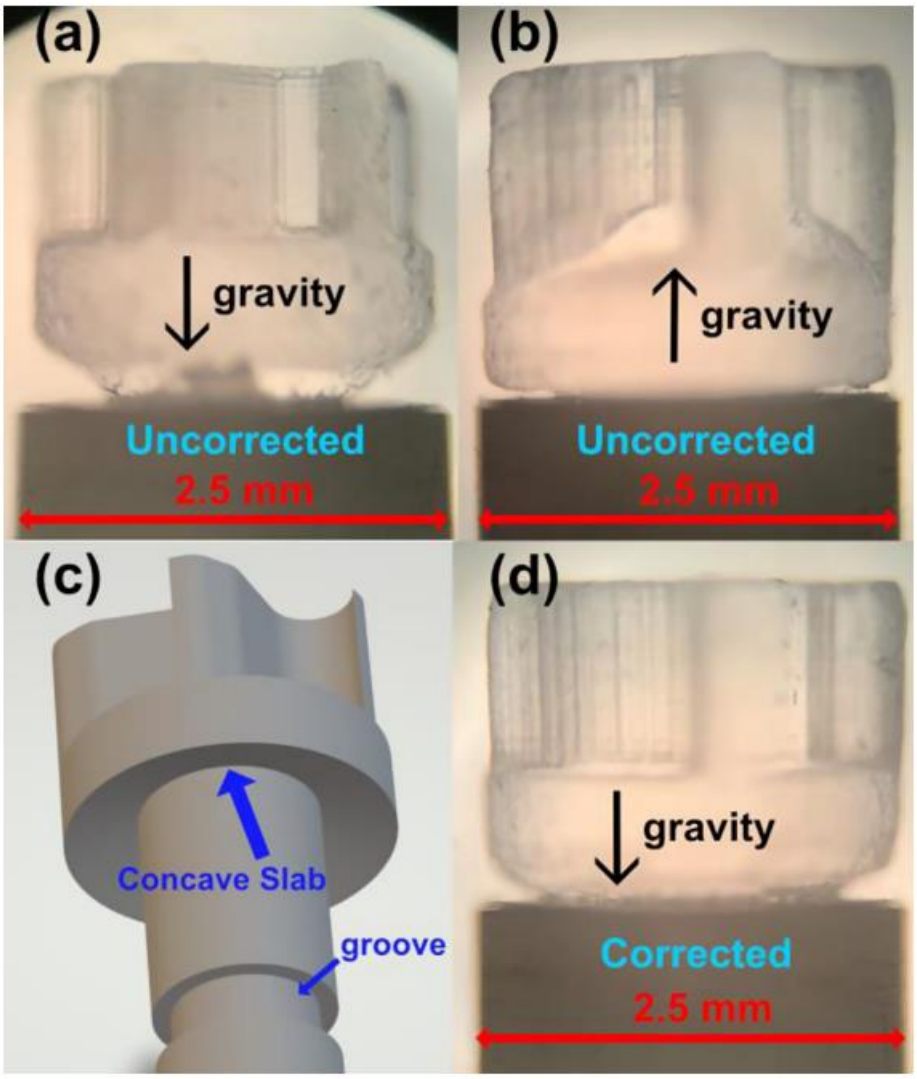

Fig. 57: Images of 2.5 mm MAS drive caps. Note the undesirable overhang effect present in the (a) upright and (b) reversed orientation. The artefacts were compensated by designing (c) a concaved (curved inward) slab, which yields the (d) corrected cap that improves the maximum spinning frequency from 22 to 26 kHz.

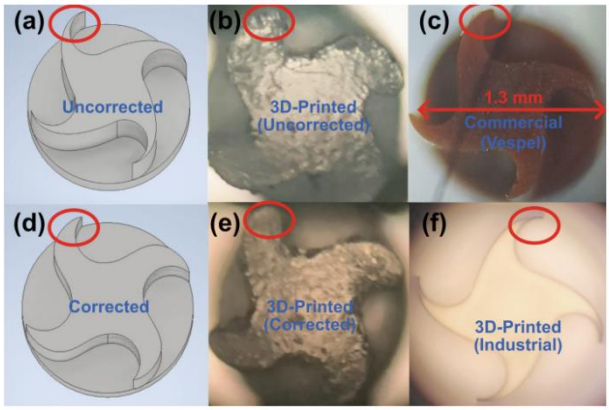

Fig. 58: 1.3 mm MAS drive caps. Images of the (a and d) CAD and (b and e) 3D-printed pieces (a and b) before and (d and e) after the design compensation. Images of the (c) machined and (f) industrial 3D-printed (BMF) drive caps.

At last, we emphasize that such iterative compensation is possible only because the 3D printing protocol yields very consistent and reproducible results. We have fabricated many batches of the drive caps over several months, and they yield very similar results.

7.1.3 MAS experiments using 3D printed caps:

The 3D-printed caps were fitted into standard ZrO_2 rotors for MAS experiments in Bruker MAS probes or a benchtop spinning station at ambient temperature. A Bruker MAS II unit was used to regulate the drive and bearing gas pressure to achieve a stable spinning frequency. We have tested at least 10 pieces of each design for at least 15 min to evaluate the MAS performance. The pressure of each gas inlet and spinning frequency as a function of time in the automated mode were logged using TopSpin (Bruker). We have tested the 3.2 mm drive caps on both ZrO_2 and sapphire rotors. All zirconia rotors fitted with 3D-printed caps spun > 20 kHz without major issues. However, the sapphire rotor crashed when spun above 18 kHz (rated for 15 kHz at RT). For the 1.3 mm drive caps printed with an industrial 3D printer (Boston Micro Fabrication (BMF)), we have tested only 2 out of the 3 ordered pieces.

7.1.4 NMR samples and experiments:

The ^{13}C-^{15}N L-Isoleucine sample was purchased from CortecNet and used without further purification. For the Metal-Organic Framework (MOF-801) sample [23], the MOF was synthesized through an established procedure and washed with D_2O using ultrasounds [23]. The D_2O washing step was performed to promote an exchange of the hydroxyl proton (Zr-OH) with deuterium, which helps unambiguously assign the Zr-O ^1H NMR peak observed in an H_2O-washed MOF sample. The D_2O-washed MOF sample was then activated in a vacuum drying oven for 12 h at 100 °C to remove excess solvent. To minimize the exposure of the dried MOF sample to the moist in the atmosphere, the sample was packed into a 3.2 mm rotor closed with a 3D-printed drive cap sealed with silicone-filled (Bluestar CAF 1) groove inside an argon-filled glove box. The NMR spectra were acquired using an 800 MHz spectrometer equipped with an Avance Neo console (Bruker). We have used either a 1.3 mm, 2.5 mm, or 3.2 mm (E-free) triple-channel MAS probe to perform MAS NMR experiments. The ^1H and ^{13}C chemical shifts were referenced to the adamantane signal at 38.5 ppm on the tetramethylsilane (TMS) scale. The RFDR experiment (Fig. 59a) was performed using the 1.3 mm probe at 45 kHz MAS frequency with a ~ 2 ms RFDR mixing time. The DARR experiment (Fig. 59b) was performed using the 2.5 mm probe at υ_r= 20 kHz with a 100 ms DARR mixing time. The HETCOR spectra (Fig. 59c&d) were acquired using a 3.2 mm probe at υ_r= 10 kHz. The experimental time for each 2D experiment is ~ 2 hr. The magic angle and field B_0 homogeneity was optimized with KBr and adamantane, respectively. The low-temperature MAS experiment (Fig. 62) was performed using a 3.2 mm HXY MAS DNP probe (Bruker). The sapphire rotor was packed with MOF-801, the surface of which was wetted with solutions of DNP juice (d8-glycerol: D_2O: H_2O in 6:3:1 by volume) doped with 5 mM TinyPol. We filled the groove on the 3D-printed drive cap with red silicone sealant so that the cap does not become loose as it shrinks at low temperatures [11]. Prior to

the MAS experiment, the rotor was immersed in liquid nitrogen at ~ 77 K to ensure that the 3D-printed cap remained intact and well-fitted to the rotor. We initially planned to perform DNP experiments with the 3.2 mm system, but the gyrotron was not operational during the experiment. Nevertheless, we performed conventional NMR experiments at low temperatures without microwaves, which allows the sample to reach a colder temperature (~105 K) due to the absence of microwave heating. The stator temperature was maintained at ~ 109 K (measured at stator after the mixing of the variable temperature (VT), bearing, and drive gas) by regulating the temperature of the three spinning gases at the probe base to be ~ 95 K. Hence, we estimated the actual sample temperature to be ~ 100 K.

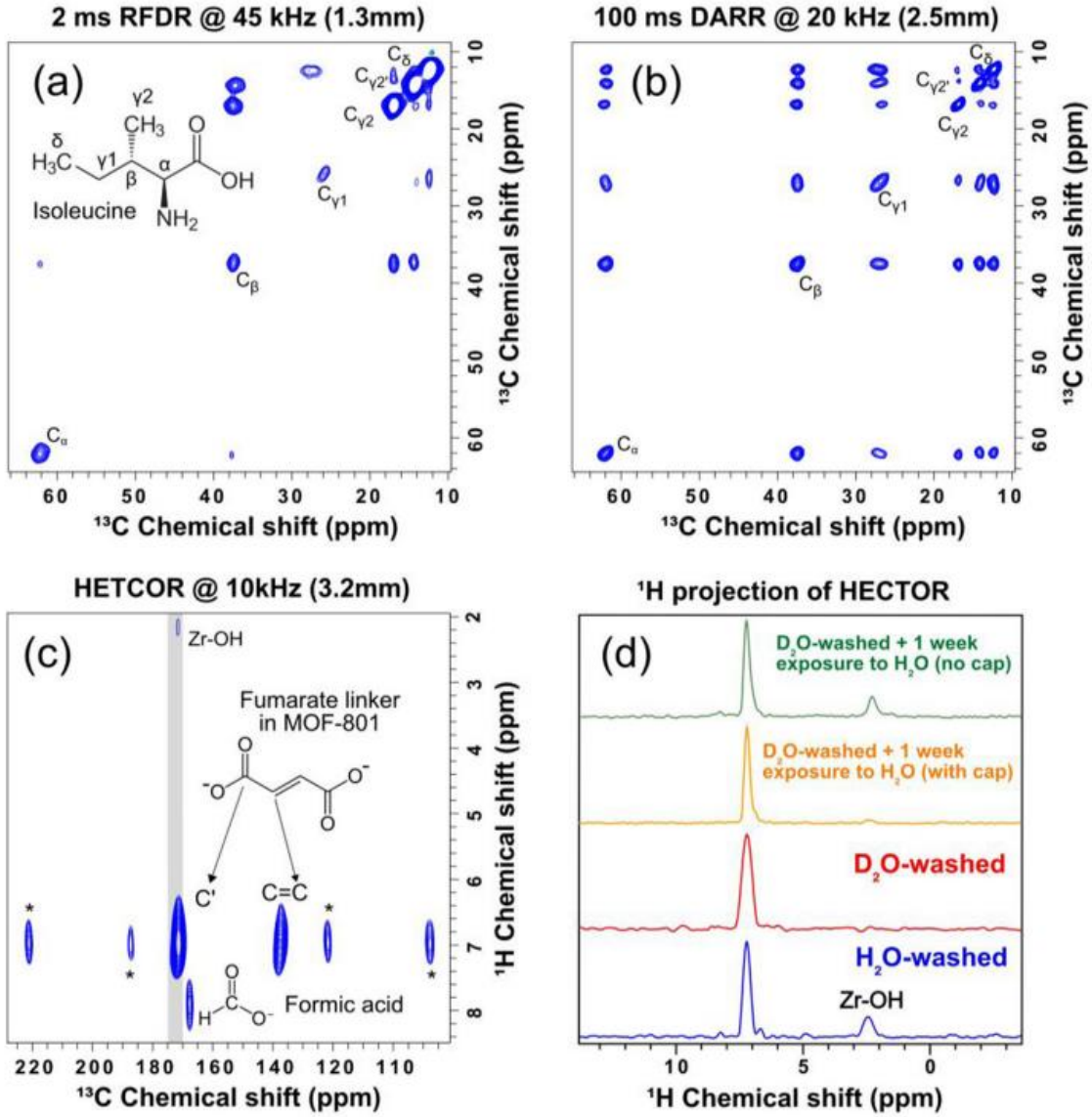

Fig. 59: 2D NMR spectra acquired with (a) 1.3 mm, (b) 2.5 mm, or (c) 3.2 mm 3D-printed caps. (a) ^{13}C–^{13}C RFDR spectrum of L-Isoleucine in a 1.3 mm rotor at ν_r = 45 kHz. (b) ^{13}C–^{13}C DARR spectrum of L-Isoleucine in a 2.5 mm rotor with ν_r = 20 kHz. (c) ^{1}H–^{13}C HETCOR spectrum of MOF-801 in a 3.2 mm rotor with ν_r = 10 kHz. * Denotes the spinning sidebands. Note that there are two isoleucine isomers that give rise to two $C_{\gamma 2}$ peaks, where the second peak is labelled as $C_{\gamma 2'}$ [39]. (d) 1D projection showing the ^{1}H dimension (integrate along the grey area in (c)) for MOF-801 washed in H_2O (blue), D_2O (red), D_2O-washed MOF exposed to saturated water vapour for one week with (yellow) or without (green) the 3D-printed cap sealed with silicone.

7.2. Results:

We found that the in-house 3D-printed drive caps for sizes ≥ 3.2 mm have almost equivalent MAS performances as the commercial caps, while the cost of 3D printing is almost negligible. Nevertheless, the smaller 3D-printed drive caps (1.3 mm and 2.5 mm) yield less satisfactory spinning performances than the machined caps. Hence, we improvised the original CAD to compensate for the printing inaccuracies (vide supra), which moderately improved the maximum ν_r to > 70 % of those specified for the commercial caps, i.e., the 2.5- and 1.3-mm 3D-printed caps can spin up to 26 and 46 kHz, respectively. Despite the lower max ν_r, the 3D-printed caps still achieve excellent spinning stability (≤ 2 Hz), which is practical for MAS NMR experiments. To further assess the transfer efficiency of the momentum from the gas to the printed drive, we have recorded the spinning profiles (Fig. 61) of the smaller caps as a function of the drive gas pressure. We noted that the 3D-printed 1.3 mm caps are less efficient and require more drive gas to reach the same spinning frequency as the commercial caps [24,25]. We hypothesized that the 1.3 mm caps could spin faster if they could be more accurately made. To test our hypothesis, we have 3D-printed the 1.3 mm caps using a state-of-the-art industrial 3D printer (BMF) with HTL resin, which has a ~ 12x higher XY resolution (2 μm) than our desktop Form 3+ printer. Not only the BMF cap exhibits sharper fins (circled in Fig. 58f) than those made by Form 3+ (Fig. 58e), but also those machined Vespel caps (Fig. 58c). Indeed, those industrial-printed caps were able to achieve ν_r = 60 kHz ± 3 Hz (Fig. 60b). Note that we have only tested two out of three available pieces. Both pieces achieve similar spinning frequencies with the same bearing and drive gas, but the second piece broke when spun above 50 kHz. This issue could be mitigated if harder materials (alumina ceramics or HT 200 from BMF) are used for printing the caps, but they are not in-house fabricated and are beyond the scope of this work. Although these industrial 3D-printed caps cost > 20 USD / piece (for a large-quantity order), they are still an order of magnitude cheaper than the machined Vespel caps.

On the printing consistency, which we defined as the ratio of the number of pieces that spin to the total number of printed parts, we have achieved very consistent results, i.e., all printed drive caps can be reliably reproduced with > 90 % consistency. Note that it is necessary to spin-test the printed drive caps ≤ 2.5 mm, as the defective pieces cannot be easily identified with visible features. For ≥ 3.2 mm drive caps, the consistencies are remarkably near 100 %. For the most used 3.2 mm system, we have repeatedly fabricated >100 pieces over a few months using the same optimized protocol, and they have all worked. We have also tested both freshly printed and several-month-old pieces, and they yield equal performances. It is noteworthy to be aware that we did not reuse any old caps because the cost is almost negligible.

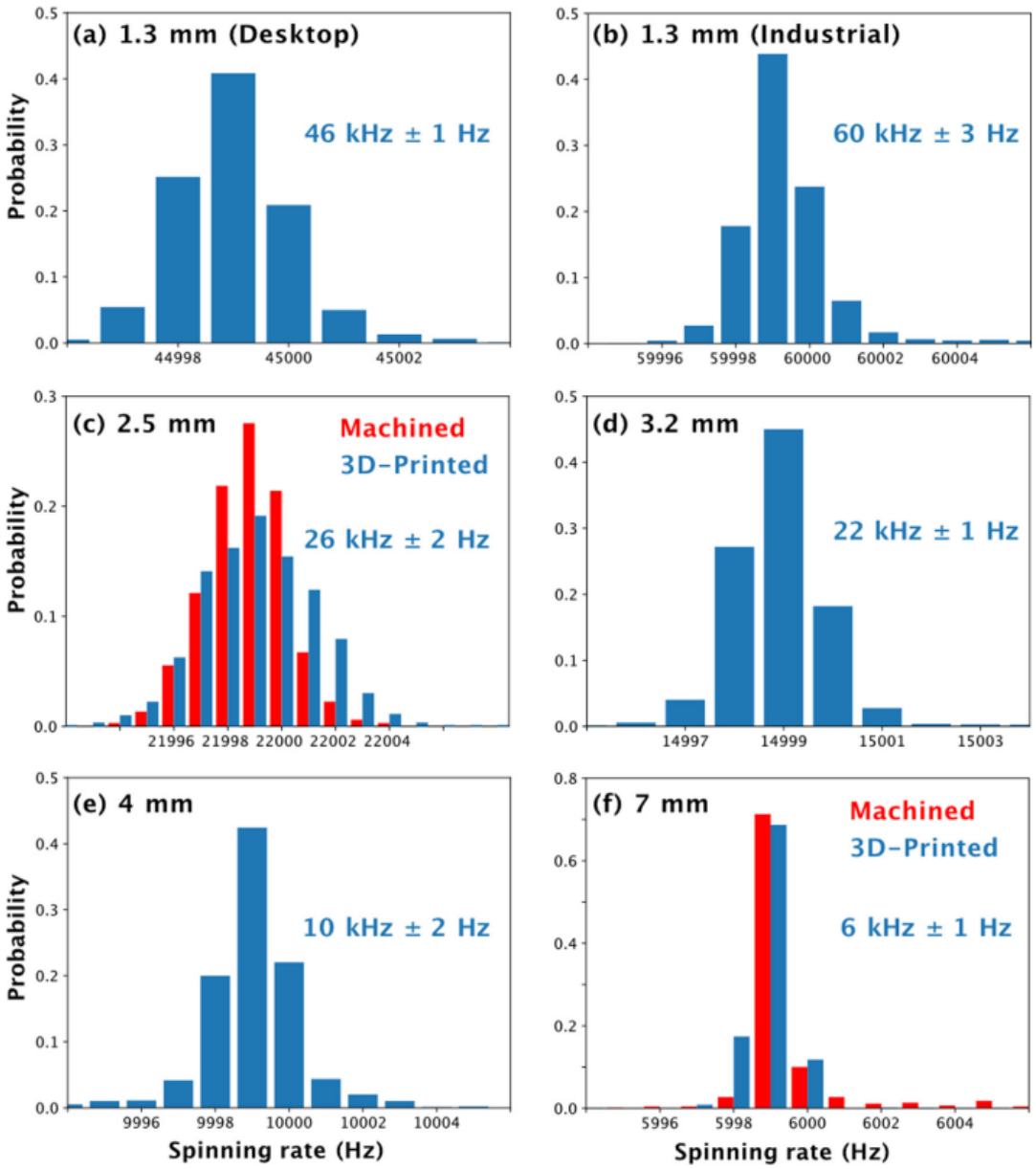

Fig. 60: Histograms of MAS frequencies for (a and b) 1.3 mm, (c) 2.5 mm, (d) 3.2 mm, (e) 4 mm, and (f) 7 mm drive caps that are either 3D-printed (blue) or machined (red, Bruker). All 3D-printed caps were made in-house except (b), which was outsourced to BMF. All caps were tested in a regulated mode using MAS II for at least 15 min. Only the standard deviation in MAS frequency for the 3D-printed caps is shown.

To assess if the 3D-printed drive caps are practical for long MAS NMR experiments, we have performed various 2D NMR correlation experiments on the 1.3 mm, 2.5 mm, and 3.2 mm drive caps on standard compounds. Among these experiments, the RFDR dipolar recoupling experiment performed on the 1.3 mm rotor requires the rf pulses to be rotor-synchronized to yield an efficient correlation between the ^{13}C peaks [26]. The fact that the 2D spectra show excellent linewidths and all the expected cross peaks, we conclude that the home-built 3D-printed drive caps are practical for actual MAS NMR experiments.

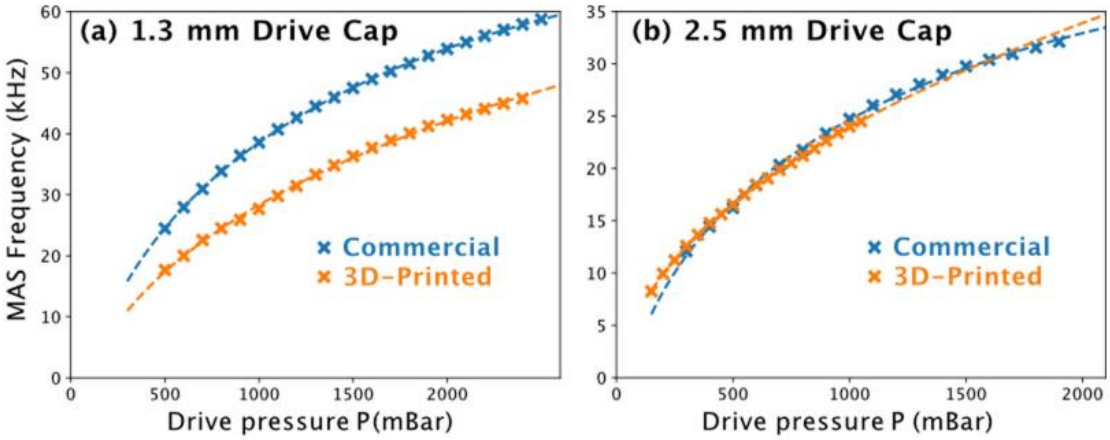

Fig. 61: MAS frequencies of the (a) 1.3 mm and (b) 2.5 mm drive caps as a function of the drive gas pressure with a constant bearing gas pressure of 3 bar. The dashed lines (–) show fitted data with function $\nu_r = AP + B\sqrt{P} + C$, where A, B, and C are numerical constants.

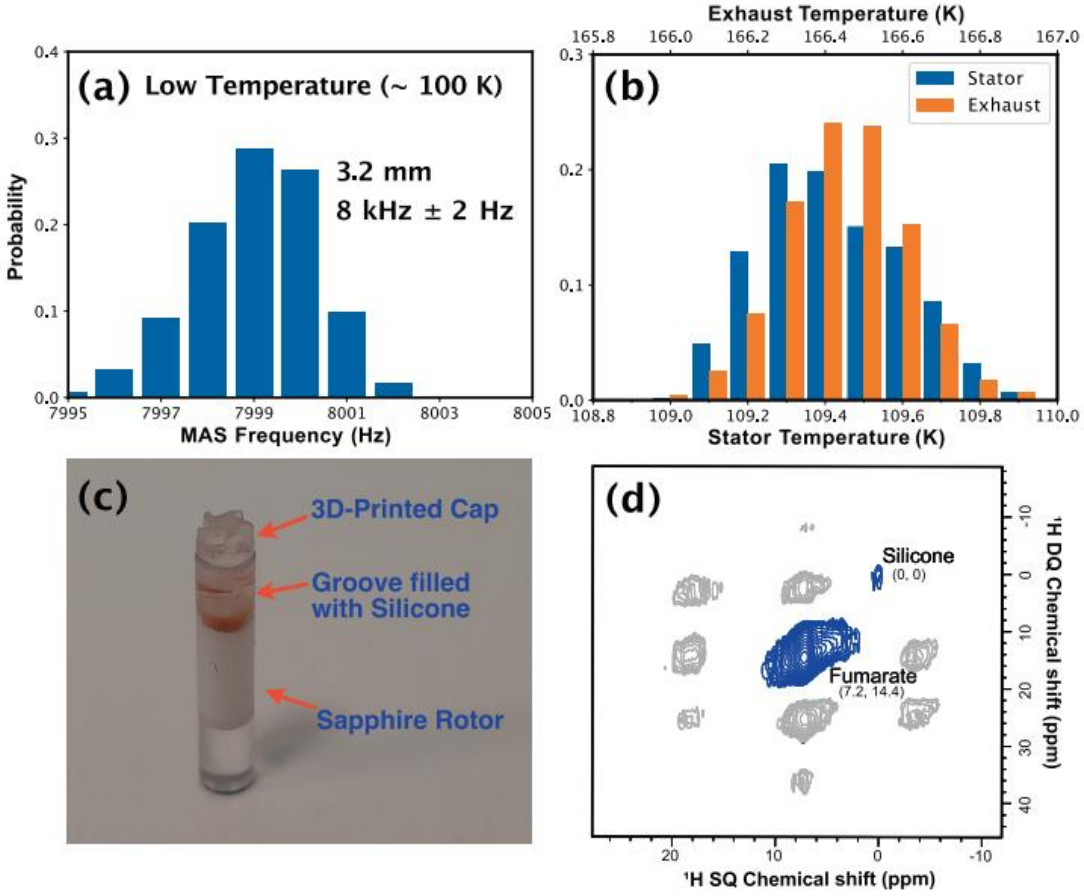

Fig. 62: (a) Histogram of MAS frequency of a 3.2 mm 3D-printed drive cap at ~ 100 K. (b) The stator and exhaust temperature were measured to be ~ 109.4 K and ~ 166.5 K, respectively. The exhaust temperature was measured at the probe base. (c) Photo of a 3D-printed drive cap with a silicone-filled groove to prevent the cap from becoming loose at low temperatures. (d) A 2D ^{1}H–^{1}H DQ-SQ (single quantum) spectrum was acquired with a C7 sequence at ~ 100 K and 18.8 T. As the exact chemical composition of the commercial silicone sealant is not known, we tentatively assign the anomalous peak to originate from the silicone sealant. In the 2D spectrum, we have observed peaks of both silicone and ligands of MOF 801 (fumarate) but not a correlation between the two sites.

In addition to the standard drive cap designs, we also prototyped new models that could be useful for special NMR applications. For instance, we have added a groove to the stem (Fig. 57c) so that the rotor could be sealed using epoxy or silicone sealant, which is useful for studying air- or moisture-sensitive NMR samples. As proof of principle, we have applied such a protocol on a MOF-801 sample packed in a 3.2 mm rotor. MOF-801 is built-up from $Zr_6O_4(OH)_4$ oxo-clusters and fumaric acid molecules. The labile proton in the –OH groups could, in principle, exchange with deuterium. To test the hypothesis, we recorded some 2D ^{1}H–^{13}C HETCOR spectra (Fig. 59c&d) of MOF-801 prepared under various conditions. The ^{1}H peak intensity at ~ 2.4 ppm is significantly lower than in the D_2O-washed sample relative to the H_2O-washed counterpart. This implies that labile ^{1}H in Zr-OH could be exchanged with D_2O to form Zr-OD, which attenuates the ^{1}H peak intensity. The experimental results allow us to unambiguously assign the observed ^{1}H peak to Zr-OH, which was previously stated in literature with only DFT calculations [27]. To examine if the sealed 3D-printed cap is sufficiently robust for studying moisture-sensitive samples, we put the rotors packed with D_2O-washed samples inside Eppendorf vials filled with a few drops of H_2O for ~ 1 week. For the rotor fitted with a silicone-sealed 3D-printed cap, the HETCOR spectrum (Fig. 59d) is nearly identical to the spectrum acquired before exposure to water vapor. In contrast, the rotor without a cap showed significant growth in the Zr-O ^{1}H peak. Hence, the results confirm that the 3D-printed cap with silicone seals provides a robust airtight condition suitable for studying air- or moisture-sensitive NMR samples. Moreover, emptying the rotors fitted with silicone- or epoxy sealed drive caps which could become unusable if destructively removed is more cost-efficient if the caps were 3D-printed in-house. Another main concern about the 3D-printed drive caps is their feasibility for low-temperature applications. It was reported by Banks et al. that the 3D-printed caps fabricated by an industrial 3D printer (Protolabs) crack at ~ 100 K [10]. To examine our printed drive caps printed (Formlabs), we fitted a 3D-printed cap into a sapphire rotor packed with MOF-801 wetted with DNP juice (see Experimental Section) and sealed with silicone sealant (Fig. 62c), before spinning it at ~ 100 K using a 3.2 mm 800 MHz MAS DNP probe. Fig. 62a shows the histogram of regulated MAS frequency of ν_r = 8 kHz ± 2 Hz at a sample temperature of ~ 100 K over ~ 17 h. The recorded spinning frequency at low temperatures is slightly less stable than the room-temperature operation (Fig. 60d), possibly due to a larger standard deviation in stator temperature (see Fig. 62b and Experimental Section). Following that, we recorded a 2D ^{1}H–^{1}H double-quantum filtered (DQF) spectrum (Fig. 62d) using a symmetry-based $C7_2^1$ sequence, which is a rotor synchronized dipolar recoupling sequence that requires a stable spinning frequency for efficient performance [28]. The 2D experiment acquired at ~ 100 K demonstrates that the 3D-printed drive cap is robust for low-temperature (including MAS DNP) applications. Besides that, we have also modelled 4 mm drive caps with a center hole (Fig. 63), which could be useful for in-situ monitoring of chemical reactions during MAS experiments, or those NMR experiments that require in-situ illumination of light or lasers [29–32]. For the first case, similar instrumentation and experiments were demonstrated in the literature [33–36], where a reactant gas was directed into a 7 mm rotor via an injection tube through the drive cap with an axial

hole. The 4 mm drive cap (without an injection tube) could spin till υ_r = 7 kHz ± 0.3 Hz, which is slightly slower than the normal cap (~ 10 kHz).

7.3. Conclusion:

We have demonstrated that it is possible to fabricate 1.3–7 mm drive caps using an affordable desktop 3D printer in-house. The moderate-accuracy but high-precision 3D printing method allows us to fabricate highly consistent (> 90 %) MAS drive caps with similar results as the commercial caps for the ≥ 3.2 mm system. The smaller (≤ 2.5 mm) caps can spin up to ~ 70 % as fast as the commercial caps, and yet with a high spinning stability (≤ 2 Hz). The high spinning stability of the drive caps allows practical multidimensional NMR experiments to be performed. Additionally, we have exploited the high-resolution (2 μm) industrial 3D printer (BMF) to fabricate the 1.3 mm caps, which yield near equivalent MAS performances as the commercial caps. We foresee that it could be possible to 3D print smaller (≤ 0.7 mm) [4,5,37,38] caps with similar or harder materials offered by the same company. In contrast to traditional machining, which becomes more challenging and expensive to fabricate smaller drive caps, 3D printing becomes cheaper as the size of the drive cap decreases—because more pieces could be simultaneously printed in a single print job on the platform.

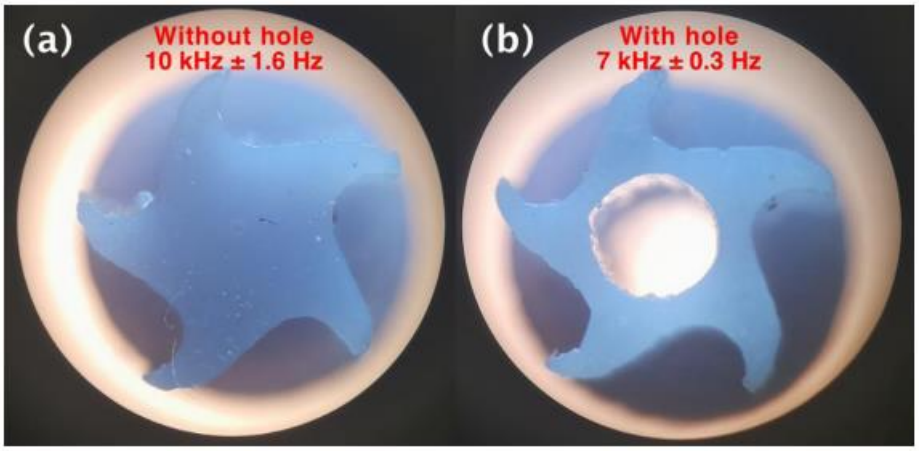

Fig. 63: Image of the 4 mm drive cap (a) without or (b) with a center hole. The drive caps were printed using a desktop 3D printer (Elegoo Saturn). Their MAS performances are specified in the image.

The relatively low cost and short fabrication time have allowed us to prototype new designs for new or custom MAS NMR applications. For instance, it costs < 1 USD and 6 h to fabricate 100 pieces of the MAS drive caps in-house. Not only does the silicone-filled groove on the 3D-printed cap provides an airtight environment suitable for studying air- or moisture-sensitive materials, but also allows low-temperature MAS experiment (including DNP) at ~ 100 K. As the 3D printing technology continues to flourish, we expect higher-resolution 3D printers will become more easily accessible by laboratories, and new tools could be fabricated in-house for novel NMR experiments.

References:

[1] B. Reif, S.E. Ashbrook, L. Emsley, M. Hong, Nat. Rev. Methods Prim. 1 (2021) 2.

[2] E.R. Andrew, A. Bradbury, R.G. Eades, Nature 182 (1958) 1659.

[3] I.J. Lowe, Phys. Rev. Lett. 2 (1959) 285.

[4] M. Schledorn, A.A. Malär, A. Torosyan, S. Penzel, D. Klose, A. Oss, M. Org, S. Wang, L. Lecoq, R. Cadalbert, A. Samoson, A. Böckmann, B.H. Meier, ChemBioChem 21 (2020) 2540.

[5] A. Böckmann, M. Ernst, B.H. Meier, J. Magn. Reson. 253 (2015) 71.

[6] F.D. Doty, EMagRes (2007).

[7] F.D. Doty, P.D. Ellis, Rev. Sci. Instrum. 52 (1981) 1868.

[8] N. Herzog, A. Weber, A. Purea, D. Osen, B. Knott, F. Engelke, D. Wilhelm, J. Fluids Eng. 144 (2022).

[9] K. Xu, O. Pecher, M. Braun, J. Schmedt auf der Günne, J. Magn. Reson. 333 (2021).

10] D. Banks, B. Michael, N. Golota, R.G. Griffin, J. Magn. Reson. 335 (2022).

[11] A.B. Barnes, M.L. Mak-Jurkauskas, Y. Matsuki, V.S. Bajaj, P.C.A. van der Wel, R. DeRocher, J. Bryant, J.R. Sirigiri, R.J. Temkin, J. Lugtenburg, J. Herzfeld, R.G. Griffin, J. Magn. Reson. 198 (2009) 261.

[12] J.I. Kelz, J.E. Kelly, R.W. Martin, J. Magn. Reson. 305 (2019) 89.

[13] H. Vanduffel, C. Parra-Cabrera, W. Gsell, R. Oliveira-Silva, L. Goossens, R. Peeters, U. Himmelreich, B. Van Hooreweder, D. Sakellariou, W. Vanduffel, R. Ameloot, Adv. Mater. Technol. 2200647 (2022) 2200647.

[14] J.I. Kelz, J.L. Uribe, R.W. Martin, J. Magn. Reson. Open 6–7 (2021).

[15] S.J. Elliott, M. Ceillier, O. Cala, Q. Stern, S.F. Cousin, S. Jannin, J. Magn. Reson. Open 10–11 (2022).

[16] Z. Long, J. Ruthford, S.J. Opella, J. Magn. Reson. 327 (2021).

[17] F. Ellermann, A. Pravdivtsev, J.-B. Hövener, Magn. Reson. 2 (2021) 49.

[18] L. Delage-Laurin, R.S. Palani, N. Golota, M. Mardini, Y. Ouyang, K.O. Tan, T.M. Swager, R.G. Griffin, J. Am. Chem. Soc. 143 (2021) 20281.

[19] K.O. Tan, L. Yang, M. Mardini, C.B. Cheong, B. Driesschaert, M. Dinca˘, R.G. Griffin, Chem. – A Eur. J. 13 (2022) 287.

[20] J. Xie, X. You, Y. Huang, Z. Ni, X. Wang, X. Li, C. Yang, D. Zhang, H. Chen, H. Sun, Z. Chen, Nat. Commun. 11 (2020) 1.

[21] P. Chen, B.J. Albert, C. Gao, N. Alaniva, L.E. Price, F.J. Scott, E.P. Saliba, E.L. Sesti, P.T. Judge, E.W. Fisher, A.B. Barnes, Sci. Adv. 4 (2018) eaau1540.

[22] C. Gao, P.T. Judge, E.L. Sesti, L.E. Price, N. Alaniva, E.P. Saliba, B.J. Albert, N.J. Soper, P.-H. Chen, A.B. Barnes, J. Magn. Reson. (2019).

[23] H. Furukawa, F. Gándara, Y.-B. Zhang, J. Jiang, W.L. Queen, M.R. Hudson, O.M. Yaghi, J. Am. Chem. Soc. 136 (2014) 4369.

[24] D. Wilhelm, A. Purea, F. Engelke, J. Magn. Reson. 257 (2015) 51.

[25] N. Herzog, D. Wilhelm, S. Koch, A. Purea, D. Osen, B. Knott, F. Engelke, J. Fluids Eng. 138 (2016) 1.

[26] A.E. Bennett, R.G. Griffin, J.H. Ok, S. Vega, J. Chem. Phys. 96 (1992) 8624.

[27] S. Devautour-Vinot, G. Maurin, C. Serre, P. Horcajada, D. Paula da Cunha, V. Guillerm, E. de Souza Costa, F. Taulelle, C. Martineau, Chem. Mater. 24 (2012) 2168.

[28] M. Hohwy, H.J. Jakobsen, M. Edén, M.H. Levitt, N.C. Nielsen, J. Chem. Phys. 108 (1998) 2686.

[29] C.G. Joo, A. Casey, C.J. Turner, R.G. Griffin, J. Am. Chem. Soc. 131 (2009) 12.

[30] X.L. Wang, Y.F. Yao, W.C. Qiao, J. Liang, W. Dong, K. Ma, J. Phys. Chem. C 125 (2021) 9908.

[31] V.S. Bajaj, M.L. Mak-Jurkauskas, M. Belenky, J. Herzfeld, R.G. Griffin, Proc. Natl. Acad. Sci. U. S. A. 106 (2009) 9244.

[32] Q.Z. Ni, T. Van Can, E. Daviso, M. Belenky, R.G. Griffin, J. Herzfeld, J. Am. Chem. Soc. 140 (2018) 4085.

[33] S. Xu, W. Zhang, X. Liu, X. Han, X. Bao, J. Am. Chem. Soc. 131 (2009) 13722.

[34] M. Hunger, M. Seiler, T. Horvath, Catal. Letters 57 (1999) 199.

[35] M. Hunger, T. Horvath, J. Weitkamp, Stud. Surf. Sci. Catal. 105 (B) (1997) 853.

[36] M. Hunger, T. Horvath, J. Chem. Soc. Chem. Commun. 1423 (1995).

[37] P. Berruyer, S. Björgvinsdóttir, A. Bertarello, G. Stevanato, Y. Rao, G. Karthikeyan, G. Casano, O. Ouari, M. Lelli, C. Reiter, F. Engelke, L. Emsley, J. Phys. Chem. Lett. 11 (2020) 8386.

[38] E. Barbet-Massin, A.J. Pell, J.S. Retel, L.B. Andreas, K. Jaudzems, W.T. Franks, A.J. Nieuwkoop, M. Hiller, V. Higman, P. Guerry, A. Bertarello, M.J. Knight, M. Felletti, T. Le Marchand, S. Kotelovica, I. Akopjana, K. Tars, M. Stoppini, V. Bellotti, M. Bolognesi, S. Ricagno, J.J. Chou, R.G. Griffin, H. Oschkinat, A. Lesage, L. Emsley, T. Herrmann, G. Pintacuda, J. Am. Chem. Soc. 136 (2014) 12489.

[39] J. Cui, J. Li, X. Peng, R. Fu, J. Magn. Reson. 284 (2017) 73

8. 3D printed Ultracentrifuge Kit:

Solid-state NMR spectroscopy is a powerful technique used for the characterization of various materials, including natural organic matter (NOM), organic molecular solids, inorganic compounds, pharmaceutical cocrystals, polymers, and proteins. It provides valuable structural and dynamic information about these materials (Mao et al., 2017; Dudenko et al., 2013; Cuny et al., 2008; Li et al., 2018; Seyger et al., 1999; Harris, 2016; Pacilio et al., 2014; Jensen et al., 2011). The lack of spectral resolution in the study of biomolecular solids by NMR led to the use of magic-angle spinning of the sample. In MAS, the sample is spun at an angle of $\theta = 54.74°$ with respect to the static magnetic field. This averages the nuclear spin interactions, which are orientation-dependent and are explicable by $3\cos^2\theta-1$. This produces NMR spectra with clear isotropic chemical shifts [9–10]. It is important that the MAS frequency be greater than the size of the anisotropic interactions to achieve an efficient line-narrowing effect. In most systems, the MAS rate up to 40 kHz is enough to average out the heteronuclear dipolar coupling and chemical shift anisotropy (CSA) interactions. But for systems with a higher order of terms in the Hamiltonian expansion, the MAS rate of 40 kHz only weakly averages the terms, resulting in a homogeneous broadening. To solve this issue, a higher rate of spinning is required. To achieve such fast MAS frequencies without significantly heating the NMR sample, the rotors are pneumatically spun with gas to reduce frictional heating. The most effective way of increasing the MAS pneumatically driven rotor is to decrease the outer wall diameter of the rotor. This started the manufacturing of smaller-diameter rotors, like 1.3mm and 0.7 mm rotors. The 0.7 mm rotor can be spun up to 110 kHz.
It gets more difficult to effectively transfer and pack samples into rotors as MAS rates get bigger and rotor diameters get smaller. This difficulty is magnified when rotors must be filled with biomolecular solids that have a diameter of less than 1 mm and must be kept moist for studies that mimic native conditions. Many of these biomolecular solids are soft, viscous slurries or gels, making them challenging to work with. Using a microspatula or other tools, it is possible to manually transfer these samples into larger rotors, but this method frequently causes sample loss or dehydration and is especially difficult for very small rotors. Furthermore, efficient and reliable rotor filling protocols are required if we are to realize another advantage of smaller rotors, namely the capacity to measure samples for which only a very small amount of material is available.
The centrifugal rotor packing device, which funnels the sample into the rotor using the centrifugal force, has solved the problem of filling these small-diameter rotors with hydrated gels or proteins. Two strategies are usually used when designing these centrifugal rotor packing devices. The first strategy is when a pre-centrifuged pallet of materials is transferred to the kit with the rotor, and the pallets are transferred to the rotor under low relative centrifugal force. while the second type directly pellets the sample into the rotor using an ultracentrifuge [19, 23–32]. Using low g-forces during the transfer process makes it possible to include fragile rotor parts like Vespel polymer caps in the assembly. These caps effectively seal the bottom of open-ended MAS rotors. However, it is important to note that these low centrifugal forces may lead to loose packing and a significant proportion of supernatant solution within the rotor, depending on the type of sample being used. On the other hand, direct ultracentrifugation directly into the rotor ensures efficient and compact packing of hydrated samples. Nevertheless, it is crucial for the device to be designed in a manner that can withstand and not deform or leak under high g-

forces. Furthermore, when employing ultracentrifugation with open-ended rotors, it is necessary to pack them without inserting the bottom cap or drive tip to prevent any damage to the cap. This requirement necessitates the incorporation of additional features to prevent any potential leaks through the rotor. The majority of the packing tools for ultra-centrifugal rotors used today are hand-made by scientists. They use long-lasting polymers like glass-filled polyether ether ketone (PEEK) or Delrin. Each device has been specifically designed to accommodate a particular size of MAS rotor and is intended for use with a specific centrifuge available to the researchers. Consequently, there is no universally applicable solution that can be employed for all situations. Moreover, all the centrifugal packing devices that are already on the market are made for rotor sizes bigger than 1 mm, and only a few labs have made custom ultracentrifuges that can fill 0.7 mm rotors with biomolecular solids [33–34].
There are two main categories of 3D printing technology: fused deposition modeling (FDM) and stereolithography (SLA). Although the FDM method has, in general, a poorer resolution, it is more affordable and easier to use relative to the resin-based SLA method. Both types of 3D printing have been used for different NMR tasks, such as making MAS sample eject systems [11], RF coils [12–15], NMR sample tubes [16], parahydrogen generators [17], NMR sample degassing apparatus [18, 19], NMR probe heads [20], and more. Besides these examples, Popp et al. recently demonstrated 3D-printed ultracentrifuge kits for packing samples in a solid-state rotor.

8.1 3D printing and post processing methods:

The centrifuge kits were designed using Autodesk Fusion 360 (Autodesk Inc., San Rafael). The kits were printed using standard clear v4 resin in our in-house Form3+ (Formlabs) printer with 25 µm XY resolution and layer thickness. The supports for the piece were put at the bottom part of the piece with a contact point size of 1mm. After the printing job is finished, the printed pieces are soaked in an isopropanol-water mixture (9:1 by volume ratio) for 25 minutes to remove the uncured resin or any other impurity that may be present in the piece. Then the supports were removed, and the piece was soaked in the isopropanol-water mixture again for 10 minutes. Then a syringe is used to suck the isopropanol-water mixture from the rotor chamber to clean it clearly. After that, pressurized gas is supplied through the exhaust side to push isopropanol-water mixed with resins out of the piece to properly clean it. Then the piece is dried properly, and only after it is dry is the piece cured under UV and heat flow for 30 minutes to enhance the mechanical properties of the piece. To account for the change in dimension after the post-processing steps, we have iteratively compensated for the changes by redesigning and reprinting the parts. To check if the dimensions are correct for the rotor space, a gauge pin of the same outer diameter as the rotor is used. Different sizes of gauge pins are inserted into the rotor chamber to correctly check the dimensions of the kit after the curing process. Fig. 64 shows the full section, and Fig. 65 shows the half-section view of the CAD file along with the 3D printed product (Fig. 66) for the case of the 0.7 mm rotor.

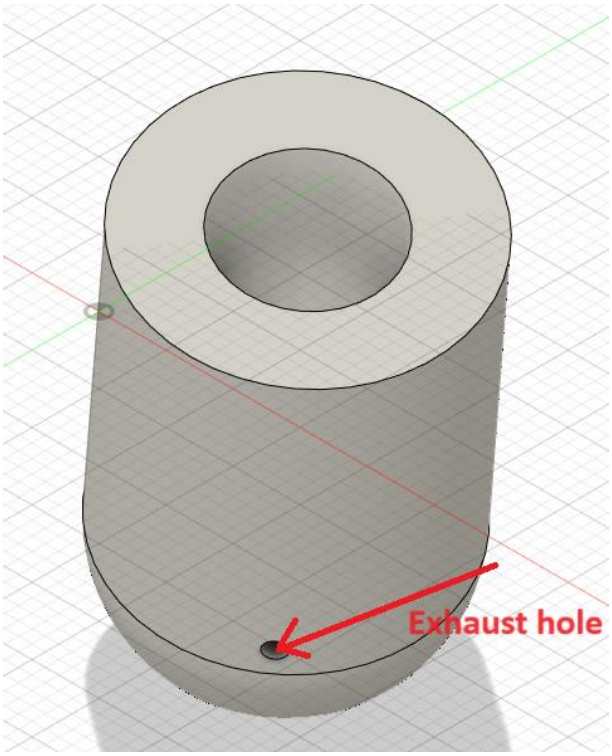

Fig. 64: A full-section view of the 0.7-mm ultracentrifuge kit with the exhaust hole shown in the figure.

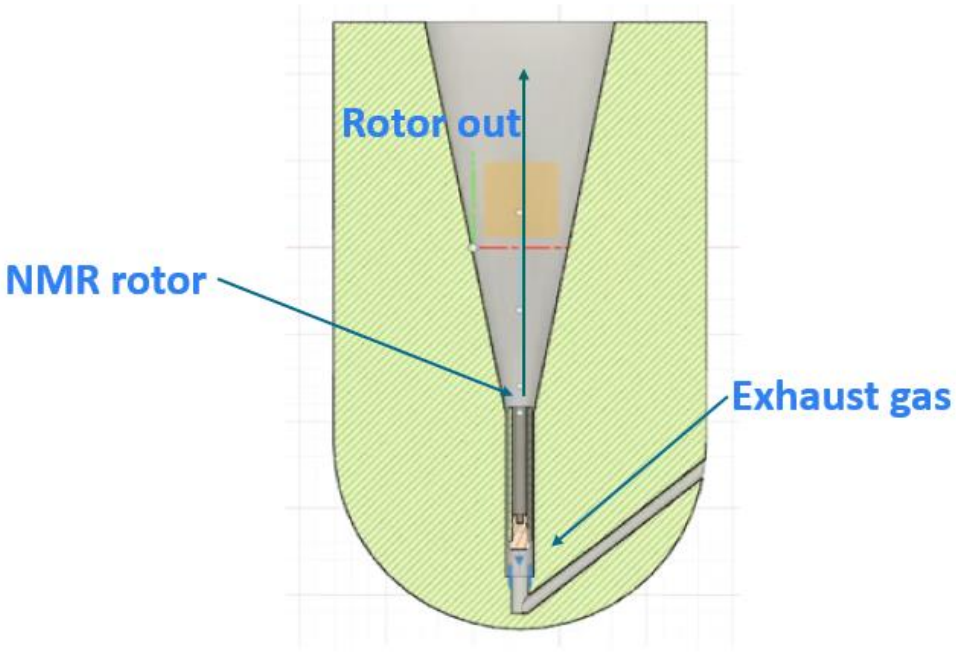

Fig. 65: A half-section view of the 0.7-mm ultracentrifuge kit with the exhaust hole and rotor chamber shown in the figure.

(a) (b)

Fig. 66: (a) the 3D-printed ultracentrifuge kit, and (b) the 3D-printed kit inside the centrifuge glass tube.

8.2 **Working principle:**

The working principle (Fig. 67) of the 3D-printed ultracentrifuge kit is that the rotor is first put into the rotor chamber of the ultracentrifuge kit. Then the aqueous suspension of the sample is pipetted into the kit, and the kit is put into the glass tube for the centrifuge.

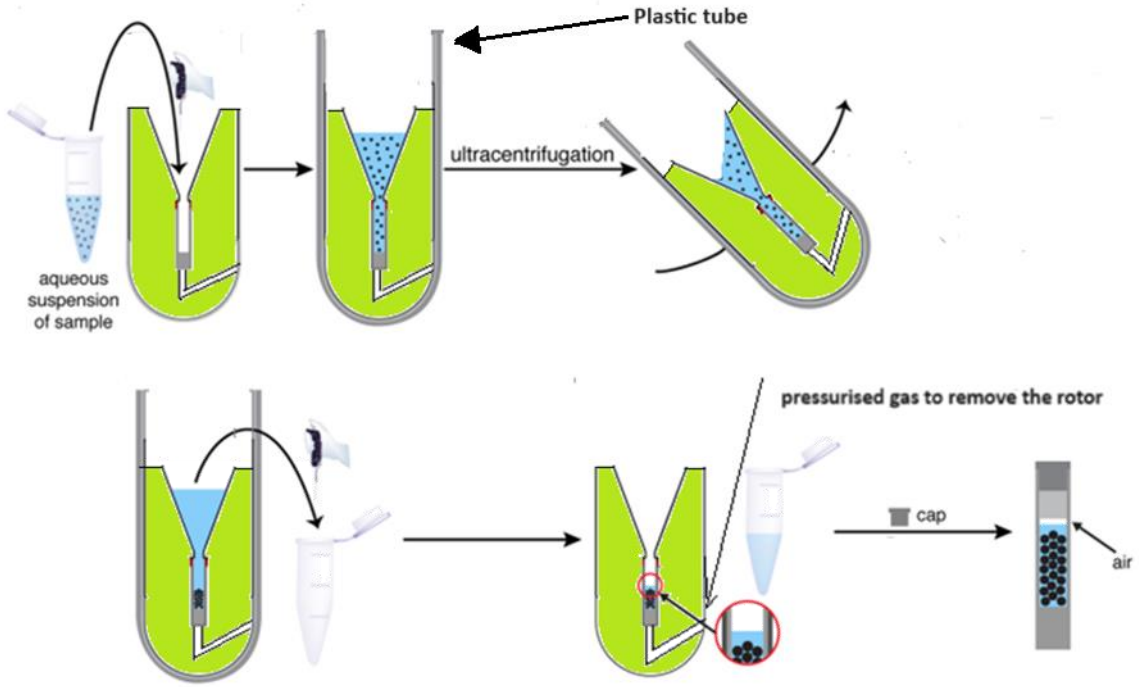

Fig. 667: The different stages of the packaging process using a 3D-printed ultracentrifuge kit.

The glass tube with the ultracentrifuge kit is put inside the centrifuge bucket for ultracentrifugation. The centrifugation is done for 1-2 hours under high-g rotation. We have tested our kit to 400000 x g, but for most of our experiments, we use 100,000–150,000 x g. The sample is sedimented during the centrifugation, and the sample is packed inside the rotor with some liquid. The rotor is then taken out of the centrifuge kit using gas. We can push the rotor out of the chamber by drawing gas from the exhaust hole, as shown in Fig. 65.

8.3 **NMR Samples and experiments:**

Our collaborator from Latvia prepared a ^{13}C-^{15}N Alpha Synuclein Fibrils sample [26] to test the ultra-centrifuge packing kit. The NMR spectra were acquired using an 800 MHz spectrometer equipped with an Avance Neo console (Bruker). We have used a 1.3-mm triple-channel MAS probe to perform MAS NMR experiments. We couldn't test the 0.7-mm packing kit in our lab due to the unavailability of a 0.7-mm solid-state NMR probe. We have sent our kit to our collaborator to test it because they have a 0.7-mm probe. To pack the sample in the 1.3-mm rotor, a Beckman Coulter Optima L-XP ultracentrifuge was used with a Type 70 Ti fixed-wing titanium bucket. The sample was packed at 100000 x g for 2 hours. For the 1.3-mm rotor, 5mg of sample was packed, and for the 0.7-mm rotor, 1mg of sample was packed by measuring the weight of the rotor before and after the packing.

8.4 **Results and conclusions:**

A 1-D NMR spectra of the sample was recorded using our 1.3-mm rotor at ENS and a 3.2 mm rotor at the Latvian Institute of Organic Synthesis.

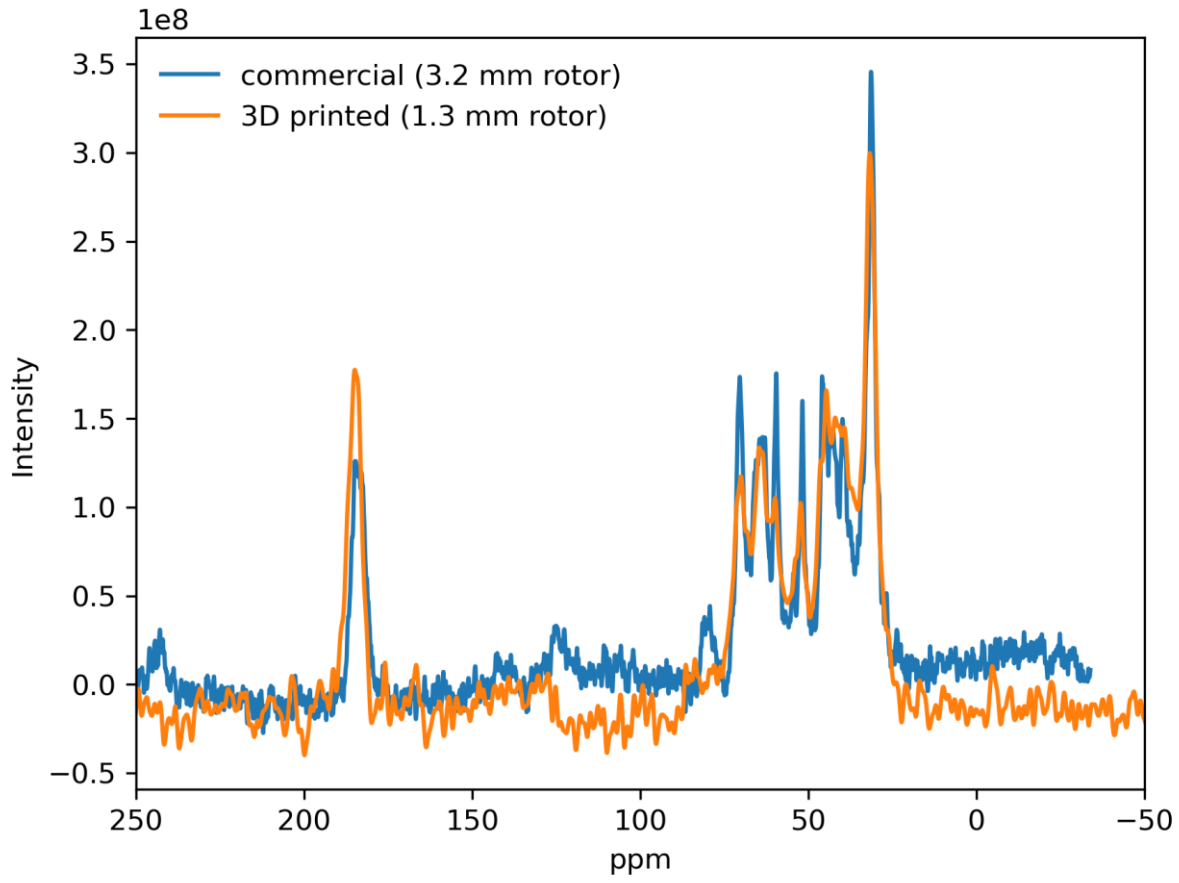

Fig. 68: 1D NMR spectra for 1.3 mm rotor (orange) and 3.2 mm rotor (blue). The 1.3-mm rotor is packed using a 3D-printed kit, and the 3.2-mm rotor is packed using commercial tools.

A 1-D NMR spectra of the sample was recorded using our 1.3-mm rotor at ENS and a 3.2-mm rotor at the Latvian Institute of Organic Synthesis. The 1.3-mm rotor was packed with the 3D-printed kit, and the 3.2-mm rotor was packed using a commercial tool. The orange curve depicts the recorded spectrum of the 1.3-mm rotor, and the blue curve depicts the recorded spectra of the 3.2-mm rotor. They are compared in Fig. 68, and even though both spectra are not identical as the conditions are different, the important thing is that the spectra show that the rotor is packed with the sample.

A 2D CP experiment was performed at v_r = 10 kHz and the recorded spectra is shown in Fig. 69.

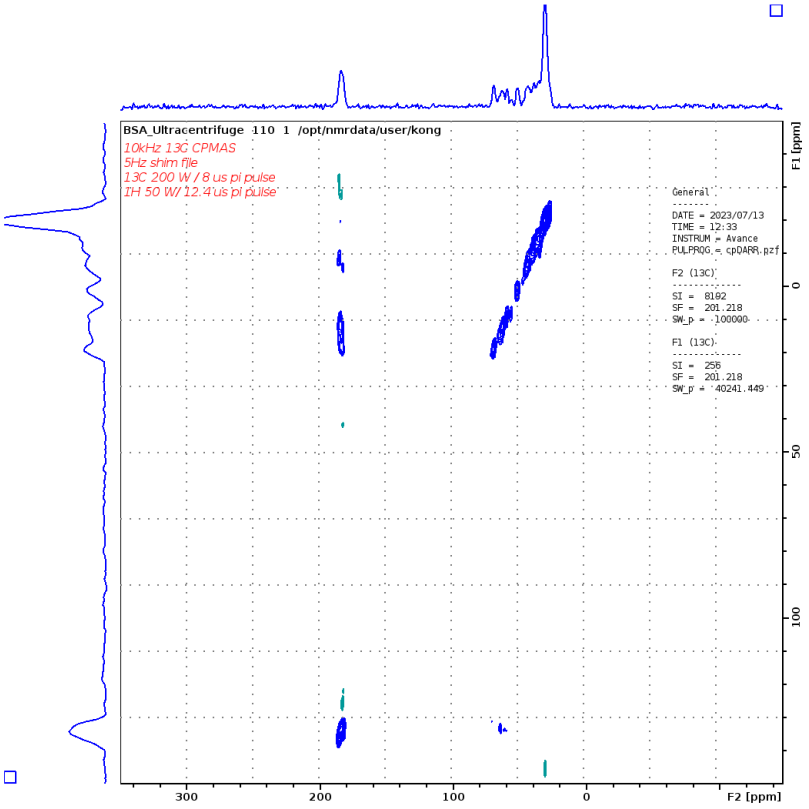

Fig. 69: A 2D CP spectra of the sample packed in a 1.3-mm rotor.

We have demonstrated that 3D printing technology can be used to fabricate centrifugal kit devices for solid-state NMR rotor packaging. A single-piece design of the kit makes it more robust than a multiple-piece design, where there is a chance of leakage and deformation under high centrifugal speed. The ejection procedure of the rotor from the kit is unique in the sense that the rotor can be used just by using gas from the exhaust or ejection hole. In the meantime, as more instruments are made that can spin rotors at speeds higher than 100 kHz MAS, having reliable and easy-to-reach tools for preparing the rotors, like the 3D-printed devices we've shown here, will speed up and improve the progress made in high-resolution ^{1}H-detected bio-molecular solid-state NMR.

References:

[1] E.R. Andrew, A. Bradbury, R.G. Eades, Removal of Dipolar Broadening of Nuclear Magnetic Resonance Spectra of Solids by Specimen Rotation, Nature 183 (1959) 1802–1803, https://doi.org/10.1038/1831802a0.

[2] I.J. Lowe, Free induction decays of rotating solids, Phys. Rev. Lett. 2 (1959) 285–287, https://doi.org/10.1103/PhysRevLett.2.285.

[3] A. Mandal, J.C. Boatz, T.B. Wheeler, P.C.A. Van Der Wel, On the use of ultracentrifugal devices for routine sample preparation in biomolecular magicangle-spinning NMR, J. Biomol. NMR 67 (2017) 165–178, https://doi.org/ 10.1007/s10858-017-0089-6.

[4] I. Bertini, F. Engelke, L. Gonnelli, B. Knott, C. Luchinat, D. Osen, E. Ravera, On the use of ultracentrifugal devices for sedimented solute NMR, J. Biomol. NMR 54 (2012) 123–127, https://doi.org/10.1007/s10858-012-9657-y.

[5] A. B¨ockmann, C. Gardiennet, R. Verel, A. Hunkeler, A. Loquet, G. Pintacuda, L. Emsley, B.H. Meier, A. Lesage, Characterization of different water pools in solidstate NMR protein samples, J. Biomol. NMR 45 (2009) 319–327, https://doi.org/ 10.1007/s10858-009-9374-3.

[6] C. Gardiennet, A.K. Schütz, A. Hunkeler, B. Kunert, L. Terradot, A. B¨ockmann, B. H. Meier, A Sedimented Sample of a 59 kDa Dodecameric Helicase Yields HighResolution Solid-State NMR Spectra, Angew. Chem. Int. Ed. 51 (2012) 7855–7858, https://doi.org/10.1002/anie.201200779.

[7] B. Kunert, C. Gardiennet, D. Lacabanne, D. Calles-Garcia, P. Falson, J.-M. Jault, B. H. Meier, F. Penin, A. B¨ockmann, Efficient and stable reconstitution of the ABC transporter BmrA for solid-state NMR studies, Front. Mol. Biosci. 1 (2014), https:// doi.org/10.3389/fmolb.2014.00005.

[8] A. Mandal, P.C.A. van der Wel, MAS ^{1}H NMR Probes Freezing Point Depression of Water and Liquid-Gel Phase Transitions in Liposomes, Biophys. J. 111 (2016) 1965–1973, https://doi.org/10.1016/j.bpj.2016.09.027.

[9] P.C.A. Van Der Wel, J.R. Lewandowski, R.G. Griffin, Solid-State NMR study of amyloid nanocrystals and fibrils formed by the peptide GNNQQNY from yeast prion protein Sup35p, J. Am. Chem. Soc. 129 (2007) 5117–5130, https://doi.org/ 10.1021/ja068633m.

[10] T. Wiegand, D. Lacabanne, A. Torosyan, J. Boudet, R. Cadalbert, F.-H.-T. Allain, B. H. Meier, A. B¨ockmann, Sedimentation Yields Long-Term Stable Protein Samples as Shown by Solid-State NMR, Front. Mol. Biosci. 7 (2020) 17, https://doi.org/ 10.3389/fmolb.2020.00017.

[11] T. Wiegand, C. Gardiennet, R. Cadalbert, D. Lacabanne, B. Kunert, L. Terradot, A. B¨ockmann, B.H. Meier, Variability and conservation of structural domains in

divide-and-conquer approaches, J. Biomol. NMR 65 (2016) 79–86, https://doi.org/10.1007/s10858-016-0039-8.

[12] C.L. Hoop, H.-K. Lin, K. Kar, Z. Hou, M.A. Poirier, R. Wetzel, P.C.A. Van Der Wel, Polyglutamine amyloid core boundaries and flanking domain dynamics in huntingtin fragment fibrils determined by solid-state nuclear magnetic resonance, Biochemistry 53 (2014) 6653–6666, https://doi.org/10.1021/bi501010q.

[13] C.L. Hoop, V.N. Sivanandam, R. Kodali, M.N. Srnec, P.C.A. Van Der Wel, Structural Characterization of the Caveolin Scaffolding domain in association with cholesterol-rich membranes, Biochemistry 51 (2012) 90–99, https://doi.org/10.1021/bi201356v.

[14] D. Cala-De Paepe, J. Stanek, K. Jaudzems, K. Tars, L.B. Andreas, G. Pintacuda, Is protein deuteration beneficial for proton detected solid-state NMR at and above 100 kHz magic-angle spinning? Solid State Nucl, Magn. Reson. 87 (2017) 126–136, https://doi.org/10.1016/j.ssnmr.2017.07.004.

[15] L. Lecoq, M. Schledorn, S. Wang, S. Smith-Penzel, A.A. Mal¨ ar, M. Callon, M. Nassal, B.H. Meier, A. B¨ockmann, 100 kHz MAS proton-detected NMR spectroscopy of Hepatitis B Virus capsids, Front. Mol. Biosci. 6 (2019) 58, https://doi.org/ 10.3389/fmolb.2019.00058.

[16] A.B. Barnes, M.L. Mak-Jurkauskas, Y. Matsuki, V.S. Bajaj, P.C.A. van der Wel, R. DeRocher, J. Bryant, J.R. Sirigiri, R.J. Temkin, J. Lugtenburg, J. Herzfeld, R.G. Griffin, J. Magn. Reson. 198 (2009) 261.

[17] J.I. Kelz, J.E. Kelly, R.W. Martin, J. Magn. Reson. 305 (2019) 89.

[18] H. Vanduffel, C. Parra-Cabrera, W. Gsell, R. Oliveira-Silva, L. Goossens, R. Peeters, U. Himmelreich, B. Van Hooreweder, D. Sakellariou, W. Vanduffel, R. Ameloot, Adv. Mater. Technol. 2200647 (2022) 2200647.

[19] J.I. Kelz, J.L. Uribe, R.W. Martin, J. Magn. Reson. Open 6–7 (2021).

[20] S.J. Elliott, M. Ceillier, O. Cala, Q. Stern, S.F. Cousin, S. Jannin, J. Magn. Reson. Open 10–11 (2022).

[21] Z. Long, J. Ruthford, S.J. Opella, J. Magn. Reson. 327 (2021).

[22] F. Ellermann, A. Pravdivtsev, J.-B. Hövener, Magn. Reson. 2 (2021) 49.

[23] L. Delage-Laurin, R.S. Palani, N. Golota, M. Mardini, Y. Ouyang, K.O. Tan, T.M. Swager, R.G. Griffin, J. Am. Chem. Soc. 143 (2021) 20281.

[24] K.O. Tan, L. Yang, M. Mardini, C.B. Cheong, B. Driesschaert, M. Dinca˘, R.G. Griffin, Chem. – A Eur. J. 13 (2022) 287.

[25] J. Xie, X. You, Y. Huang, Z. Ni, X. Wang, X. Li, C. Yang, D. Zhang, H. Chen, H. Sun, Z. Chen, Nat. Commun. 11 (2020) 1.

[26] Toleikis, Zigmantas, Raitis Bobrovs, Agne Janoniene, Alons Lends, Mantas Ziaunys, Ieva Baronaite, Vytautas Petrauskas, Kristine Kitoka, Vytautas Smirnovas, and Kristaps Jaudzems. 2022. "Interactions between S100A9 and Alpha-Synuclein:

Insight from NMR Spectroscopy" *International Journal of Molecular Sciences* 23, no. 12: 6781. https://doi.org/10.3390/ijms23126781

Acknowledgement

I would like to start by thanking my PhD supervisor and co-supervisor at ENS, Prof. Kong Ooi Tan, and Dr. Daniel Abergel for giving me a great opportunity to be a part of the Laboratoire des Biomolécules (LBM), ENS Paris. They spent so much time teaching me. Our discussions always helped me move forward in my research. They supported me, and every time I asked them for any kind of help, they graciously helped me. This research would not have been possible without their guidance.

I would like to thank Dr. Andrea Capozzi for his collaboration with us on the LOD EPR project. His help on the LOD EPR detection coil has made possible all the beautiful data that we have recorded. In his busy life, he has always found time to discuss with us different results and ideas.

This research is not just the result of my work. I wish to acknowledge the support of all my group members at ENS Paris. However, I have to thank some of my colleagues specifically because of their direct involvement in parts of my thesis.

I would like to thank Dr. Vineeth Francis Thalakottoor Jose Chacko for helping me adjust in France. He has helped me with everything from administrative issues to scientific issues. He has helped me with equipment, fixing different codes, and, most importantly, having discussions with me to solve many problems. And most importantly, he has accompanied me for good Indian cuisine in Paris.

I would like to thank Dr. Zhenfeng Pang for teaching and guiding me throughout the year. From him, I have learned many things about solid-state NMR and magnetic resonance in general. He was always there for any help at any time. The discussion we had made it possible for me to move forward in my research.

I would like to thank Dr. Nicolas Birlirakis for training me in cryogenic instruments. And Dr. Mathieu Baudin for training me on the Bruker and the cryogenic polarizer. His constant support with the polarizer made it possible to finish the thesis. I would like to thank Dr. Thiery Drujon for his constant support on the 3D-printed ultracentrifuge kit project.

I would like to thank my parents (Mr. Nirmal Banerjee and Mrs. Gopa Banerjee) for all their support, without which it would have been impossible to make this journey. I would like to thank my friends and other family members for all their support throughout this journey.

Finally, I would like to thank all the administrative staff at ENS and Sorbonne University for their constant support.